A blood exchange method to study circulation kinetics of tumor cells in the blood

by

Alex Brandon Miller

B.S. Engineering Sciences (Bioengineering)
Harvard University (2015)

Submitted to the Harvard-MIT Program in Health Sciences and Technology
in Partial Fulfillment of the Requirements for the Degree of

Doctor of Philosophy in Medical Engineering and Medical Physics

at the

MASSACHUSETTS INSTITUTE OF TECHNOLOGY

June 2023

© 2023 Alex B. Miller. All rights reserved

The author hereby grants to MIT a nonexclusive, worldwide, irrevocable, royalty-free license to exercise any and all rights under copyright, including to reproduce, preserve, distribute and publicly display copies of the thesis, or release the thesis under an open-access license.

Authored by: Alex B. Miller
Department of Health Sciences & Technology
May 1, 2023

Certified by: Scott R. Manalis
Professor of Biological Engineering and Mechanical Engineering
Thesis Supervisor

Accepted by: Collin M. Stultz, MD, PhD
Director, Harvard-MIT Program in Health Sciences and Technology
Nina T. and Robert H. Rubin Professor in Medical Engineering and Science
Professor of Electrical Engineering and Computer Science

A blood exchange method to study circulation kinetics of tumor cells in the blood

by

Alex Brandon Miller

Submitted to the Harvard-MIT Program in Health Sciences and Technology on May 1, 2023 in Partial Fulfillment of the Requirements for the Degree of Doctor of Philosophy in Medical Engineering and Medical Physics

Abstract

Blood is an essential compartment for tumor cell trafficking. In solid epithelial-derived tumors, blood serves as the major vehicle for metastasis, whose principal cell is the circulating tumor cell (CTC). These cells originate from the primary tumor and are shed at low concentrations into the blood, where they travel to distant sites to initiate metastatic lesions. In liquid, blood-borne cancers, the blood is a major reservoir of disease, and allows cells to move between the bone marrow, where disease typically initiates, to other sites throughout the body.

While the general steps of these processes is known, there is a lack of evidence in the field regarding the physical properties defining tumor cell trafficking through the blood. Several studies have estimated vastly conflicting half-life time of CTCs, ranging from seconds to hours. However, these studies are limited in that they typically involve monitoring the decay in concentration of injected *in vitro* cultured cells, rather than that of native, unprocessed tumor cells. Measuring the blood concentration of these injected in vitro cultured cells over time is insufficient to extrapolate the two defining variables which underlie the concentration of CTCs: half-life time and generation rate. Studying these parameters is crucial to understanding the nature of the metastasis of cancer throughout the body, which remains the leading cause of cancer deaths.

Our lab has developed a technology capable of detecting genetically fluorescent CTCs longitudinally directly from the bloodstream of mice in real-time. The system combines a surgical cannulation technique of the jugular vein and carotid artery with a lab-built optofluidic platform, which uses laser-based detection on a microfluidic chip, to enumerate and capture CTCs from un-anesthetized mice. By setting two of these in sequence, we aim to develop a method for transferring unprocessed CTC-containing blood between animals and monitoring the resulting blood concentrations to elucidate the circulatory kinetics of tumor cells in the blood.

In this thesis, we begin by developing a system to determine circulation properties of CTCs. Using a series of real-time CTC detection platforms, we create a model to describe how the exchange of blood between healthy and tumor-bearing mice allows us to extrapolate circulation properties of the cells. Next, we apply this platform to study the circulation kinetics of CTCs from several models of solid-tumor disease. Finally, we use these techniques to study the kinetics of leukemia cells. By varying the tumor and treatment status of donor and recipient animals, we assess how the tumor cells themselves and the microenvironment of the bone marrow impacts tumor cell clearance. We discover that E-selectin, a vascular adhesion molecule, prevents cell turnover between tumor compartments and enables relapse cells to escape circulation more quickly.

Altogether, this work provides a novel method to assess circulation kinetics of tumor cells and identify features that regulate the clearance of tumor cells from the blood.

Thesis supervisor: Scott R. Manalis

Title: David H Koch Professor, Biological Engineering and Mechanical Engineering

Acknowledgments

A PhD is not something you can do alone. I am incredibly grateful to the people who have made this work possible, from those who encouraged my initial interests in scientific research, to the scientists who laid the groundwork for the project, to the support network I have had along the way.

To start, I would like to thank my adviser, Dr. Scott Manalis, for creating a lab where students can thrive. He has taught me to think critically and to thoughtfully design experiments. He has given me room to grow and learn new skills, and has trusted me to take initiative throughout my research experience.

I would also like to thank my committee members, Dr. Sangeeta Bhatia, Dr. Michael Hemann, and Dr. David Weinstock, for their guidance and support throughout this project. They provided excellent feedback and pushed me to always think about the greater context for my research.

I would also like to thank several other professors for their helpful feedback and advice, including Dr. Andy Lane for his expertise on the leukemia projects and Dr. Alex Shalek for guidance on sequencing analysis.

Within the Manalis Lab, I was lucky to be welcomed into an amazing team. The CTC project was spearheaded by an incredible graduate student, Dr. Bashar Hamza, who I had the absolute pleasure of working with. His design of the CTC detection platform made my project possible, and I learned so much from his expertise. I am so glad to have had the opportunity to work on the development of the blood exchange platform with him. Shortly after I joined, we welcomed a visiting graduate student, Dr. Lara Meier, whose enthusiasm and intelligence pushed our team forward. I am also thankful for the mouse surgeon, Emily King, who enabled the blood exchange experiments to be possible, and a dedicated undergraduate researcher, Kelsey DeGouveia.

I am so glad to have had the chance to grow our CTC team and bring on new members. Our research is being continued through the work of two brilliant and hardworking graduate students, Felicia Rodriguez and Adam Langenbucher, who are pushing the projects in exciting new directions. Additionally, I have had the distinguished honor to welcome an incredible mouse surgeon, Dr. Lin Lin, who innovated our surgeries to extend survival and sampling periods. Our team also was joined by a hardworking technician, Christina Bray, and several undergraduate researchers, Emily Ryeom and Rebekah Costello.

Within the broader Manalis lab, I have met some of the kindest and smartest researchers, who have guided my research and served as incredible friends. I specifically thank Dr. Ye Zhang, Dr. Jason Yu, Dr. Max Stockslager, Richard Wu, Sarah Duquette, Nolawit Mulugeta, Dr. Teemu Miettinen, Dr. Yorgos Katsikis, Dr. Mary Mu, Dr. Peter Winter, and Dr. Scott Knudsen for all of their work on the project and in my development as a scientist.

I would also like to thank the collaborators who made this work possible. Dr. Sheng Rong Ng, Dr. William Freed-Pastor, Dr. Grissel Cervantes Jaramillo, and Dr. Megan Burger, along with their advisor Dr. Tyler Jacks, for help with many of the animal models used for these studies. I would also like to thank Dr. David Goulet from the Hemann Lab, as well as Dr. Gonwei Wu from the Weinstock Lab, for their expertise with the leukemia models.

Within the Koch Institute, I have had the opportunity to work with many supportive staff members in the Core Facilities. In the Flow Cytometry Core, I thank Glenn Paradis and Michele Griffin. From the Histology Core, I thank Kathleen Cormier, and from the Microscopy Core, I thank Jeffrey Kuhn.

This work could not have been done without the incredible staff of the Koch Animal Facility, particularly Brian Lagace, Veronica Vargas, and Hilda "Scooter" Holcombe, who taught me how to effectively and humanely perform animal research.

I would also like to thank my friends and mentors from my time working in the Bhatia lab, who taught me how to be a better scientist and prepared me for my graduate studies. Dr. Sangeeta Bhatia was instrumental in fostering my scientific mind and teaching me how to thoughtfully approach research. Specifically, I would like to thank the Malaria Team that I was a part of: Dr. Sandra March, Dr. Nil Gural, Dr. Liliana Mancio, Dr. Jiang He, Meghan Marquette, and Dr. Allison Demas. I would also like to thank others in the Bhatia Lab who made my time there so special, including Dr. Heather Fleming, Dr. Tiffany Vo, Dr. Amanda Chen, Dr. Lian-Ee Ch'ng, Dr. Quinton Smith, Keval Vyas, Trevor Nash, Kelsey Hern, Maria Ibrahim, Emilia Pulver, Henry Ko, and Dr. Leslie Chen.

While I was in undergrad, I first learned how to approach scientific research from Dr. David Mooney and Dr. Yevgeny Brudno. Their guidance encouraged me to eventually pursue a graduate degree, and I am grateful to have worked with them.

Outside of the lab, I have had an incredible network of friends and family, who have pushed me to be my best and supported me along the way. My parents, Lori and Wayne, always encouraged me to pursue my passions and have been there for me every step of the way. My brothers, Bruce and Gary, have been my role models since childhood, and the entirety of my extended family have cheered me on and been there for me. I also thank my friends from near and far for their unending support.

Finally, to my husband, Alexander Raun. Words cannot describe how important you are to me. You have been by my side for 10 years, and I truly would not be where I am without your love and support.

Table of Contents

List of Figures

List of Tables

1. Introduction to tumor cells and the blood

Cancer and the blood are inextricably linked. Early on in cancer development, blood supplies the tumor with nutrients for development. As the tumor develops, it can alter circulation to increase blood flow and vascularization, allowing for even more rapid growth. And in late-stage disease, blood serves as the major avenue for the spreading of disease throughout the body[1,2].

Cancer can be classified broadly by whether the mutated cells develop in tight clumps of cells. If they do, these diseases are classified as solid tumors. Solid tumors make up nearly 90% of adult cancer, from breast cancer to melanoma to pancreatic cancer[3]. The other tumor type, liquid tumors, describe cancers of the blood cells. Liquid tumors, including leukemias and lymphomas, involve the hematological organs, such as bone marrow, spleen, blood, and lymph nodes, though some can also form nodules in other tissues[4].

For both solid and liquid tumors, the blood plays an important role in transporting cells throughout the body. And the spreading of cancer through the blood is the leading cause of cancer deaths. By studying the ways that tumor cells interact with and are trafficked through the vasculature, we can better understand how cancer spreads and identify potential targets for new therapeutic agents.

1.1 Solid tumors and the blood

Metastasis, or the spreading of cancer from its initial site to locations throughout the body, is the leading cause of cancer deaths, accounting for up to 90% of mortality[5,6]. By far the most common path of spreading to distant organs is the involvement of tumor cells in the blood. While the general steps of metastasis are relatively understood, little is known about the physical properties that define the spread of tumors through the blood and the specific factors that contribute to trafficking of tumor cells in circulation.

1.1.1 Circulating tumor cells (CTCs)

For cancers originating in the epithelium, in order to spread from their initial location in the body, the tumor cells must perform a series of tasks, most of which develop due to genetic mutations and changes in transcriptional regulation (Figure 1.1)[7]. First, the tumor must invade the surrounding tissue by breaking through the basement membrane, which is the thin layer that separates the epithelial layer from underlying stroma. Next, the cells undergo a transition known as epithelial-to-mesenchymal transition (EMT) whereby the cells lose much of their epithelial phenotype and behave more like mesenchymal cells[8–10]. They thus lose their polarity and become migratory, an important feature for developing eventual metastases. They also take on a stem cell-like gene expression, as they increase their ability to self-renew[11,12]. After EMT and migration toward blood vessels, the cells must break through the endothelial layer and enter the bloodstream, a process known as intravasation.

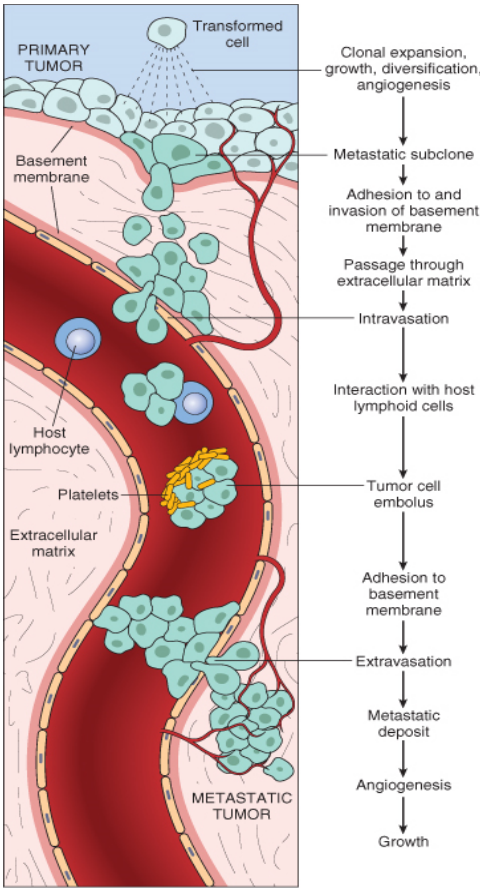

Figure 1.1 Overview of the metastatic pathway[7]. Cells that undergo certain genetic mutations (transformed cells) expand in a primary tumor. After the acquisition of further genetic mutations, subclones can migrate through the basement membrane and into the bloodstream, a process known as intravasation. The circulating cells can interact with immune cells and platelets before exiting the blood at a distant site, a process call extravasation, where they can begin to develop a metastatic tumor.

Once a cancerous cell enters the bloodstream, it is referred to as a circulating tumor cell (CTC)[13]. A subset of CTCs will go on to initiate metastases in a distant location. Tumor cells traveling in the bloodstream must avoid immune attack and find their way to a distant site where they can begin to grow. Once a cell has found a distant site, it must extravasate, or exit the bloodstream, by first binding to the vascular wall and then traversing the endothelial layer, before beginning to grow as a metastatic tumor[14–16]. Two hypotheses have been suggested as to how CTCs find the best place to grow. One proposes that tumor cells get trapped in the first capillary bed that they come across[14]. This would suggest that cancer cells which enter the portal venous system would metastasize to the liver, systemic tumors would spread to the lungs, and lung tumors could metastasize to any systemic organ. However, many clinical observations contradict this, since breast and prostate cancers, whose next capillary bed in the circulatory system is the lung, have a propensity to metastasize to bone, while patients with melanoma, which would also be expected to have lung metastases, are commonly found to have brain metastases[16–22]. The alternative hypothesis is termed “seed-and-soil”, which posits that circulating cells find a distant site that has the most optimal microenvironment and molecular cues for their growth[23–25]. Regardless of the method of locating a desirable site, CTCs are a crucial player in the metastatic pathway, and are responsible for spreading a tumor from its primary site to distant locations throughout the body.

1.1.2 Solid tumor models

In order to study cancer in a controlled setting, the use of preclinical models in needed. While the most simplistic models involve *in vitro* culture of human or animal cell lines, these systems are unable to capture the various stages of the metastatic cascade, and as such, are unable to be used to effectively study the kinetics of tumor cells in the blood. To that end, more complex systems are needed, primarily through the use of mouse models.

Mouse models are an important aspect of the study of cancer for many reasons. Mice and humans share many of the same genetic and transcriptomic features, allowing for the extrapolation of function and importance of key proteins[26,27]. Mice also share a majority of the organ systems as humans, which allows us to examine the complex interactions between organ systems[28–30]. And importantly for the purposes of this project, mice can be used to effectively model the various stages of cancer.

Several types of mouse model are available to study cancer, with various benefits and drawbacks. Patient derived xenograft (PDX) models use cancerous cells derived from patients in order to initiate a mouse tumor. These models typically start from a biopsy of a patient tumor, which is either directly implanted into a mouse or implanted following *ex vivo* cell culture[31]. PDX systems are often thought to behave most similarly to that of human patients, since the tumors themselves contain actual human cells, and are commonly used for patient-specific drug screening in a precision medicine model, as a way to identify potential therapeutics that a patient's specific tumor will be most likely to respond to[32–34]. However, if human cells were injected into a standard, wild type mouse, the mouse immune system would quickly recognize the human tumor cells as foreign, and begin attacking them, preventing the development of a tumor. This would render the model useless, as there would be no actual tumor present to study. As such, immunodeficient mice are used for PDX implantations. These mice contain specific genetic mutations that prevent the development of a normal immune system, thereby preventing the killing of cross-species cells. The most commonly used mouse is the NSG (NOD scid gamma) which prevents the development of mature T cells, B cells, and natural killer (NK) cells[35]. While PDX models can be an effective way to test tumor-drug interactions, they do have some key drawbacks. The time to creating a PDX model can be incredibly long, taking up to a year or more for the tumor to develop in the mouse[36].

In the context of precision medicine this can be problematic, as patients diagnosed with late stage or aggressive tumors may only survive a few months without treatment. If it takes a year to discover which drug a patient's tumor most effectively responds to, then those patients with fast-growing tumors will not be able to reap the benefit that these models provide. Additionally, the lack of an immune system in the mouse prevents the study of any immune-mediated tumor impacts. And since interaction with the immune cell-rich blood is such a crucial element of CTC trafficking, using an immunodeficient mouse model could alter the phenotypic kinetics of CTCs in the bloodstream. As such, an immunocompetent mouse model with intact immune system is important to exploring the circulation kinetics of CTCs.

Another type of mouse model of cancer is the use of genetically engineered mouse models (GEMMs). These systems consist of a mouse whose DNA has been altered to predispose it to develop tumors, either from birth or upon external induction[37]. One of the more common methods of gene modification uses the lox-Cre recombination system[38]. This system involves the expression of a particular enzyme, Cre recombinase, that is able to cut and recombine DNA at specific sequence signature, called loxP sites. When Cre recombinase is turned on in a cell, it actively removes the DNA sequence been two loxP sites, allowing for cell specific genetic manipulation. Typically, a transcription factor specific to the tumor-origin cell of interest is used as a promoter to turn on Cre recombinase production, and loxP sites are inserted into the genome at specific oncogenes or tumor suppressor genes that are important for the particular tumor model of interest. For example, pancreatic ductal adenocarcinoma (PDAC) in humans is characterized in over 75% of patients by the deletion of the cell-cycle transcription factor p53, and the mutated expression of the GTPase K-Ras [39]. One of the most commonly used GEMMs of pancreatic cancer is called the KP (Kras and p53 mutant) model[40], in which loxP sites flank a crucial exon of the p53 gene, and loxP sites flank a stop codon in front of a mutated K-Ras gene, often a G12D mutation, in which the twelfth amino acid is changed from a wild-type glycine to a mutated arginine. Thus, when Cre-recombinase is turned on in a cell, two things happen. The removal of a crucial exon of p53 renders the protein unfunctional, turning off the expression of the tumor-suppressor gene. And the removal of a stop codon in front of a mutated K-Ras turns on the expression of the constitutively active mutated oncogene. Since the KP signature is common for a number of cancer types, including non-small cell lung cancer (NSCLC) and colorectal cancer, it is crucial that the tumor is initiated in the appropriate site and cell type to study the particular tumor of interest[41,42]. One way to control this is through an additional genetic alteration, that only turns on expression of Cre recombinase in the specific cell type of interest. In the PDAC model, a pancreas specific transcription factor, pancreatic and duodenal homeobox 1 (PDX-1), is often used for this purpose[43]. By breeding mice that express a PDX-1 driven expression of Cre recombinase with the added KP genetic alterations, only the pancreatic cells turn on expression of Cre, and thus only cells of the pancreas experience the genetic manipulation that drives the p53 deletion and K-Ras mutation, so only pancreatic tumors develop. Similar transcription factors can be used to initiate Cre-recombinase production in other cell types. One of the drawbacks of using GEMMs born with a Cre driver is that the timing and dosage of Cre is not controllable. All cells that express the driver protein experience the mutational changes, and this process begins as soon as the cell-type specific transcription factor is expressed, often starting at birth or *in utero*. In the pancreatic cancer model, the entire pancreas quickly becomes one huge tumor, leading to rapid death of the animal, and often not allowing sufficient time for the full metastatic cascade, to develop. To have more control over the timescale of tumor development, external Cre can be administered at a desired time, often through viral infection[44]. The delivery of Cre recombinase to the site of interest, such as lung, colon, or pancreas, is thus highly controlled, and cell type specific viruses can be used to further control the specificity of tumor origin cell of interest[45]. Additionally, by titrating the dosage, a controllable subset of the cells will be activated, allowing for smaller initial tumors to grow, which can then develop over time to undergo the full metastatic cycle, including the production of CTCs and distant metastases. GEMMs are very useful for studying specific genetic perturbations in the context of a normal immune system. However, these models tend to be relatively slow growing, taking anywhere from a few months up to a year or more, depending on the dosage of viral Cre, to recapitulate the full course of disease[46]. Additionally, it can be difficult with GEMMs to quickly iterate with novel genetic manipulations, since the development of new GEMM breeds can be time intensive, and there must be known specific mutational changes, such as the KP model, that lead directly to the development of the tumor type of interest.

A third category of mouse model of cancer is syngeneic models. These involve the transplantation of murine cancer cell lines into immunocompetent mice. By using mice that share identical genetic background to the mouse that derived the cell line, immune rejection is prevented, allowing the tumor to grow in the mouse[47,48]. These models tend to be very tractable and give the user much more flexibility over the specific features of the tumor type as well as the location of tumor growth. Solid tumors of many types can be implanted either orthotopically at the tissue site, for example a breast cancer line injected into the mammary fat pat, or ectopically at a different site, often subcutaneously on the flank of the mouse which allows for easy monitoring of tumor growth. And cells can be injected either in a suspension or as organoid clusters, allowing for further control over the specifications of the tumor[49,50]. However, many of the cell lines used for these models have been passaged repeatedly and grow extremely readily both *in vitro* and *in vivo*. As such, syngeneic models often develop rapidly, with mice succumbing to the disease over the course of several weeks. While this can be very useful for increased throughput, many of these models develop as an aggressive primary tumor nodule that does not undergo metastasis[51]. As such, the study of CTCs and their kinetics would require the verification that such a model produces sufficient metastatic development to shed CTCs into circulation.

For this project, three models of solid cancer were explored. The first was a GEMM of small cell lung cancer (SCLC), driven by the deletion of tumor-suppressing genes p53, retinoblastoma protein (Rb1), and phosphatase and tensin homolog (Pten). This model is highly metastatic and can have large numbers of CTCs in the blood, making it ideal for the study of CTC kinetics[52]. The second model was a KP GEMM of non-small cell lung cancer (NSCLC), driven by the deletion of p53 and the turning on of an oncogenic KRAS mutant (G12D)[44,53,54]. Finally, we used several models of pancreatic ductal adenocarcinoma (PDAC), including a KP GEMM as well as several KP syngeneic organoid models[50]. The NSCLC and PDAC models have lower rates of metastasis, allowing us to study the kinetics of tumor cells in the blood across a wide array of tumor types with differing burdens of disease in the blood.

1.2 Liquid tumors and the blood

Hematologic cancers, comprised predominately of leukemias and lymphomas, are also often called liquid tumors due to their occurrence in the blood, lymphatic system, and bone marrow[4]. Leukemias, for which there are over 500,000 new diagnoses every year worldwide, arise due to proliferative mutations in white blood cells of the bone marrow, enabling them to crowd out healthy bone marrow cells, leading to high numbers of circulating leukemia cells (CLCs) in the blood[55]. Lymphomas, on the other hand, arise mainly in lymph nodes and have little blood involvement.

Leukemias can be classified as acute, defined by poorly-differentiated cells and disease that progresses very quickly, or chronic, defined by more fully-differentiated cells and disease that progresses more slowly. They can also be categorized broadly by the two main lineages of blood cells, myeloid or lymphoid. These classifications define the four main sub-types of leukemia – acute lymphoblastic leukemia (ALL), acute myelogenous leukemia (AML), chronic lymphocytic leukemia (CLL), and chronic myelogenous leukemia (CML), although less common forms of leukemia also exist[57]. Leukemias can be further identified based on the specific cell type impacted,

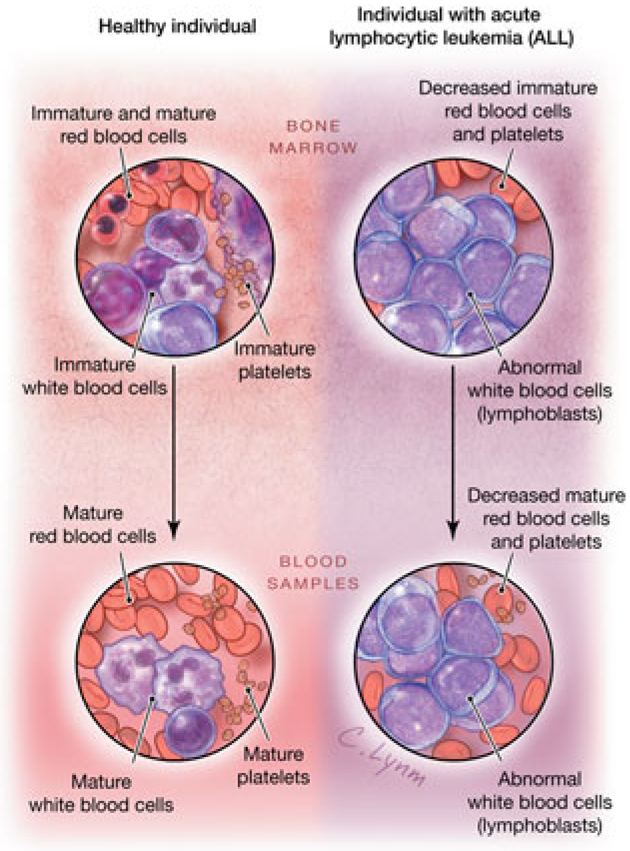

Figure 1.2 Healthy and leukemic bone marrow and blood samples. In healthy individuals (left), a diverse population of immature cells in the bone marrow gives rise to mature cells in the blood, with many red blood cells and a smaller relative fraction of white blood cells and platelets. In patients with acute leukemia (right), both the bone marrow and blood are overwhelmed with abnormal immature white blood cells, which crowds out the red blood cells and platelets[56].

such as pre-cursor B lymphocytes, mature B lymphocytes, or T lymphocytes, in the case of ALL, and by the specific genetic mutations present in the leukemic cells[4].

One property that characterizes nearly all leukemias is the transport of cells through the blood. Leukemia typically begins with a mutated cell in the marrow of one bone, but very rapidly spreads through the blood via CLCs to involve marrow throughout the body. At the time of presentation, nearly all patients present with uniform levels of disease throughout the bone marrow[4]. Leukemias continue to spread to other hematological organs (spleen, lymph nodes) and can involve non-lymphatic organs, such as the liver and the brain, all by trafficking through the blood[58,59].

1.2.2 Property changes in leukemia

Bone marrow hypercellularity has been observed in *in vitro* and *in vivo* models of all the major subtypes of leukemia[60,61]. Leukemic cells can crowd out osteoblasts and other healthy cells within the bone marrow, and overtake bone marrow niches to promote leukemogenesis, at the expense of healthy hematopoiesis and osteogenesis (Figure 1.2). They continue to rapidly divide and block the production of normal blood cells, leading to symptomatic presentation in patients of anemia (by blocking normal red blood cell production), clotting issues (by blocking normal platelet production), or susceptibility to infection (by preventing healthy white blood cell production). Leukemia can also lead to changes in remodeling of the bone marrow. Changes in extracellular matrix (ECM), as well as decreased calcium deposition, are commonly found in leukemia. This presence of bone marrow remodeling has been shown to clinically correlate with worse prognoses[62]. In addition to remodeling of the architecture of the bone marrow, the vasculature, particularly in the bone marrow, has been shown to have increased permeability in leukemias, a phenomenon often described as “vascular leakiness”[4]. Vascular leakiness has also been shown to be implicated in disease progression, as it is correlated with worse prognoses, and inhibition of increasing vascular permeability has been shown to improve efficacy of chemotherapy and outcomes[63,64].

1.2.3 Treatment of leukemias

While surgery is often the most favorable first-line therapy for solid tumors, where a primary tumor can be physically excised, such treatments are not applicable for leukemias, as there is no true mass to be removed. As such, chemotherapy is often the first treatment explored, though newer immunological treatments have recently been developed to target the disease more effectively.

In AML, the most common induction (first-line) chemotherapy is a 7+3 regimen of cytarabine and an anthracycline such as daunorubicin[65,66]. This treatment involves seven days of continuous cytarabine dosing, with single doses of daunorubicin on each of the first three days. These chemotherapy treatments are often effective at reducing the burden of disease in patients, typically through non-specific killing of rapidly dividing cells. Cytarabine is a nucleotide analog, which has a similar structure to the nucleoside deoxycytidine, which allows it to be incorporated into the DNA as cells replicate their genome. However, it is sufficiently different from the normal nucleoside as to prevent normal transcription, leading to cell death. Anthracyclines are intercalating agents, which have a flat ringed chemical structure that allows them to slide between nucleotides in the DNA of a cell, which prevents DNA replication, also resulting in cell death. In ALL, a commonly used chemo agent is cyclophosphamide. This drug is metabolized in the liver to produce phosphoramide mustard, an alkylating agent that crosslinks DNA. Because these chemotherapies are non-specific, they kill off many rapidly dividing cells, including cells of the hair follicles, the gut, and normal hematopoietic stem cells. Thus, these treatments lead to a number of intense side effects, ranging from hair loss and vomiting to anemia and susceptibility to infection, and often requires constant monitoring of the patient[67].

To overcome these unwanted side effects, targeted treatment options can also be available for patients whose tumors have certain genetic mutations. For instance, one of the common mutations in ALL, the BCR-ABL translocation also called the Philadelphia chromosome (Ph+), results in a constitutively activated tyrosine kinase. As such, tyrosine kinase inhibitors have been developed that specifically target the mutated protein. These drugs, including imatinib and desatinib, have dramatically increased survival in Ph+ patients[68]. Similarly, for AML, targeted therapies have been developed for several common mutations. Gemtuzumab is a monoclonal antibody therapy that binds CD33 and is a treatment option for patients that express that surface protein[69]. Another targeted therapy, midostaurin, is a tyrosine kinase inhibitor that specifically binds to a FLT3 mutation common for AML patients[70,71].

Immunotherapy is a newly developing field that has made progress in treating both solid tumor cancers and leukemias. This category of treatment harnesses the natural killing ability of the immune system to more effectively target the tumor. One of the most commonly used immunotherapies involves a process known as checkpoint blockade[72]. Cytotoxic T-cells, which use specific antigen recognition to destroy damaged or pathogen-infected cells, express certain surface proteins, including PD1 and CTLA4 that serve to mitigate their killing potential of normal cells. Many tumor types evolve to use this property to their advantage, by presenting specific proteins, such as PDL1 and B7, which bind to PD1 and CTLA4, respectively[73]. Activating this "immune checkpoint" inhibits the killing function of the T cells and allows the tumor to continue growing unrestricted. Recently, antibodies have been developed that interfere with this process, and prevent the tumor cells from binding to PD1 or CTLA4. This process, known as immune checkpoint blockade (ICB) in turn allows the T cells to perform their natural function and kill the tumor cells[74]. While ICB therapies have had strong successes in treating a number of solid tumors, they have not had nearly as dramatic effects in leukemia, though additional studies are ongoing[75–77]. However, a different type of immunotherapy, called CAR-T therapy, was recently approved by the FDA for relapsed/refractory ALL[78]. Chimeric antigen receptor T cell (CAR-T) therapy involves the *ex vivo* engineering and expansion of donor T cells (either autologous from the same patient or allogenic from a separate individual) to recognize and kill tumor cells with a specific antigen. In the case of relapse/refractory B-ALL, the CD19 B cell surface marker is used as the antigen to generate the CAR-Ts [79].

While a variety of therapies are available to patients with acute leukemia, there is still a significant need for more effective drugs. For adult ALL and AML, the 5-year survival rates remain below 50%[3,80]. While non-specific chemotherapies have historically been the first line of treatment for these diseases, future development of novel targeted therapies and immunotherapies are likely to improve outcomes in patients with leukemia with a reduction of the severe side effects associated with toxic chemotherapies.

1.2.4 Minimal residual disease (MRD) and relapse

Tumor burden in patients with leukemia are typically described by the number of cells in a blood or bone marrow biopsy (Figure 1.3)[81]. This allows for close monitoring of tumor burden and response to therapy. Acute leukemia is diagnosed when at least 20% of the nucleated bone marrow cells are immature cells, also called blasts[82,83]. Shortly following treatment, patients typically exhibit a drastic drop in tumor burden. This is often followed by a period of remission, with low or undetectable levels of disease.

There are several classifications that are used to describe the degree of remission. Complete remission (CR) is typically defined as less than 5% blast presence in a bone marrow biopsy and can be measured with a standard smear, making it a quick and relatively inexpensive test, but this does not mean that no tumor cells are present. A second, more stringent classification is the term minimal residual disease (MRD). Measuring MRD requires using more sophisticated techniques, such as flow cytometry and polymerase chain reaction (PCR) amplification to identify extremely rare cell populations. MRD is often defined as less than 0.1% detection of tumor cells in the bone marrow, though newer techniques continue to push that limit[84]. For this reason, the term "minimal residual disease" is being replaced by "measurable residual disease" to clarify that patients with disease seen only with advanced technologies (MRD+) do still have detectable disease burden, though it is very low[85].

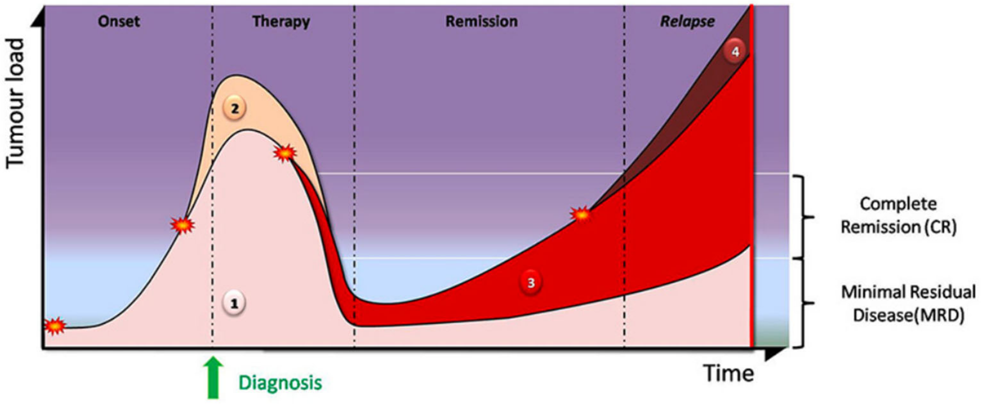

Figure 1.3 Tumor burden of leukemia over the course of disease and treatment[81]. Disease begins with a low number of cells that experience an exponential growth to at least 20% of total bone marrow cells, as the tumor undergoes genetic mutation. Upon effective therapeutic treatment, the number of tumor cells dramatically decreases. In a remission phase, tumors may experience a slow growth over time, and additional genetic or transcriptional changes may allow for the cells to rebound into another rapid growth relapse state. Complete remission (CR) and minimal residual disease (MRD) define clinical levels of detection to classify the degree of tumor burden.

The degree of MRD has been shown to correlate with patient survival time, with a lower MRD (fewer detected cells) being associated with better survival times[86–89]. However, in many types of leukemia, most patients who have MRD do eventually relapse, with disease that can be even more aggressive and harder to treat than the initial disease[90].

1.2.5 Mouse models of leukemia

Many mouse models exist for studying leukemias, with various benefits and drawbacks. One of the most common is adaptive transfer of syngeneic models. Similar to solid tumor syngeneic models, these cell line-based methods are derived from a donor mouse with identical genetic background. Cells removed from a donor are genetically engineered *in vitro* to express certain oncogenic mutations. These cells are then injected through the tail vein into the recipient mouse, where cells can home to the bone marrow and begin growing as a tumor[91,92]. Depending on the model, a pretreatment of the recipient mouse with irradiation or drug may be necessary to clear out sufficient space in the marrow for the cancer to efficiently seed. Syngeneic models are widely used because they are easily tractable and have relatively short timescales, taking only a few weeks to develop severe disease. Also, because they are based on cell lines, additional genetic manipulations, such as adding fluorophores to readily identify tumor cells or additional mutations to assess function of specific genes, is relatively straightforward to perform[93,94].

Another commonly used model category is PDX. Like in solid tumors, this involves the injection of human patient-derived tumor cells into an immunodeficient mouse to better study how the tumor of a specific patient behaves. While these models are often regarded as more clinically relevant, the lack of immune system in the mouse prevents the full understanding of how the cells of the normal immune system interact with the tumor cells[95]. Additionally, these models tend to seed relatively poorly, with only a fraction of patient tumors able to form PDX models. It can also take many months for disease to develop in the recipient mouse, making it challenging to rapidly iterate experiments with these models[96].

A final method of modeling leukemia in mice is through exposure to either radiation (gamma or X-ray) or viral infection. Low dose radiation can induce AML in mice and has also been associated with leukemia development in humans, so these models have been used to understand the clinical aspects of radiation-induced leukemias[95]. Several murine leukemia viruses (MuLVs) have also been discovered that can spontaneously induce AML leukemia in mice. While the use of these models has been important historically in understanding the development of leukemias, their use is limited. This is because many of the external stimulus methods often have low levels of incidence in tumorigenesis, with fewer than 50% of mice developing disease[97].

For the purposes of this project, we worked with two syngeneic models of leukemia. Our ALL model used the common Ph+ BCR-ABL transgene, either with or without the addition of a fluorophore[98,99]. We also used an AML model driven by the MLL-AF9 transmutation with an added fluorophore, which is one of the most commonly used AML models in the field[95,100].

1.2.6 Vascular adhesion molecules in leukemia

Leukemia cells rely on adhesion molecules for many reasons. Adhesion binding can allow circulating cells to affix to the vascular wall and exit from circulation. These molecules can similarly prevent cells in a bone marrow niche from escaping the marrow and entering circulation. It has been shown that leukemia cells can use their binding to adhesion molecules to alter their sensitivity to chemotherapies[100–102].

In order to more effectively home to their ideal bone marrow niches, leukemia cells evolved to coopt the adhesion molecules that normal white blood cells use to recognize binding proteins on endothelial cells and within the bone marrow. These molecules can be integrins, which bind to ECM proteins (such as collagen and fibronectin) and certain endothelial surface proteins; junctional adhesion molecules (JAMs), which bind to corresponding JAMs on endothelial cells; and certain glycans, which bind to the family of selectin proteins on endothelial cells[4,103].

Studies have shown that interfering with adhesion of leukemia cells can influence the efficacy of chemotherapy. One drug, uproleselan or GMI-1271, functions as an antagonist for E-selectin, one of the key proteins on endothelium which allows for white blood cell adhesion. Researchers showed that binding to E-selectin upregulated survival pathways in leukemia cells and decreased the efficacy of chemotherapy both *in vitro* and *in vivo*[100]. The same study demonstrated that inhibiting E-selectin increased the efficacy of chemotherapy in a mouse model of AML. An ongoing clinical trial in patients with AML has shown promising results using uproleselan to inhibit E-selectin binding in combination with chemotherapy[104]. Similar studies have explored integrin binding in ALL as a pathway for chemo-resistance [105,106]. By inhibiting the ability of ALL cells to bind to the ECM via their integrins, cells become significantly more susceptible to chemotherapies. They showed that this is due to a decrease in uptake of the drug because of changes the signaling pathways mediated by integrin binding.

It has also been demonstrated that interfering with adhesion expression can lead to an increased population of actively circulating leukemia cells. By blocking the binding to E-selectin, a significant number of cells shift from the bone marrow niche into the blood[100]. This further increases the efficacy of chemotherapy, as the leukemic cells cannot hide in their protective niches, and may be exposed to higher levels of drug in circulation than when they are trapped in the bone marrow.

1.3 Determining the kinetics of circulating cells

1.3.1 Techniques to identify CTCs in the blood of mice

The simplest method to estimate the blood concentration of CTCs in mouse models relies on *ex vivo* processing of blood samples. Because solid tumor CTCs exist at such low levels in the blood (ranging from 1-1000/mL)[107], at least 0.5-1mL is required to sample to get an accurate estimate of the blood concentration. Due to the small blood volume of mice (around 1.5mL), this often is done by euthanizing mice at various times post-dosing with tumor cells to collect sufficient volumes. There are a number of methods to identify CTCs *ex vivo*, often through the use of microfluidics to sort or capture the cells based on presumed properties[108]. These are typically separated into platforms that isolate based on physical properties, and those that isolate based on surface markers.

Physically, the most commonly used approach is to separate based on size, though alternative methods based on density or electrical properties have also been employed[109–111]. Because most CTCs are expected to be larger than a typical white blood cell (since they typically arise from large epithelial cells) many fluidic based approaches have been developed that separate based on cell volume. By taking advantage of inertial focusing, a process by which larger, more massive particles are pushed towards the edges of channels when flown along an arc, large CTCs can be quickly separated from smaller white blood cells, platelets, and red blood cells[112].

Another common method of separating CTCs from whole blood utilizes the expression of known biomarkers on the CTC surface. Researchers have designed numerous devices that are coated with antibodies for EpCAM (an epithelial marker expressed on many types of CTCs) or for proteins specific for the tumor type of interest[113–115]. The antibodies may be fixed just to the sides of the device, or complex arrays of pillars and walls may be present to maximize the likelihood of binding[116,117].

A final approach involves the use of pre-labeled tumor cells, either through radioisotope or fluorescence, to identify CTCs[118–120]. In these studies, fluorescent or radioluminescent microscopy of the blood sample can be employed to count the CTCs from a sample of whole blood. While all of these methods can be effective at detecting CTCs from the blood, they all rely on *ex-vivo* analysis of blood samples. This not compatible with real-time monitoring of tumor cells in the blood, as the concentration can only be determined at discrete timepoints, rather than through continuous monitoring.

In vivo flow-cytometry is one of the most effective methods to monitor CTC counts in real time[121,122]. In this setup, a mouse is anesthetized and an ear capillary is observed on a microscope to identify and enumerate fluorescent CTCs. While this method is able to be performed longitudinally (at different timepoints in the same animal), the mouse must remain anesthetized for the duration of monitoring, and only a small percentage of the blood is visualized. For the average mouse ear capillary, it would take tens of hours to scan through a full blood volume of a mouse[123]. As such, it this method is prone to high error, as only a small volume of blood is used to estimate the total concentration of CTCs in circulation.

1.3.2 Half-life estimations of CTC and CLCs

Observed clearance of CTCs and CLCs can occur from several avenues. Cells can be killed in circulation by immune cells, they can get stuck in capillaries due to their size, they can adhere to endothelial cells lining the walls through adhesion molecules, or they can fully extravasate and exit blood vessels. While it is difficult to distinguish between these possibilities, identifying the rate that tumor cells clear active circulation is vital to studying tumor cell trafficking.

Half-life time in the context of CTCs refers to the duration it takes for the concentration of CTCs in the blood to drop by 50%. Early studies aimed at defining CTC half-life time relied on using radioisotope-labeled cells injected into the blood of mice with euthanasia of mice at defined times post-injection[120,124]. These studies tended to estimate half-lives on the order of seconds, with nearly instantaneous clearance of the injected cells. Later studies using *in vivo* flow cytometry or serial patient samples reported half-lives on the order of minutes to hours, though an initial rapid clearance of a subset of CTCs followed by a slower clearance was often seen[125,126].

In vivo circulatory kinetics of normal myeloid- and lymphoid-lineage cells have been studied much more intensively than tumorigenic leukemic cells, often in the context of immune response to disease, such as HIV. Studies of the in vivo circulatory kinetics of autologous in vitro- or in vivo-radiolabeled granulocytes date back as far as 1959. These studies reported an *in vivo* half-life of granulocytes in humans to be in the range of 6-8 hours[127,128]. Fewer studies have examined the kinetics of leukemic myeloblasts, but those that have found that they have half-lives longer than those of granulocytes in healthy subjects, in both acute and chronic myelogenous leukemias[129].

Our lab has developed a CTC Counter platform that allows for the detection of fluorescent cells in the blood[130]. By combining an arterial-venous cannulation with a microfluidic chip and optical system, we can flow blood from the carotid artery of a mouse through our system and return it through the jugular vein, while detecting fluorescent events in the blood. Our system can process orders of magnitude more blood than a traditional *in vivo* flow cytometry system, and can scan through a full mouse blood volume in only 30 minutes, allowing for much more accurate measures of concentration than other real-time detection platforms.

In this project, we will use the CTC Counter system to extrapolate circulation kinetics of tumor cells in the blood. We will begin by developing a blood exchange method with two CTC Counters in series, and demonstrate through mathematical model the ability to estimate half-life time and generation rate of CTCs based on the steady-state transfer rates of cells between tumor bearing and healthy mice. Next, we will apply this method to several solid tumor CTC models and show that while generation rates can vary dramatically between disease models, the half-life time of solid tumor CTCs remains much more consistent. Finally, we will use the blood exchange system to determine factors that influence the clearance of leukemia CLCs. We will demonstrate that both disease status of the tissue and relapse status of the leukemia cells impact the clearance rates of CLCs, and that these changes are driven by increases in the expression of adhesion proteins on the endothelium and tumor cells.

2. Development of blood exchange platform

2.1 Background

Understanding the trafficking of tumor cells through the body requires an accurate measure of their kinetics. Several key features can define the kinetics, including generation rate (the number of cells being shed into circulation per unit time) and the clearance rate (the rate at which cells are removed from circulation, either through extravasation or immune killing). By studying these features, we can begin to see the factors, both intrinsic and extrinsic, that can modulate the circulation properties of these cells, potentially leading to the identification of new therapeutic targets.

Measuring the concentration of circulating tumor cells in the blood is incredibly important for understanding the ways that CTCs move throughout the body. But, while knowing the concentration of cells in the blood is important for understanding how the cells circulate, it is unable to decouple the various contributing factors, namely generation rate and clearance rate. A low circulating concentration could be defined either by a low generation rate (very few cells get into the bloodstream) or a very fast clearance rate (cells remain in the bloodstream for a very short time). In order to decouple these parameters, additional measurements are required, one for each variable, since it is not possible to calculate two independent variables from just a single measurement.

The simplest means to extrapolate clearance rate using only a concentration would be to remove the second variable, generation rate. By injecting fluorescent cells into an otherwise healthy mouse and monitoring the decay profile, the half-life time (time for the circulating concentration to drop by half) could be calculated solely by measuring the change in concentration over time. However, this method has a few key limitations. *In vitro* cultured cells have been shown to have dramatic differences to *in vivo* counterparts, ranging from cell cycle time to surface markers[131,132]. Additionally, the processing required to prepare cells for injection, including pipetting and centrifuging, can impart additional shear forces that could impact the behavior of the cells. Finally, particularly with CTCs, which exist in the blood at notoriously low concentrations (as low as 1-100 cells per mL), the injection of a relatively high concentration of cells for a clearance study could artificially impact the measured results. And injecting CTCs at a physiological concentration at the maximum allowed volume (~150µL for a mouse) could have as few as 10 cells, which would be insufficient to follow a decay profile. Because there are no mouse models with CTC generation but no clearance, there isn't a way to effectively measure the generation rate alone. One study from 1975 attempted to measure generation rate alone by collecting blood from a vessel exiting a subcutaneous tumor over the course of 15-30 minutes while replenishing the lost blood volume with blood from a healthy animal and quantifying CTCs in the collected blood[133]. However, several caveats exist for this method, including the choice of model (subcutaneous cell line models are typically less metastatic than GEMM or organoid derived models) and uncertainty in whether all cells were collected (many vessels often exit a tumor).

A different approach to extrapolate the two primary circulation kinetic variables (generation rate and half-life time) would be to add an additional measurement. This could be accomplished by connecting the circulation of a tumor bearing mouse (with both a CTC generation rate and clearance rate) to a healthy mouse (that can clear CTCs but not generate CTCs) and monitoring the changing concentrations between the mice. The primary way historically to exchange blood in real-time between animals is through parabiosis. In parabiosis, skin flaps from the backs of two animals are sutured together, and after one to two weeks of healing, blood vessels form between the animals, creating a shared circulation. It is estimated that up to 1% of the blood can be exchanged per minute, but the rate is highly variable depending on the degree of revascularization and inflammation. Additionally, it is difficult to confirm the volume of blood transfer between the animals, which complicates the ability to effectively calculate circulation parameters[134,135]. And using *in vivo* flow cytometry to estimate real-time concentrations on the two animals would be nearly impossible, since the mice are conjoined and thereby would require two confocal microscopes with viewing windows only inches apart.

In this chapter, we develop a blood exchange system capable of extrapolating circulation kinetics of CTCs, by connecting the circulation of active, non-anaesthetized mice in a highly controlled manner using arterial and venous catheterization. Each mouse is housed separately, and pumps are used to flow blood between the mice at defined rates. Home-built fluorescent detection systems monitor the transferred blood for the fluorescent CTCs, and by connecting a tumor-bearing donor animal to a healthy naïve recipient mouse, the circulation kinetics of CTCs can be effectively extrapolated. We show a mathematical model for extrapolating generation rates and clearance rates from the paired circulation of tumor bearing and naïve mice, and demonstrate improvements to the system of sorted cell purification that will allow for more reliable sequencing results. Many of the results from this chapter were published in 2021[136].

2.2 Real-Time CTC-Counter Platform

Our lab has developed a system that can identify fluorescent cancer cells in the blood stream of live, unanesthetized mice in real time[130]. Using a genetically fluorescent tumor model, we perform a surgical cannulation of the carotid artery and jugular vein of the mouse, allowing temporary access to the circulatory system. The mouse is then connected to an optofluidic platform (CTC-Counter), which combines a microfluidic chip with a laser detection setup, to enable real-time identification of fluorescent cells from whole blood. A series of beam splitters and mirrors are used to split the 532 nm laser beam into two, and a cylindrical lens focuses the beam spots into lines, which are projected past a dichroic mirror (long pass 550nm) across the flow channel approximately 400µm apart. The emitted light (581 nm) passes through the dichroic, and is focused through a spherical lens onto a PMT. In this way, fluorescent cells can be detected by a signature double peak (as the cell passes through the two consecutive laser lines) on the LabVIEW control instrument (Figure 2.1).

This system of real-time detection has several main benefits over other methods of CTC enumeration. First, mice remain awake and alert throughout the duration of the experiment, allowing for longer scanning times. Additionally, by sampling through the carotid artery, rather

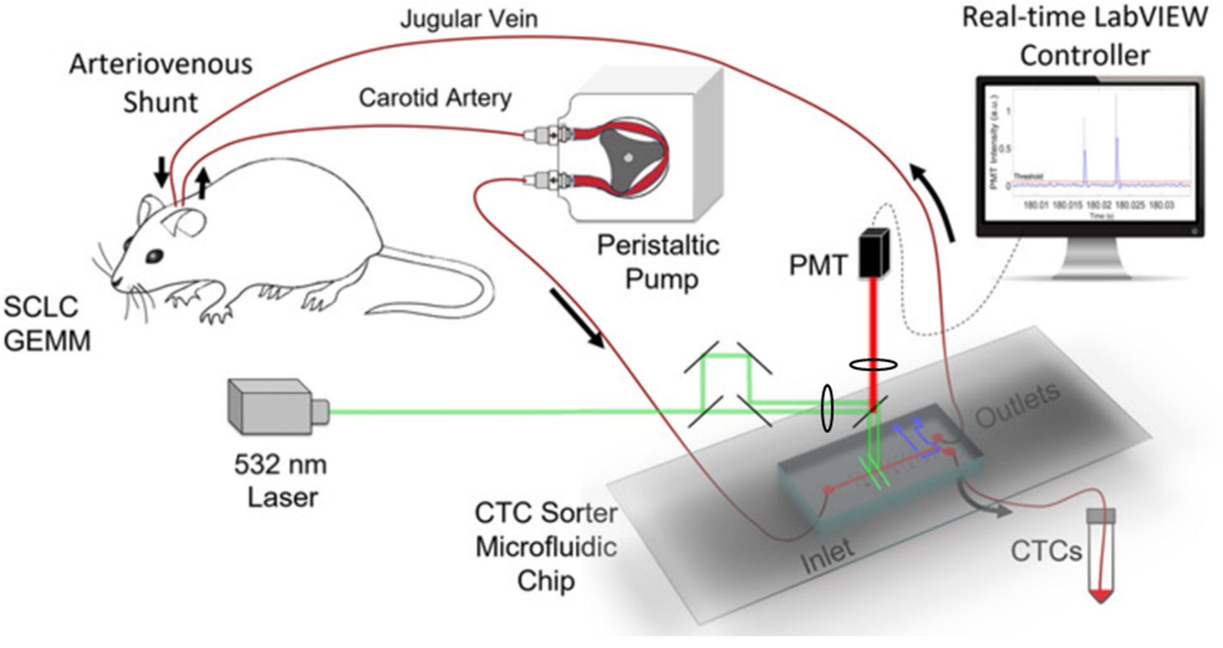

Figure 2.1 Schematic of CTC-sorter platform for scanning the blood of mice in real-time to identify fluorescent tumor cells, with the capacity to sort out CTCs in a small blood volume[130]. A mouse with arteriovenous shunt is connected via peristaltic pump to a microfluidic chip. A series of laser lines are projected onto the chip, and a detection photomultiplier tube (PMT) records the fluorescent data, which can be interpreted externally through LabVIEW software to identify fluorescent cells via their double-peak. This data can additionally be used to estimate the velocity of fluorescent CTCs, and a set of valves can be used in CTC collection experiments redirect small volumes of blood to collect CTCs in-line from the bloodstream of mice.

than an ear capillary, a larger volume of blood can be sampled, allowing for greater confidence of concentration estimation. Finally, since the system involves a pump and *ex vivo* optofluidic system, additional processes, such as direct sorting of CTCs from blood, or in-line injection of reagents, is made possible.

The CTC detection platform was tested in a small-cell lung cancer (SCLC) mouse model to validate the detection capabilities. Table 2-1 shows that the real-time scan of mouse blood using this system correlates with the concentration of CTCs detected in a terminal blood sample, demonstrating that the system can accurately determine the blood concentration of fluorescent cells.

The first use of the CTC detection platform was to sort out the fluorescent CTCs in real time in order to assess the transcriptional evolution of the cells over the course of treatment. Mice exposed to JQ1 (a bromodomain and extra-terminal motif protein inhibitor) showed a pronounced change in transcriptional expression of sorted CTCs over the course of 5 days[130]. This system provided a unique ability to sequence CTCs from the same animal over time, a feat that had historically been limited by the small blood volume of mice and the inability to collect sufficient CTC numbers without a terminal bleed. And by looking at transcriptional changes within the same animal, transcriptional changes were unmasked that would have been obscured using traditional methods of longitudinal takedowns[130].

	CTCs/mL	
Exp #	Real-Time Scan	Terminal Blood
1	400	318
2	893	505
3	287	296
4	555	458

Table 2-1 Comparison of CTC detection levels between a real-time scan and terminal blood from the same animal shows consistency of detection rates

2.3 Blood Exchange System

By connecting two of the CTC detectors in sequence, we were able to develop a method to circulate blood between animals without the need for parabiosis. Two cannulated mice, each connected to a separate peristaltic pump and fluorescent detection system, can have blood exchanged between them with accuracies of 0.1µL/min, ensuring an even exchange of blood. Mice connected in this way can be fully awake and active and perform normal eating, nesting, and grooming activities while connected to the system. By minimizing the distance between detection platforms, and by minimizing the interior diameter of the connective tubing (Figure 2.2A), we were able to reduce the *ex vivo* blood in the system to around 100-150uL, less that one tenth of the mouse's total blood volume, to prevent negative impacts of blood loss on the mice. Exchanges were well tolerated, and mice kept on the system for several hours still had normal behavior. Healthy mice exchanged on the system had normal survival and have been followed for many months without incident.

We also demonstrated that cells are not lost in the tubing and that the systems are equally good at detecting the fluorescent cells. Approximately 400 fluorescent SCLC cells were added to two connected CTC detection systems. The cells flowed sequentially through the pair of systems 5 times, and the resulting detections were monitored, showing no difference in detection and minimal losses (Figure 2.2B).

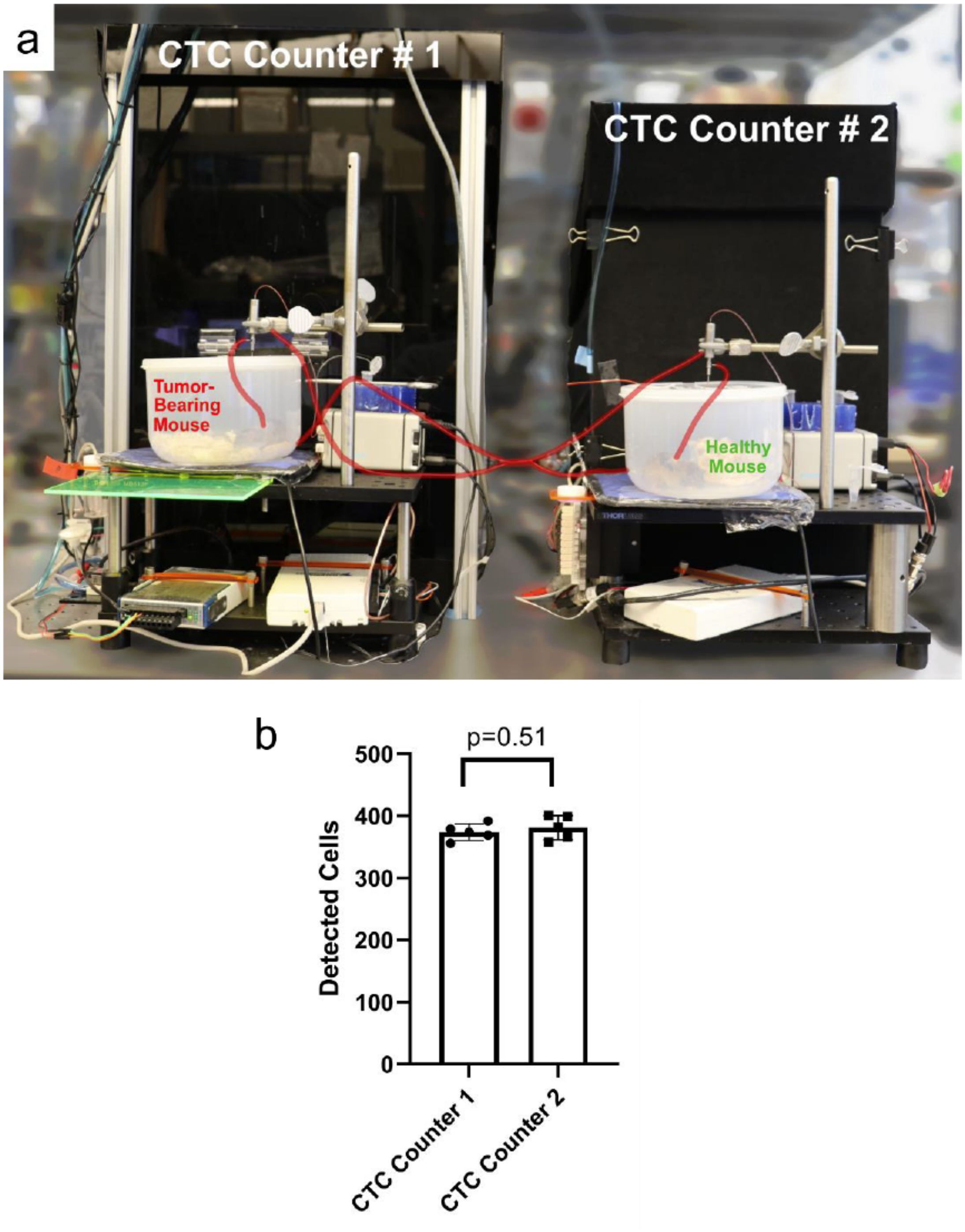

Figure 2.2 Blood exchange system. (a) Two mice (in this setup a tumor-bearing mouse and a healthy mouse) in individual containers are connected via tubing (highlighted in red) to a CTC Counter and each other. (b) Cells circulated five times through the sequentially connected systems demonstrate minimal cell loss and equivalent levels of detection across systems.

2.4 Modeling to Extrapolate Circulatory Kinetics

In order to understand the varying circulation concentrations and metastatic propensities of solid tumor CTCs, it is important to characterize the kinetic properties of CTCs in the blood. The two predominate parameters that define the circulation kinetics are the generation rate (rate at which CTCs enter circulation through intravasation from the primary tumor) and half-life time (the time it takes for the circulating concentration of CTCs to decrease by 50%). In order to quantify these properties, we developed a mathematical model to describe them in the context of blood exchange at steady state.

As shown in Figure 2.3, blood exchange can be conceptualized as the flow between two well-mixed containers representing the circulatory volume of the two mice. In this model, the fluid (blood) is pumped between the two containers, transferring red spheres (CTCs) between the containers at rates r_1 and r_2. CTCs are released into the container representing the tumor bearing mouse (TBM) at rate r_{gen} and are removed from each container (representing extravasation) at a

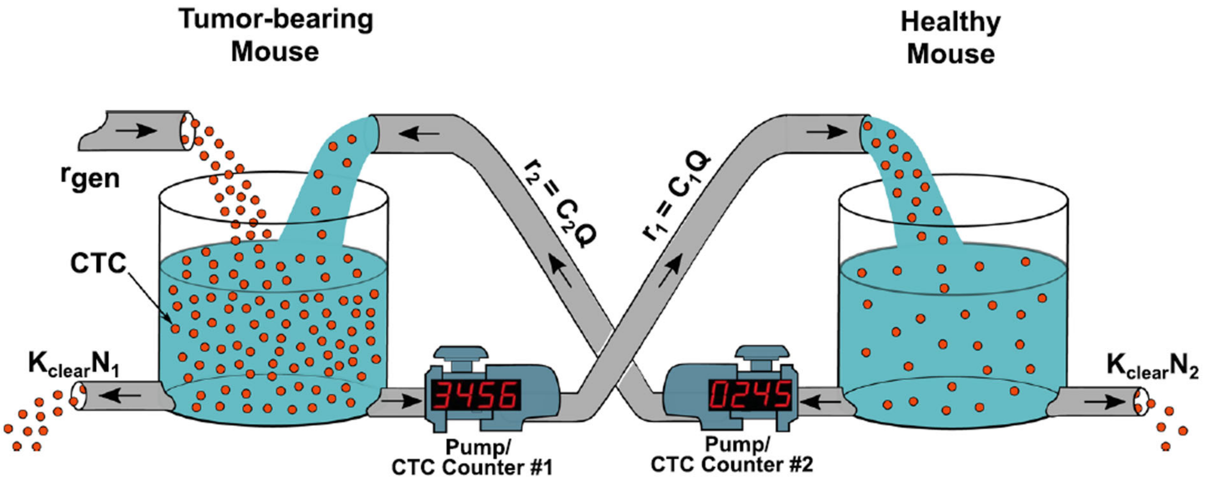

Figure 2.3 Model for blood exchange. The concentration of CTCs in the tumor-bearing and healthy mice in a blood exchange setup can be modeled as the mixing of CTCs (red) between two well-mixed containers. CTCs are shed at a rate r_{gen} from the tumor-bearing mouse into circulation. CTCs can be cleared by either animal as a first-order decay

rate equal to $K_{clear}n$, where K_{clear} is a first-order rate coefficient and n_1 and n_2 are the total number of CTCs in each container.

Using the assumption of first order decay kinetics, CTCs stay in circulation for a half-life time of $t_{1/2}$, where $t_{1/2} = \ln(2)/K_{clear}$. The differential equations to describe the changes with respect to time of the total number of CTCs in each mouse can be defined as:

$$\frac{dN}{dt} = rate\ of\ CTCs\ in - rate\ of\ CTCs\ out \qquad \textit{(2-1)}$$

$$\text{Tumor-bearing mouse: } \frac{dn_1}{dt} = -C_1(t)Q + C_2(t)Q - K_{clear}n_1(t) + r_{gen} \qquad \textit{(2-2)}$$

$$\text{Healthy mouse: } \frac{dn_2}{dt} = C_1(t)Q - C_2(t)Q - K_{clear}n_2(t) \qquad \textit{(2-3)}$$

In these equations, Q is the volumetric flow rate of the pump (set at 60 µL/min), C_1 and C_2 are the concentrations of CTCs in the TBM and healthy mouse (HM) respectively, and n_1 and n_2 are the total number of cells in the TBM and HM respectively, so n=C x V, where V is the total blood volume of the mouse.

By using the above equations, we can extrapolate both the generation rate (r_{gen}) and half life time ($t_{1/2}$) of CTCs based only on the steady-state transfer rates r_1 and r_2, where r = C x Q. By setting dn/dt=0, we get the following equations:

$$r_{gen} = (r_1 - r_2)\left(1 + \frac{r_1}{r_2}\right) \quad \left[\frac{CTCs}{min}\right] \qquad \textit{(2-4)}$$

$$t_{1/2} = \frac{(V/Q)\ln(2)}{r_1/r_2 - 1} \quad [min] \qquad \textit{(2-5)}$$

An overview of the experiment is shown in Figure 2.4. The CTC-Counters connect the blood of the TBM and HM and allow for fluorescent detection of the blood of each animal using a laser and a photomultiplier tubes (PMT).

In post-processing of a blood exchange experiment, the raw PMT data was fed through a MATLAB program to identify the signature double-peak shape of the CTCs (due to cells passing through the two sequential laser lines) (Figure 2.4b and inset). The cumulative count was then plotted in order to follow the changing concentration of the CTCs in the blood of the mice. The plots of the cumulative CTC counts in the TBM and HM of a representative blood exchange are

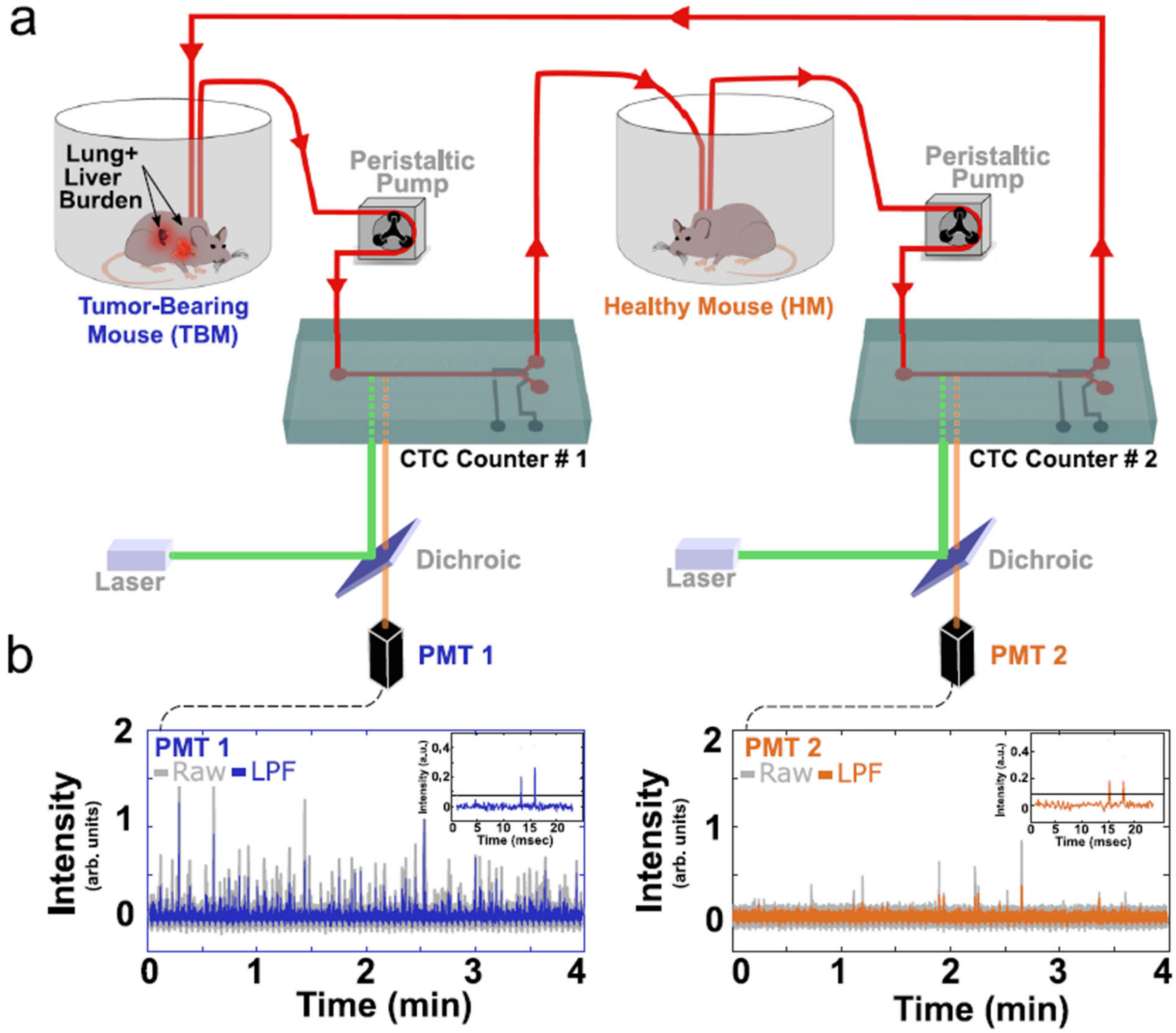

Figure 2.4 Blood exchange setup for CTC detection. (a) Schematic showing the connection of circulation between two animals, a tumor-bearing mouse (TBM) and a healthy mouse (HM) via CTC-Counter systems. For each device, a laser excited fluorescent tumor cells as they flow through the chip, and the emitted light passes through a dichroic filter, where it is measured by a photomultiplier tube (PMT). (b) Readout of the PMTs show a high number of peaks (CTC detections) in the TBM and fewer detections in the HM. LPF- low pass filtering (of raw data for analysis). Inset shows the expected double-peak signal of a single CTC passing through the laser lines.

shown in Figure 2.5. The final segment of the exchange is estimated to be a steady-state exchange, confirmed by the constant slope of the cumulative count curves, and can be used to estimate the circulation kinetics.

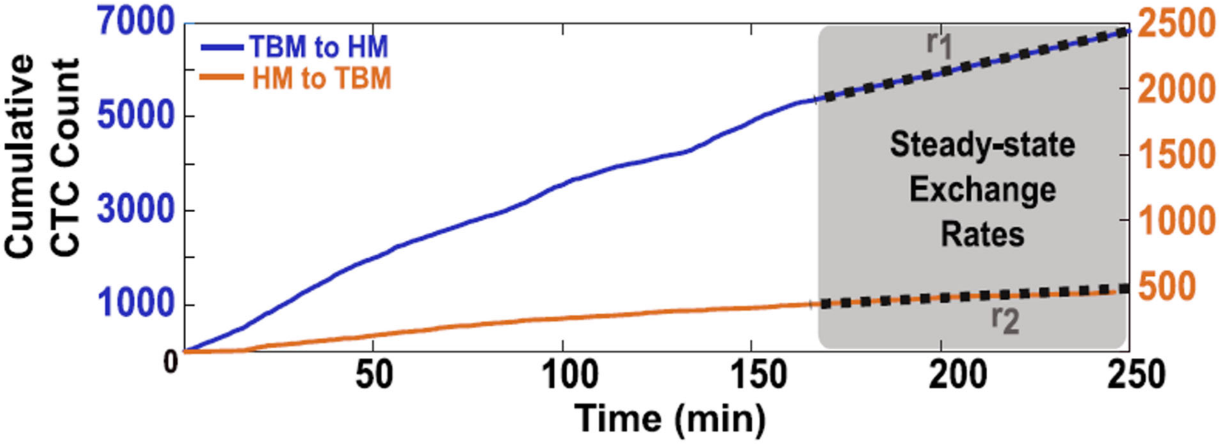

Figure 2.5 Representative detection profiles throughout a blood exchange experiment. Blue lines represent the cells detected in the blood of the TBM that will be infused into the HM, while the orange line indicates the cells detected in the HM that will be returned back to the TBM.

2.5 Sorting and purification of CTCs

2.5.1 Chip fabrication

One of the key features of the CTC detection system in its development was the capacity to sort out CTCs directly from the bloodstream. The design of the microfluidic chip is a two-layer PDMS device, in which the valve layer can be pressurized to seal off outlets of the channel layer (Figure 2.6).

The top layer is the channel layer, which has a “Y” shaped path with one inlet and two outlets (as shown in Figure 2.4a). This layer is fabricated on a silicon wafer using a positive resist photolithography method. AZ4620 a positive photoresist, is spun to approximately 45-50µm in height and baked onto silicon wafers, and a mask is used to protect the desired "Y" channel shape from UV exposure, which makes the resist soluble in developer. After development, which leaves just a "Y" shaped section of AZ4620. A brief reflow heating allows for the smoothing of the photoresist channels, leaving a parabolic cross section in the channel, which will allow for more ideal valve sealing in future steps.

The bottom layer is the valve layer, which has two paths, each of which can intersect with the outlets of the channel layer when aligned properly. This layer is fabricated using negative photoresist on silicon. SU8 is spun on the wafer to approximately 50µm, and a negative mask is applied in order to cross-link the SU8 photoresist into the desired valve design.

To create the microfluidic chips, PDMS is thoroughly mixed at a 1:10 base elastomer to curing agent ratio and degassed to remove air. The channel layer is prepared by pouring a thick ~1cm layer of PDMS on the channel silicon mold, whereas the valve layer is prepared by spinning approximately a thin 30-50um layer of PDMS onto the valve silicon mold. After baking to cure the PDMS, the pieces are exposed to oxygen plasma and carefully aligned to covalently bind the layers. After punching 50um diameter holes for the channel inlets, channel outlets, and valve inlets, the chip and a glass slide are exposed to oxygen plasma and affixed together. At this point,

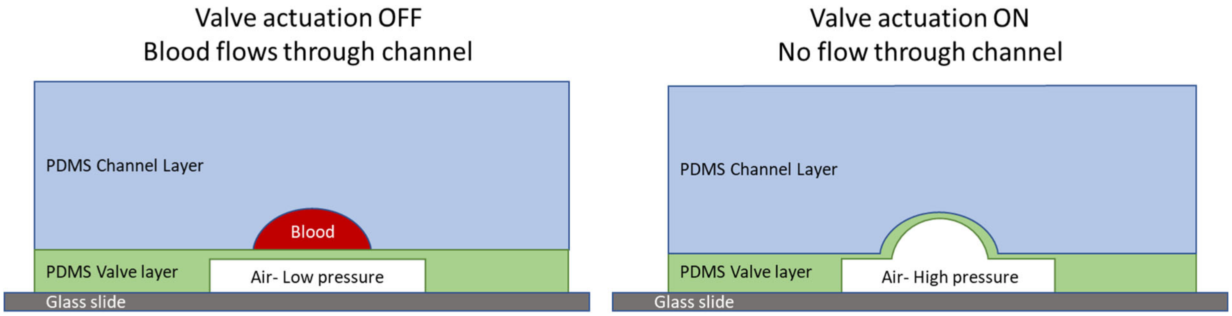

Figure 2.6 Cross section of 2-layer microfluidic chip showing valve operation. The device is made from thin valve layer with a thick channel layer on top bonded to glass. In the open channel position (left), low pressure in the valve layer allows for blood to flow in the semicircular shaped channel. To actuate the valve, a high pressure is applied, which deflects the thin valve layer up into the channel, forming a seal and preventing flow.

pressurization of either valve will deform the thin valve layer up into the channel layer, thereby sealing off the outlet that it is covering. The semicircle cross section of the channel layer is important to ensure a proper seal to effectively control which outlet is being used. During standard operation, one outlet of the "Y" shaped channel is closed by the valve, such that all of the blood passing through the device returns to the mouse. When a cell passes through the laser lines and generates the double peak fluorescent signature, the velocity can be estimated based off the known physical distance between the laser lines. Then the valves can acuate to shunt blood into the second outlet of the "Y" shaped channel and remain open based on the estimated velocity and the known distance to the valves. This system allows for the real-time sorting of small blood volumes containing single CTCs in approximately 50nL of blood.

2.5.2 Improvements to purification of sorted CTCs

After sorting CTCs in small blood volumes, further purification is necessary to perform downstream analysis of either microscopy (where significant, but non-perfect purification is needed) or RNA sequencing (where single cell purity is required). This is due to the incredibly concentrated nature of cells in the blood. A single microliter of blood can contain 10 million red blood cells, 100 thousand platelets, and 10 thousand white blood cells, in addition to the single sorted CTC. White blood cells have by far the most RNA of the blood cells, so are the most crucial to remove from a sample containing CTCs, as they will add the most noise to sequencing results. Even after the removal of white blood cells, the sheer number of red blood cells and platelets can result in a significant amount of noise to either microscopy or sequencing. Therefore, massive purification is necessary to reduce the background noise and allow for identification of CTCs in downstream processing.

The historical method of purification used in our lab involved chemical processing and antigen-based cell depletion. The first step was red blood cell lysis using ACK buffer, which selectively interferes with red blood cell specific water transporters, resulting in water accumulation and subsequent cell bursting[137]. This process is around 99% efficient, which still leaves up to several hundred red blood cells per CTC. Magnetic activated cell sorting (MACS) was then used to deplete out white blood cells. This method also has up to 99% efficiency, which leaves up to 10 white blood cells per sorted CTC[138]. The final step was a dilution, followed by resorting on the optofluidic CTC detection system as described earlier. By diluting the cells 1:50 and resorting based on fluorescence, each final sort contained on average 200 red blood cells and 0.2 white blood cells.

While this has been an effective method to purify CTCs from whole blood, one major issue is that this purification process does not remove platelets. Over 1000 platelets can be sorted per single CTC, which led to difficulties in analyzing RNA sequencing due to the overwhelming platelet signature. We therefore aimed to develop a more efficient sorting technique that could overcome the limitations of the previous methods.

A new sequential sorting method of fluorescent CTCs was pursued as an improved way to isolate single CTCs from whole blood. Since our CTC sorters are capable of robustly sorting out fluorescent cells in very small volumes, repeated dilution and sorting of CTCs in the same CTC sorter addressed many of the limitations of the MACS-based purification. Not only was this new method capable of reducing contamination of all blood components including platelets, but it also reduced the need for harsh chemicals and minimized the various processing steps of centrifugation, column purification, and heavy pipetting, which can decrease cell viability. This method also slightly reduced the duration of purification, taking about 30-45 minutes instead of 1 hour to go from whole blood to purified CTCs.

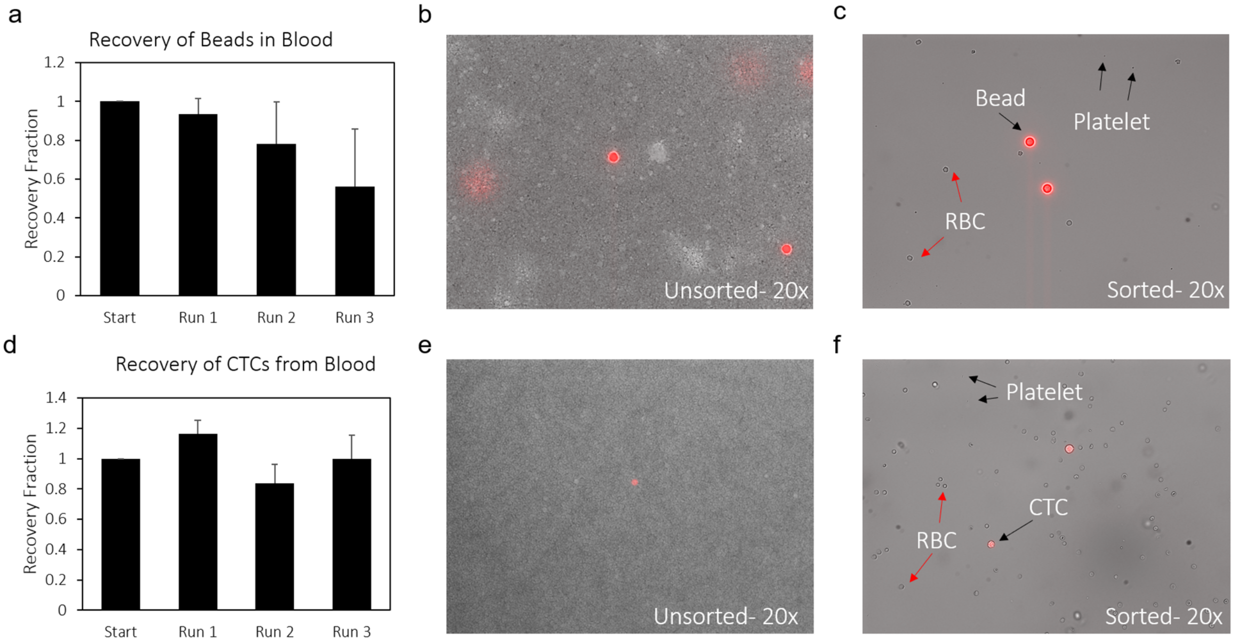

Figure 2.7 Recovery efficiency using sequential sorting purification. (a) Recovery fraction (cells/beads sorted divided by total at the start of each dilution step) of fluorescent beads spiked into blood and sorted via sequential sorting. (b) Unsorted and (c) third sort of beads purified through the sequential sorting method show effective depletion of all blood cell types. (d) Recovery fraction at each dilution step of sequential sort for CTCs sorted from a blood of a late-stage SCLC tumor bearing mouse. (e) Unsorted and (f) third sort of CTCs shows massive depletion of all cell types. The sorted samples would have one final purification sort before sequencing.

In sequential sorting, the CTCs, which have been sorted in 0.1uL each, are diluted off-chip 1:25 in either media or PBS. The subsequent dilution is passed through the CTC sorter again, effectively depleting all of the non-fluorescent cells (red blood cells, white blood cells, and platelets) 25-fold with each pass. After three rounds of purification, the cells are diluted a final time at 1:50, and sorted out for sequencing. With this method the effective dilution of each blood

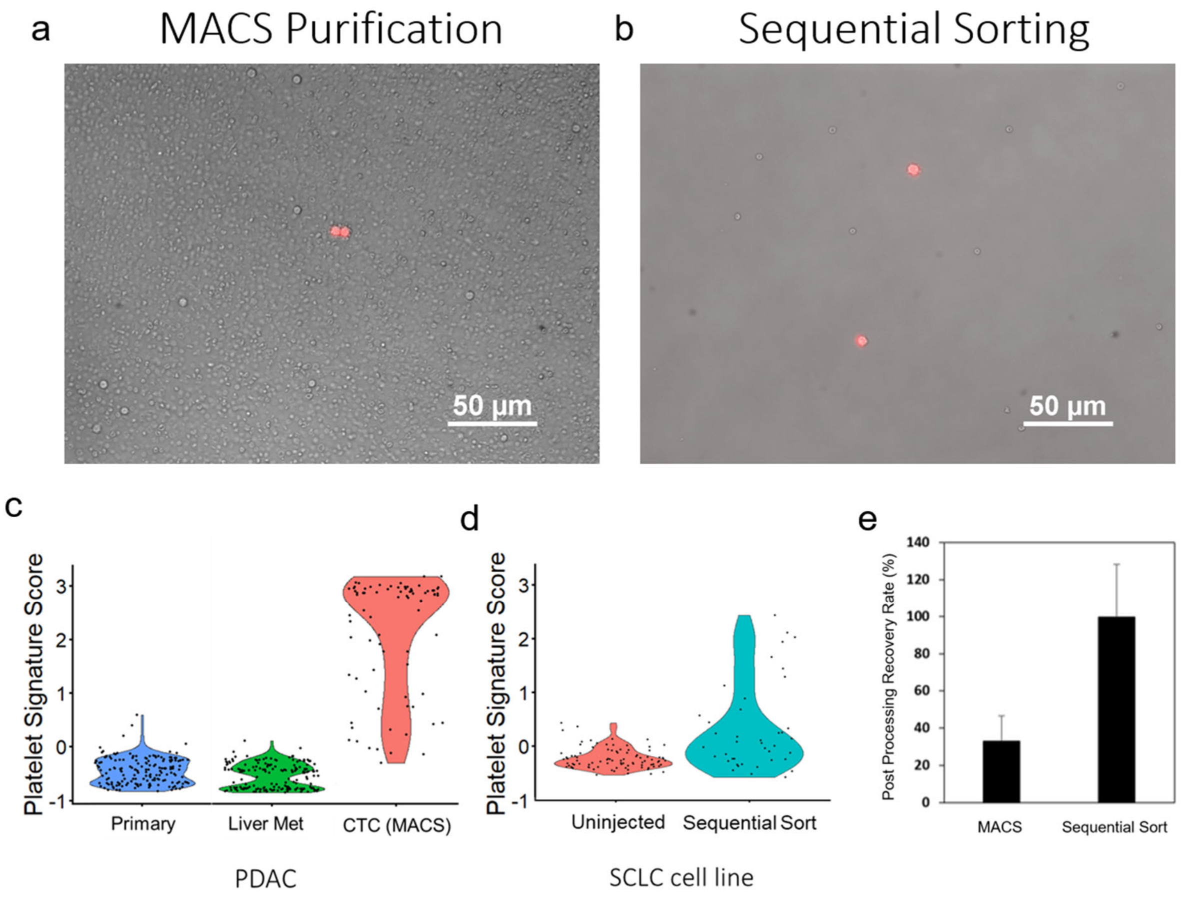

Figure 2.8 Improved purification of CTCs through sequential sorting. (a) Images of the final sort form the MACS purification method shows several red blood cells (larger white circles) and tons of smaller platelets. (b) Sequential sorting effectively removes plates and white blood cells and leaves very few red blood cells. Each image contains the total area of just under 2 final purified sorts for sequencing. (c) Single cell RNA sequencing in a PDAC model shows that CTCs purified via the MACS purification process have very elevated platelet signature compared to either primary tumor or liver metastasis cells. (d) Single cell RNA sequencing shows that sequential sorting of an SCLC cell line spiked into blood (Sequential Sort) results in a similar platelet signature to cells directly from culture that were never exposed to blood (Uninjected). (e) Sequential sort results in nearly full recovery of SCLC CTCs spiked into blood, while the excess processing and harsh reagents of the MACS methods results in only a 30-40% recovery rate.

cell type is 25x25x25x50, or nearly 800,000. This means that the final number of blood cells per CTC at the last sort should be on average 1.3 red blood cells, 0.0013 white blood cells, and 0.09 platelets, showing the sequential sorting has the potential to fully remove white blood cells and platelets and leave very few red blood cells, resulting in a very pure CTC for downstream sequencing. This efficiency can be seen in Figure 2.7, where both beads spiked into blood (a-c) and CTCs isolated from diseased SCLC mice (d-f) showed high recovery and purification efficiency.

In comparison to the MACS method of red blood cell chemical lysis and white blood cell magnetic depletion, sequential sorting outperformed in several aspects. By microscopy, it was clear that the MACS method left a large number of platelets (Figure 2.8a), whereas sequential sorting removed nearly all platelets and other contaminating blood cells (Figure 2.8b). RNA sequencing clearly demonstrated this difference in purification efficiency. Using the AddModuleScore function in Seurat 2.0 with an input set of known platelet genes, we assigned a gene signature score to sequenced cells indicating the overall expression of platelet-related markers, and indicating the degree of platelet contamination. Single cell sequencing of CTCs isolated from late-stage PDAC GEMM mice and sorted via the MACS method had a high platelet gene signature, indicating that this purification method left residual platelets in the sorted volumes (Figure 2.8c). However, single cells from a SCLC cell line that were spiked into blood and then purified via the sequential sorting method showed a similar platelet score to that of cells that were not spiked into blood, and therefore had no exposure to platelets (Figure 2.8d). Finally, the recovery rate using the sequential sorting method was significantly higher than with the MACS method (Figure 2.8e). Using MACS, only 30-40% of cells were recovered in the final sort, likely due to the off-chip processing of centrifugation, column filtering, and pipetting combined with the various chemical reagents. However, the sequential sorting method vastly improved this recovery rate, and nearly 100% of the starting cells could be recovered.

In this chapter, we developed a method for extracting the generation rate and half-life time of CTCs in mouse models of cancer. By connecting two CTC detection platforms in series, blood could be flowed between a tumor bearing and healthy mouse. We created a mathematical model to describe the system and extract circulation kinetics based on steady-state transfer rates between the mice. Finally, we improved our purification method through the use of sequential dilution of cells to generate sorted CTCs with higher purity for RNA sequencing analysis.

3. Blood exchange for solid tumor CTCs

3.1 Background

Estimates of clearance rates of CTCs in solid tumors have varied wildly, from near instantaneous clearance to hours-long clearance[125–128]. These measurements typically are performed from the injection of cultured cell lines into mice, rather than naturally arising CTCs. The development of the blood exchange method in Chapter 2 provides an opportunity to develop more accurate measure of circulation kinetics. By using the blood exchange method, we aim to better describe the clearance kinetics of CTCs, and explore how these rates vary between models of cancer.

In this chapter, we apply the blood exchange technique to a series of solid tumor models, and find that while generation rate of CTCs varies dramatically over several orders of magnitude across tumor types, the half-life remains fairly constant, with only a 2-fold difference. We then show that *in vitro* cultured cell lines clear at a significantly faster rate when injected into mice compared with naturally arising CTCs. Finally, we demonstrate the utility of the blood exchange system to seed metastatic tumors in healthy naïve mice, opening the possibility of studying metastasis in models that are limited by rapid growth of aggressive primary disease. Many of the results from this chapter were published in 2021[136].

3.2 Estimation of CTC circulation kinetics

To validate the mathematical model of blood exchange, experiments were performed utilizing murine models of three solid tumors. Five blood exchanges were carried out utilizing a genetically engineered mouse model (GEMM) of small cell lung cancer (SCLC) in Trp53$^{fl/fl}$; Rb1$^{fl/fl}$; Pten$^{fl/fl}$; Rosa26$^{LSL\text{-}tdTomato/LSL\text{-}Luciferase}$ mice that utilizes Cre recombinase-expressing adenovirus delivered intratracheally to initiate tumors[12]. Upon late-stage disease, as measured by bioluminescence via intravital imaging system (IVIS) (Figure 3.1a), Tumor bearing mice (TBMs) and healthy mice (HMs) were catheterized, and blood exchanges were performed. The traces of CTC detection for each of these experiments can be seen in (Figure 3.2b). In these graphs, the cumulative counts were plotted for both CTCs detected exiting the tumor-bearing donor mouse (TBM to HM, blue, left y-axis) and CTCs detected exiting the healthy mouse (HM to TBM, orange, right y-axis). The last 30-60 minutes of the exchange was used to estimate steady-state transfer rates of the cells (dashed lines r_1 and r_2). The slopes of these lines were then incorporated into the equations developed in Chapter 2 to calculate circulation kinetics.

Fourteen blood exchanges were carried out utilizing three models of PDAC, all in Kras$^{LSL\text{-}G12D/+}$; Trp53$^{fl/fl}$; Rosa26$^{LSL\text{-}tdTomato/LSL\text{-}tdTomato}$ mice (KPT). Thirteen blood exchanges were carried out utilizing an organoid model initiated by orthotopic transplantation of murine PDAC organoids (eight utilizing syngeneic organoids and five utilizing a syngeneic organoid harboring a defined neoantigen, SIINFEKL). One blood exchange was carried out utilizing an GEMM PDAC model initiated by a Cre recombinase-expressing adenovirus delivered via retrograde pancreatic duct injection to initiate tumors. Finally, five blood exchanges were carried out utilizing a GEMM non-small cell lung cancer (NSCLC) model in KPT mice that utilizes Cre recombinase-expressing adenovirus delivered intratracheally to initiate tumors.[24,] Figure 3.2 shows calculated generation rates (a) and half-life times (b) from these blood exchange experiments. Generation rate varied drastically between and within models over three orders of magnitude, while half-life time was relatively consistent between these three solid tumor models and only varied by a factor of around two.

The SCLC model utilized in these studies had a significantly higher CTC generation rate when compared to the PDAC and NSCLC models. This finding is consistent with the observations that the murine SCLC model utilized has higher CTC concentrations when compared to the other solid tumor models and is more prone to forming metastases[139]. It suggests that these phenomena

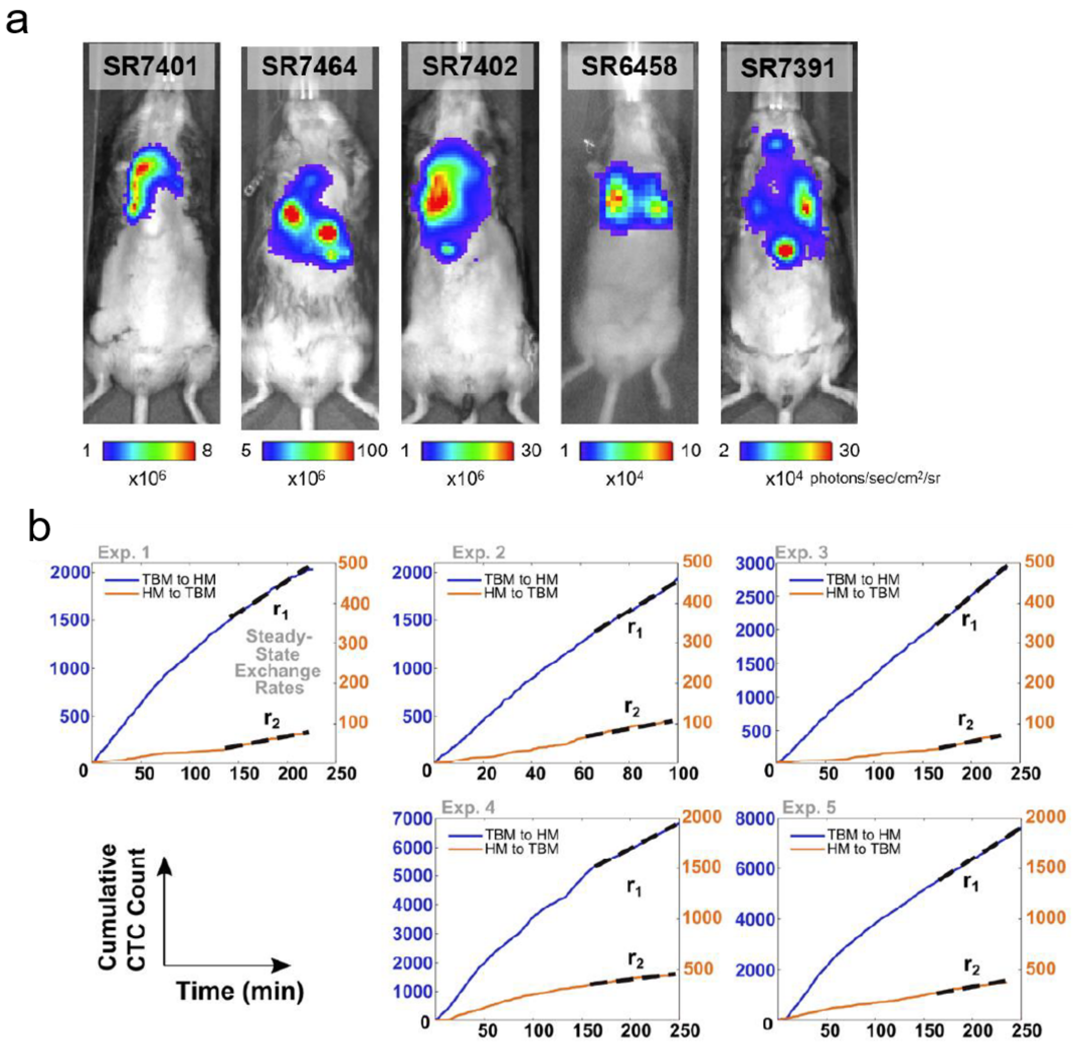

Figure 3.1 Blood exchange tracings for SCLC mice. (a) IVIS imaging showing tumor burden of TBMs shortly before blood exchange experiments showing severe lung disease. (b) Cumulative counts of CTCs exiting TBMs (TBM to HM, blue, left y-axis) and HMs (HM to TBM, orange, right y-axis) over the course of blood exchange. Steady state exchange rates (r_1 and r_2, dashed) were used to later estimate circulation kinetics.

are due to a higher CTC generation rate compared to other oncological models, rather than a longer CTC half-life time. Because the models develop over different time courses a direct comparison of generation rate is difficult to directly compare between models, as the stage of disease is difficult to universally quantify. After intratracheal injection of Ad5-CGRP-Cre virus (2E6 pfu/mouse) into mixed background C57BL/6;129/Sv mice, SCLC typically develops over the course of 6-7 months, with CTCs first becoming detectable around 4-5 months post inoculation. Blood exchange experiments in this model were performed between 5 and 6.5 months after tumor initiation. The PDAC models, which are all initiated by syngeneic orthotopic transplantation of organoids into C57BL/6 mice, develops on a much faster timeline, with mice succumbing to disease at around 8-10 weeks post initiation, and CTCs first being detected at around the 6-week timepoint. For these models, blood exchange experiments were performed between 7 and 10 weeks post implantation. The NSCLC model was initiated via intratracheal injection of AD5-mSPC-Cre virus (1E6 pfu/mouse) into C57BL/6 mice, and tumors develop over the course of 3-4 months. Blood exchanges in this model were performed around 3-4 months post tumor initiation.

In order to compare the generation rates, we normalized the generation rates to the estimated tumor masses to determine the number of CTCs shed per day per gram of tumor, as well as the percent of tumor shed per day (Table 3-1). Lung tumor mass was estimated by subtracting the weight of healthy lungs of age-matched mice from the diseased lung at late-stage disease. We found the tumor mass to be approximately 450-605 mg for SCLC at late-stage disease, and 150-500 mg for NSCLC tumors. PDAC tumor volume was measured from ultrasound imaging using Vevo LAB software (FUJIFILM Visualsonics, Inc). The corresponding tumor mass was estimated using a linear regression of previously recorded tumor mass and volumes. For all tumor types, total number of cells was calculated from the assumption that 1g tumor has roughly 10^9 cells[140]. Our calculations demonstrate shedding rates ranging from 20k-700k/day/g tumor, significantly lower than previous estimates of 3-4M CTCs/day/g tumor[133].

A detailed breakdown of the calculated variables for the full set of blood exchange experiments can be found in Table 3-2. This includes the volumetric flow rate (Q), volume of the

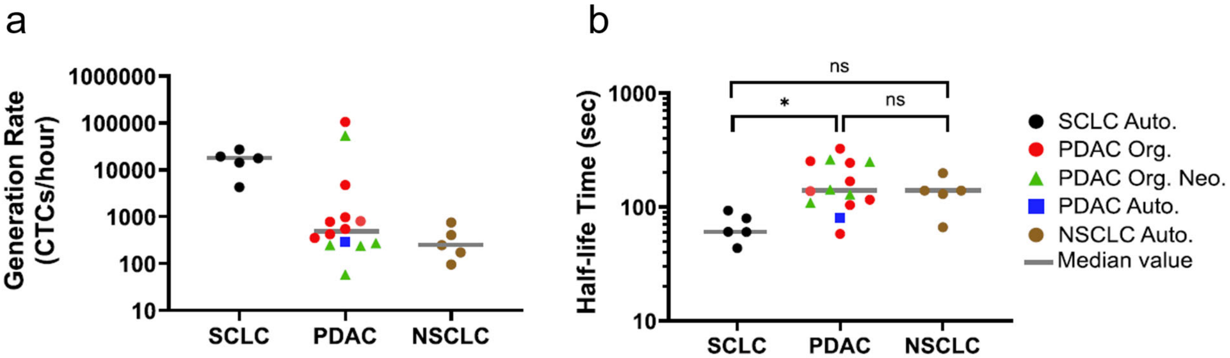

Figure 3.2 Circulation kinetics of solid tumor CTCs calculated from blood exchange experiments. Blood exchange was performed on mouse pairs to estimate generation rates and the half-life times of three different models: small-cell lung cancer (SCLC), pancreatic ductal adenocarcinoma (PDAC), and non-small cell lung cancer (NSCLC). (*$p < 0.05$ ($p = 0.0136$), Kruskal−Wallis nonparametric test with Dunn's sample pairs analysis). For SCLC, n =5 biologically independent experiments. For PDAC, n = 8, 5, and 1 biologically independent experiments, respectively, for Org, Org. Neo., and Auto. For NSCLC, n = 5 biologically independent experiments. Auto- autochthonous (GEMM). Org- organoid. Neo- neoantigen. ns- not significant.

recipient mice (V), mean and standard deviations of steady state transfer rates (r_1 and r_2) over the last 30, 45, and 60 minutes of blood exchange, as well as the calculated generation rate (r_{gen}) and half-life ($t_{1/2}$) and their corresponding errors due to propagated uncertainty of steady state transfer rates.

3.3 Comparison of CTC and cell line kinetics

Since previous studies primarily utilize *in vitro* cultured cell lines to estimate circulation kinetics of CTCs, we sought to compare the estimations of naturally derived CTCs from our blood exchange technique to that of historically used methods of measuring cell line kinetics. Using an established cell line of the same SCLC tumor model (isolated from a lymph node metastasis), we dosed mice with a 1-time bolus of tumor cells in line with our CTC detection system to monitor the clearance rate in a healthy mouse. 25,000 cells in saline were infused intravenously through the jugular vein catheter, and fluorescent detections were monitored for 3 hours (Figure 3.3). We found that there was an extremely rapid clearance of >98% of the cells in less than a minute, followed by a slower decay rate over the next three hours (Figure 3.3b-c). This was in stark contrast to natural CTCs infused during a blood exchange experiment, where no sudden initial clearance was observed and nearly 10% of infused cells were detected by the end of a three-hour exchange.

	Rgen Range (CTCs/HR)	Half-life Range (seconds)	CTCs shed/gram tumor/day	Percent of primary tumor cells shed/day (avg)
SCLC	4,000-27,000	50-100	700,000	0.07%
PDAC	65-6,000	55-260	40,000	0.004%
NSCLC	100-800	60-260	20,000	0.002%

Table 3-1 Overview of circulation kinetics and fraction of tumor shed per day

To explore whether this phenomenon was due to the infusion liquid, we incubated the cell line in blood prior for 20 minutes prior to injection, to determine whether the rapid initial clearance was due to the lack of exposure to blood, since platelets are known to sometimes coat CTCs in circulation[13,141]. In fact, the cells exposed to blood before injection were cleared even faster than those in saline. We similarly wanted to test whether non-CTC tumor cells, those cells either from a primary or metastatic tumor nodule, behaved more similarly to CTCs or cell line. We dissociated primary and metastatic tumors and similarly injected 25,000 cells into healthy mice. We found that while both groups had a large initial clearance, both groups of dissociated tumors had more cells in circulation for the duration of the 3-hour experiment, with cells from metastatic tumors having the highest circulatory rates. This suggests that metastatic cells, which have undergone the

		TBM ID	Exp. #	Q (mL/min)	V (mL)	r_1 (cells/min)	r_1 SD	r_2 (cells/min)	r_2 SD	r_{gen} (CTCs/hour)	r_{gen} Err	$t_{1/2}$ (sec)	$t_{1/2}$ Err
SCLC	Autochthonous	SR7401	1	0.06	1.57	5.90	0.82	0.49	0.03	4282.02	1232.03	97.28	15.85
		SR7464	2	0.06	1.51	17.10	0.61	1.22	0.10	14352.69	1599.76	80.08	7.92
		SR7402	3	0.06	1.59	11.85	0.51	0.48	0.09	17624.38	3531.58	46.10	8.88
		SR6458	4	0.06	1.52	17.67	0.20	0.97	0.13	19253.09	2638.61	61.24	8.73
		SR7391	5	0.06	1.46	25.20	0.40	1.39	0.09	27380.58	1950.07	59.07	4.10
PDAC	Autochthonous	PC1630	1	0.06	1.11	0.46	0.05	0.04	0.00	287.75	64.13	80.87	14.49
	Organoid Neo	WFP8367	1	0.06	1.68	0.11	0.01	0.01	0.00	58.15	18.75	141.81	45.53
		WFP8387	2	0.06	1.46	0.45	0.03	0.05	0.01	237.30	70.26	128.41	38.32
		WFP8296	3	0.06	1.62	0.81	0.04	0.15	0.01	247.32	30.34	261.05	24.99
		WFP8297	4	0.06	1.65	78.49	6.55	6.82	0.25	53790.33	9264.76	108.81	10.16
		WFP8296	5	0.06	1.58	0.87	0.04	0.16	0.02	272.55	51.42	249.45	47.65
	Organoid	KM0275	1	0.06	1.75	1.04	0.04	0.08	0.02	783.59	181.48	104.19	24.97
		KM0275	2	0.06	1.59	0.68	0.03	0.06	0.01	421.89	71.41	115.71	18.65
		KM0285	3	0.06	1.78	1.36	0.42	0.14	0.02	804.21	515.79	137.86	47.16
		KM0292	4	0.06	1.80	17.09	0.92	3.53	0.22	4754.00	623.25	325.01	31.34
		GC538	5	0.06	1.62	0.79	0.33	0.15	0.08	250.32	258.75	253.07	202.60
		KM966	6	0.06	1.27	1.50	0.24	0.24	0.06	547.95	229.66	168.03	62.38
		GC532	7	0.06	1.36	1.26	0.16	0.26	0.01	351.97	94.08	244.00	45.37
		GC534	8	0.06	1.60	87.78	16.27	4.36	0.29	105701.94	39901.63	58.11	11.49
NSCLC	Autochthonous	MB11085	1	0.06	1.80	0.28	0.02	0.03	0.01	174.23	63.18	130.31	48.79
		MB11126	2	0.06	1.20	0.93	0.07	0.07	0.02	755.61	267.80	66.37	23.46
		MB11124	3	0.06	1.29	0.30	0.09	0.05	0.01	95.40	66.12	198.12	94.52
		MB11085	4	0.06	1.68	0.73	0.04	0.08	0.01	405.96	62.28	139.58	17.26
		MB10985	5	0.06	1.42	0.85	0.35	0.17	0.00	247.96	211.31	241.73	123.40

Table 3-2 Raw data from blood exchange experiments summarizing the extracted and calculated parameters from each experiment. Q- flow rate between mice, V- estimated blood volume of recipient mouse, r_1/r_2- average steady state transfer rates of last 30, 45, and 60 minutes of blood exchange, SD- standard deviation of transfer rates, r_{gen}- generation rate of CTCs, $t_{1/2}$- half-life time, Err- propagated error due to uncertainty of steady state transfer rates.

mobilizing epithelial-to-mesenchymal transition (EMT) have properties that increase their ability to circulate, making them behave in circulation more like CTCs than the primary tumor cells.

We next aimed to design a similar experiment that more closely replicated the speed of injection that is seen in the blood exchange experiments. Though similar numbers of CTCs (around 25,000) can be infused during the course of a blood exchange experiment, that infusion is the accumulation of a lower concentration of cells over the full 3-hour exchange. To determine whether a prolonged injection of low numbers of cells would impact the clearance rates, we designed a slow-injection experiment. In this setup, a second peristaltic pump was added to inject cells slowly at 1uL/min through a T-junction into the venous catheter of the mice (Figure 3.4b). Cells were kept in separate tubes at 37C, and tubes were swapped out every 15 minutes, to ensure that the viability of infused cells was consistent throughout the experiment. For the duration of the 3-hour experiment, the connected CTC counter was used to monitor the fluorescent cells in the blood (Figure 3.4b).

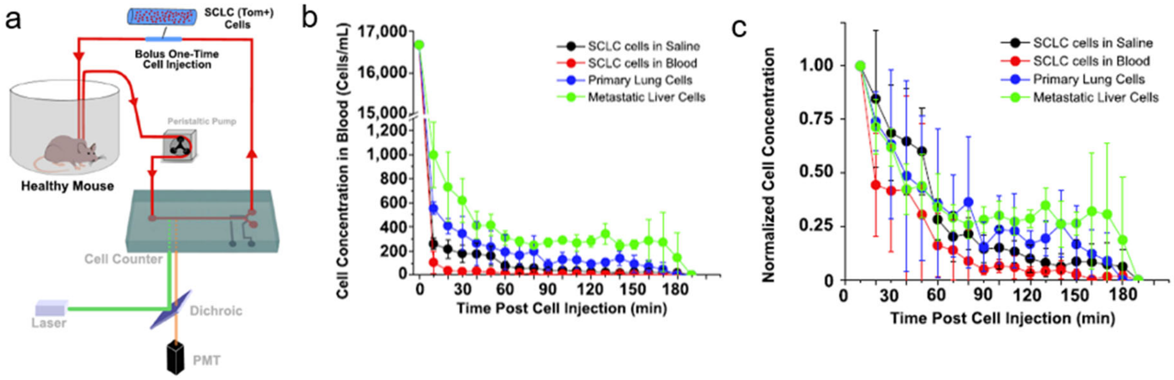

Figure 3.3 Decay profile of bolus injection of SCLC cell line. (a) Schematic showing the intravenous infusion of TdTomato+ cells and subsequent monitoring of fluorescent cells via CTC counter. (b) Real-time measurements show an extremely rapid clearance of >90% of cells within the first minute, followed by a slower decay profile. This rapid initial clearance with slower remaining decay was seen regardless of whether cells were incubated in blood or saline, or whether the cells infused were from a cell line, or dissociated primary or metastatic cells. (c) Normalized cell concentration to the first 10 minutes show that the injected cells that survived the first 10 minutes can remain in circulation for several hours

Using the slow injection method, we were able to more closely compare the finding of our blood exchange method with the injection of naturally shed CTCs with an SCLC cell line infused at a very similar rate. We found that even when injected slowly over many hours, the cell line did not stay in circulation for as long at CTCs, and was more rapidly cleared, with approximately 6-fold fewer cells being detected over the course of the scan compared with a blood exchange experiment (Figure 3.4c). This data further suggests that the SCLC cell line differs from naturally shed CTCs in their circulatory kinetics, indicating that the current standard method of calculating kinetics, through the monitoring of decay of injected cell lines, does not fully capture the nature of CTC dynamics, and may lead to incorrect assumptions about the trafficking of CTCs.

Our next goal was to characterize the differences between the cell line and endogenous CTCs in the SCLC model in order to better understand why they have differences in their circulatory properties. We first looked at whether there were differences in biophysical properties, since larger, more massive cells could get trapped in capillaries more easily and gravitate toward the walls of channels in small fluidic systems due to inertial focusing[112]. Our lab has developed a

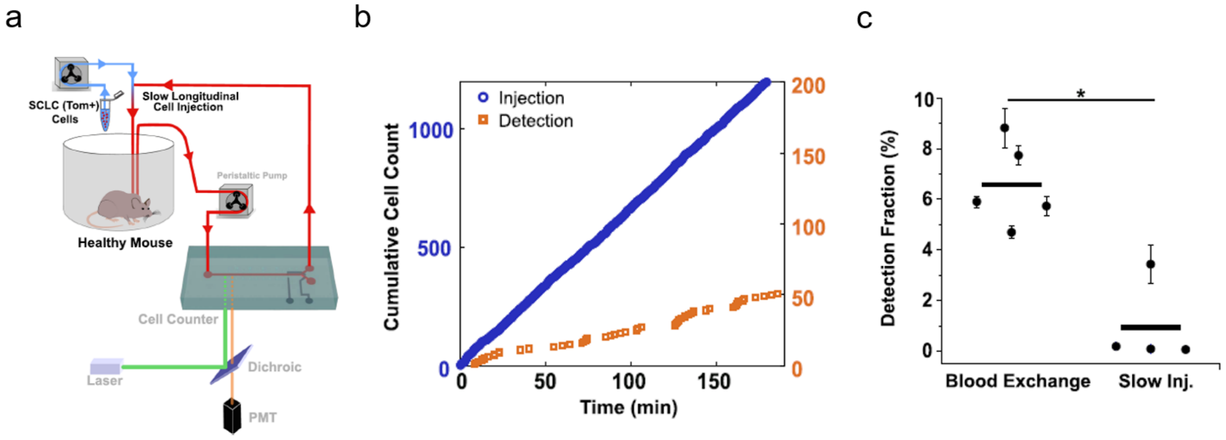

Figure 3.4 Slow injection of cell line. (a) Schematic showing the setup of slow injection experiment. Cells are slowly pumped through a peristaltic pump and infused through a T-junction into the venous catheter while monitoring blood concentration through the CTC detection system. (b) Cumulative detections of the injected fluorescent cell line shows less than 5% detection of cells during the 3 hour experiment. (c) Comparison of detection fraction of naturally derived CTCs from blood exchange to slow injection experiment shows that a higher percentage of CTCs are capable of surviving in circulation compared to a similar concentration of slowly injected *in vitro* cultured cells. (p=0.016 with two-tailed t-test)

system known as the suspended microchannel resonator (SMR) which is capable of very accurately measuring the buoyant mass of single cells[142–144]. The device consists of a microfluidic chip with a cantilever. The cantilever is vibrated at its resonant frequency, and a piezoelectric detector monitors the frequency of vibration. Within the cantilever is a fluid filled channel that flows to the tip and back out the base of the cantilever. As single cells flow through, their added mass changes the mass of the cantilever, causing it to resonate at a lower frequency proportional to the added mass. Therefore, by measuring the change in resonant frequency as cells pass through the channel, their buoyant mass can be determined a with fraction of a pg accuracy.

We added a feature to the SMR system that incorporates fluorescent detection (Figure 3.5a). By shining a laser on the bypass channel of the SMR, we could identify cells that were fluorescent, to ensure that the measured cells were indeed our fluorescent tumor cells. We ran both the fluorescent SCLC cell line and CTCs sorted and purified from SCLC tumor bearing mice in order to determine whether there were changes in the biophysical properties of the two that would

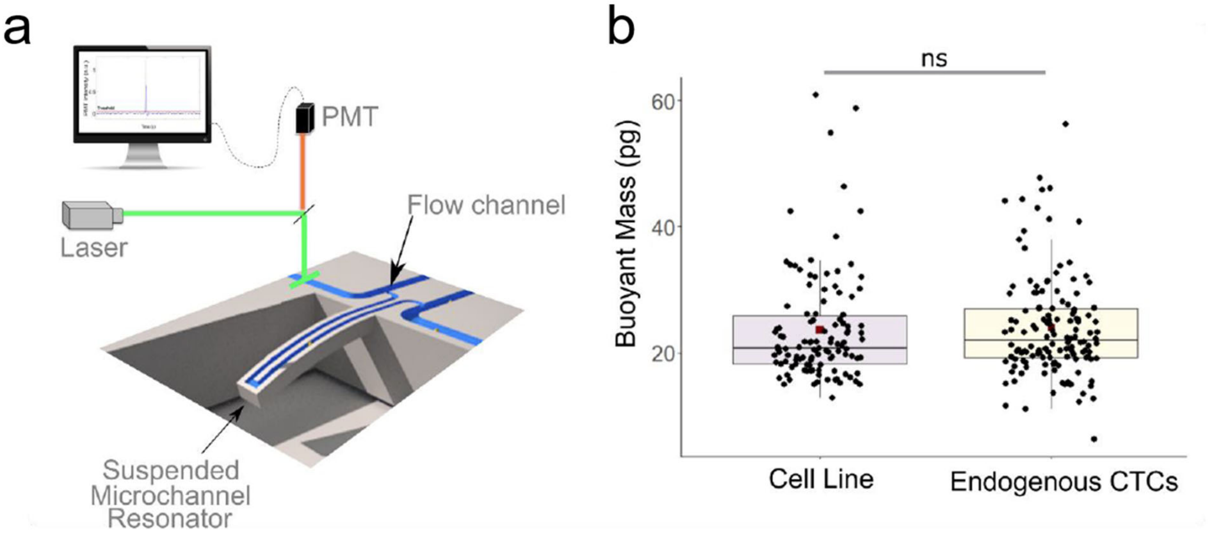

Figure 3.5 Measuring buoyant mass of CTC. (a) Design of the fluorescent suspended microchannel resonator (fSMR) for mass measurement of fluorescent cells. (b) SCLC cell line and naturally shed CTCs shows no difference in buoyant mass ($p = 0.3$, two-sided Mann-Whitney-Wilcoxon non-parametric test)

explain their different kinetics. We found that both samples had equivalent buoyant masses (Figure 3.5b). Previously, our lab has found that buoyant mass is correlated with passage time through a narrow constriction and cell volume[145], suggesting that biophysical properties of the cells are insufficient to explain their differences in circulation behavior.

This led us to explore whether there were any transcriptomic differences between the cell line and the endogenous CTCs. We collected SCLC CTCs naturally shed from tumor-bearing mice, as well as the fluorescent SCLC *in vitro* cell line, and we sorted out cells from the fluorescent SCLC cell line that had been injected into healthy mice, to directly compare the CTCs transcriptionally to the cell line and those cell line cells that survive past the initial rapid clearance following injection (Figure 3.6a). We used Smart-Seq 2 to perform single cell RNA sequencing on the three populations. After cells were lysed, reverse transcription was performed, followed by PCR amplification. After quality control, tagmentation was performed using a Nextera XT kit with unique 8 bp barcodes for single-cell identification. cDNA libraries were then pooled and sequenced on Illumina NextSeq500 with an average depth of 1.2×10^6 reads/cell. The subsequent FASTQs were mapped to mm10 mouse transcriptome with Bowtie 2, and gene expression levels were log-transformed. Cells were excluded with fewer than 500 detected genes or fewer than 375,000 total reads.

We performed t-distributed Stochastic Neighbor Embedding (tSNE) dimensionality reduction on the samples, and found that while each population grouped separately, the sorted cell line and true CTCs clustered together transcriptionally (Figure 3.6b). The top genes defining each cluster were plotted on a heatmap, demonstrating that the CTCs were more similar transcriptionally to the injected and sorted cell line cells than the "initial" noninjected cells (Figure 3.6c). The genes defining the "initial" population were predominately related to cell division, while those upregulated in the CTCs and sorted cell line were related to stress, inflammation, and cell signaling.

Next, to analyze the differences between gene expression of CTCs and the sorted cell line, we performed principal component analysis (PCA). PCA revealed that the first two components

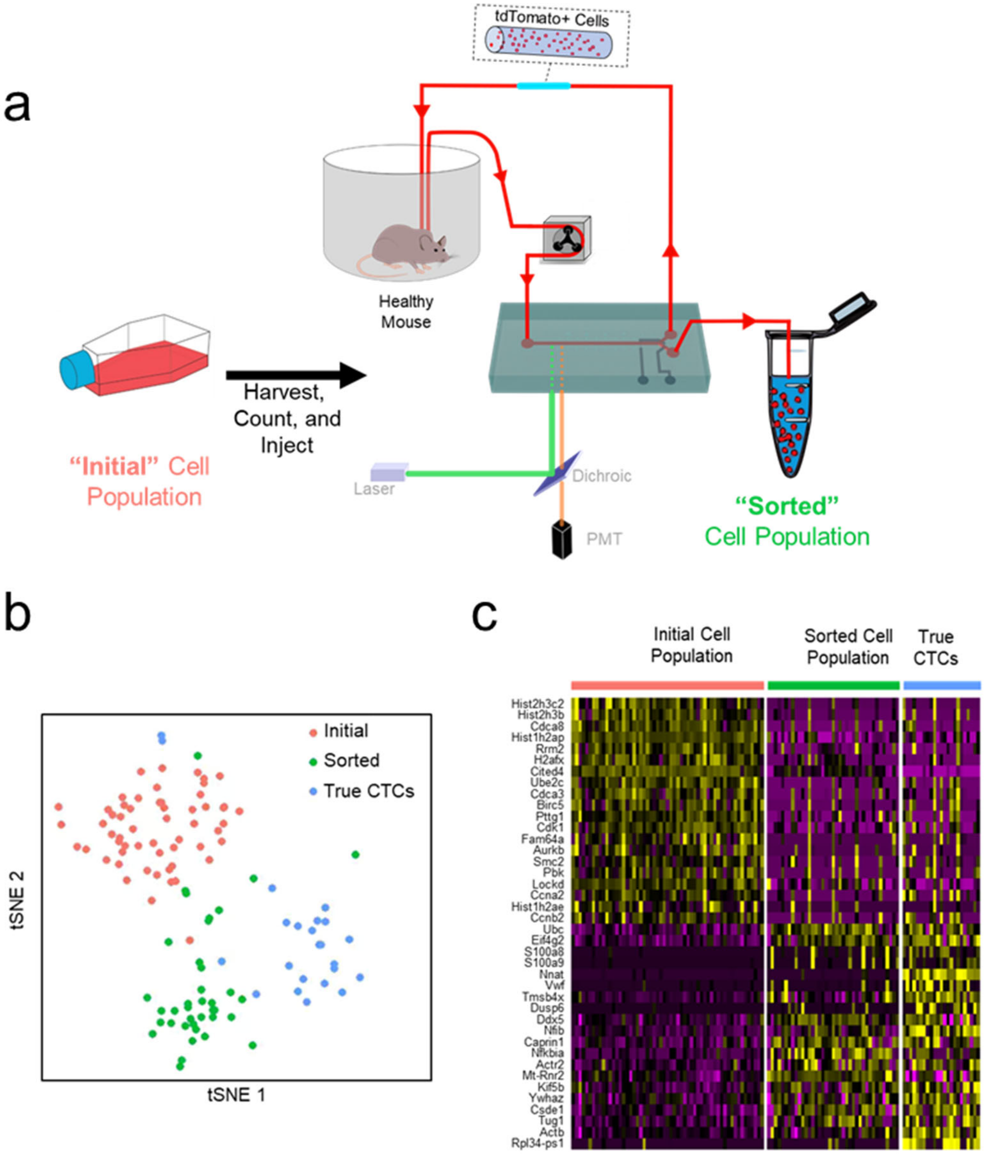

Figure 3.6 RNA-seq of SCLC CTCs vs cell line. (a) Overview of cell line collection. "Initial" cells were harvested directly from culture, while "sorted" cells were injected into healthy mice and sorted from the blood. (b) The three populations group separately on t-distributed Stochastic Neighbor Embedding (tSNE) plot, though "sorted" and "true CTCs" were defined by the same cluster. (c) The top genes defining the two clusters ("initial" and "sorted" + "true") demonstrate that the cell line surviving in circulation is more similar to CTCs than the initial population.

(PC1 and PC2) nicely separated out the two populations (Figure 3.7a). PC1 high cells were associated strongly with CTCs, while PC2 high cells classified cells from the cell line. To better understand the genes that associated with the PCs, we identified Gene Ontology (GO) genesets that may be expected to associate with metastasis or survival in the bloodstream. We used the AddModuleScore function in Seurat 2.0 to give each cell a score based on how highly that cell expressed the genes found within each GO set. Next, we performed correlation analysis between the module score and the principal components to identify whether the genes that define each principal component associate with the GO module scores for each cell. We found a number of genesets that were significantly correlated with each of the PCs, indicating genetic pathways associated with the CTCs and the cell line (Figure 3.7b).

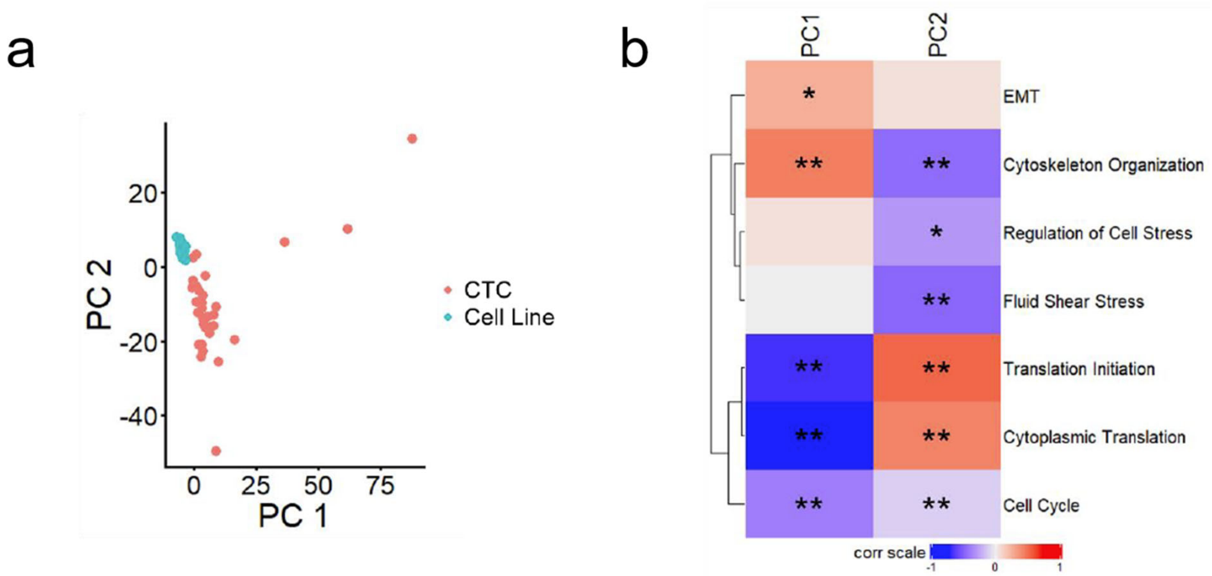

Figure 3.7 Single cell RNA-sequencing of SCLC CTCs and sorted cell line. (a) Principal component analysis reveals a striking separation of CTC and cell line, with PC1 being upregulated in the CTCs and PC2 begin upregulated in the cell line. (b) Heatmap showing the correlation coefficients between principal components and the expression of select Gene Ontology genesets show differences in gene expression profiles associated with each principal component. Color represents Pearson coefficient, R. * p<.01; ** p<.0001

We found that PC1, which is associated with the endogenous CTCs, had an increase in the expression of genes related to epithelial to mesenchymal transition (EMT), a key process in the development of cells capable of intravasating into the bloodstream. Additionally, cytoskeletal organization genes were positively associated with CTCs in PC1, which could explain difference in the circulation capacity of CTCs. Cells modulate their cytoskeleton to change their cell stiffness and flexibility, which could allow cells to squeeze through capillaries in a way that would alter their circulation kinetics. We also found that the CTCs were negatively correlated with a number of genesets associated with cellular proliferation, including translation and cell cycle genes.

The sorted cell line, on the other hand, showed many opposite associations in terms of gene expression. PC2 was negatively associated with cytoskeletal organization, and several genesets associated with cell stress. And while they also showed a decrease in cell cycle genes, they did not see the same decrease in translation related genesets, suggesting that the cell line continues at least some of its normal cellular processes in the blood. Further studies will be needed to explore how these transcriptional differences translate into measurable differences in circulation kinetics.

3.4 Blood exchange to seed metastases in naïve mice

Using the fluorescent GEMM model of SCLC, we performed blood exchanges, whereby the circulation of a tumor-bearing mouse (TBM) was sequentially connected via the CTC-Counter to two naïve healthy mice (HM) of the same background (Figure 3.8a). Each HM was connected to the TBM (late stage with primary lung and metastatic liver tumors) for 2 hours, and

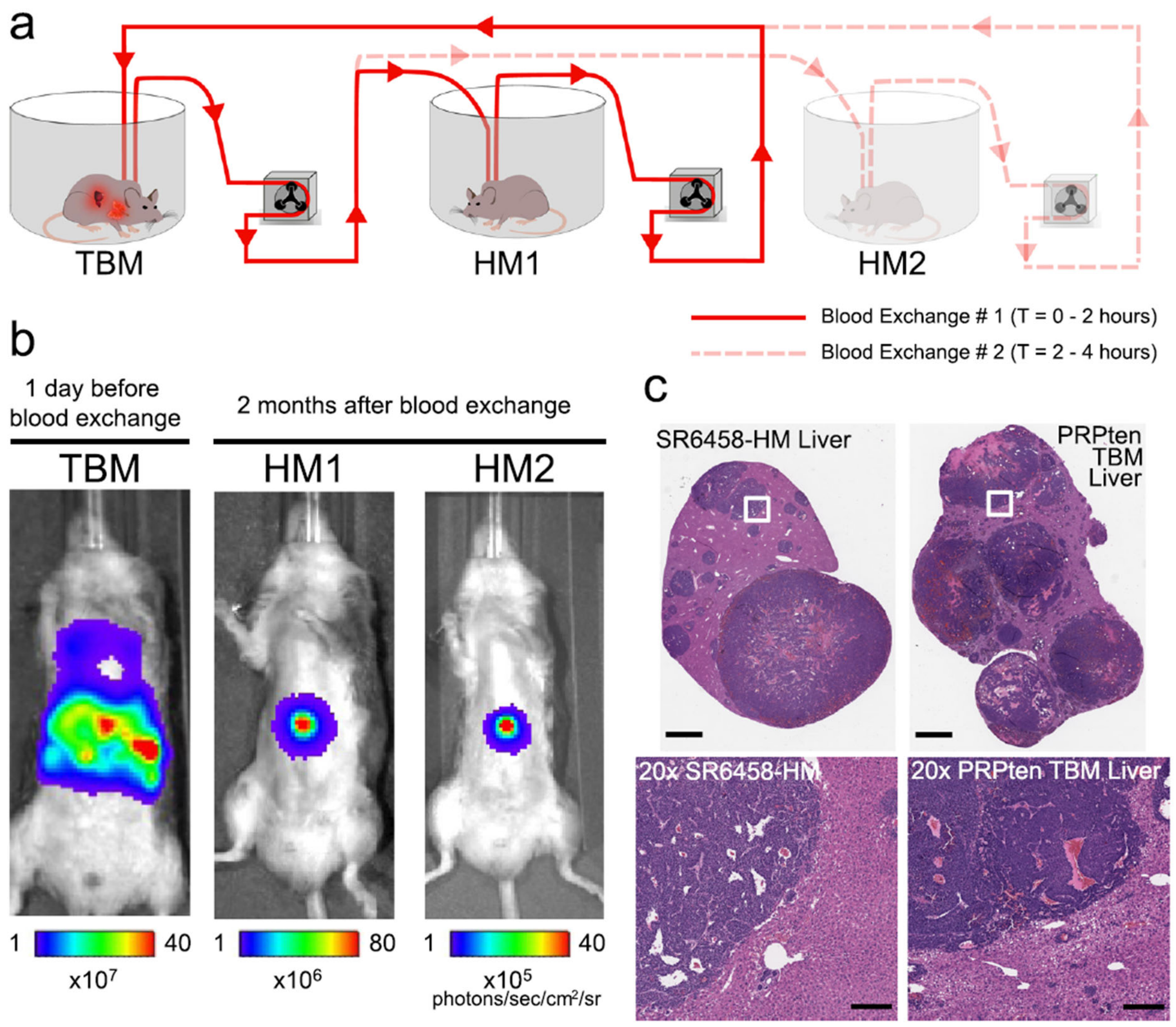

Figure 3.8 Blood exchange generates metastases in naïve mice[136]: (A) Schematic of blood exchange. The circulation of a tumor bearing mouse (TBM) is connected to healthy naïve mice (HM) through the CTC detection system. CTCs are enumerated and injected into the naïve mouse. (B) Intravital imaging (IVIS) showing generation of tumors in the liver of naïve mice 2 months post blood exchange. (C) scRNA-seq dimensional reduction plot showing clustering of transcripts of tumors from the TBM and HMs by mouse.

approximately 8000 CTCs were transferred from the TBM into each HM. In this way, metastasis generation in multiple separate HMs could be studied from CTCs of the same TBM (Figure 3.8B). The primary lung tumor and liver metastasis were harvested from the TBM on the day of blood exchange.

Approximately 2 months after blood exchange, IVIS imaging showed bioluminescent nodules in the livers of both HMs (Figure 3.8b). These tumors were harvested, and histological analysis confirmed that these tumors had similar morphology to the metastases of the donor animal (Figure 3.8c). This data suggests that even low number of CTCs (a few thousand) are capable of seeding a macroscopic metastasis. And the fact that tumors grew in the healthy recipient mice shows that the cells we measured in our blood exchange experiments are indeed fully functional CTCs. Additional replicates of the metastatic seeding of SCLC tumors through blood exchange are shown in Figure 3.9a. We also found that recipient mice who had developed large liver metastases shed CTCs back into the blood, indicating that the disease seeded through blood exchange could recapitulate many aspects of the disease progression (Figure 3.9b).

When infused into the jugular vein, CTCs first encounter the capillary bed of the lungs. However, none of the HM recipient mice developed lung disease. This is contradictory to the hypothesis that CTCs form metastases in the first capillary bed that they encounter, and suggests that they instead seed in the organ with the most favorable conditions to their specific growth. This is further supported by the fact that the location of tumor development in all of the healthy recipient mice was the liver, which is the same place that metastatic tumors developed in the donor mice, suggesting that the SCLC CTCs prefer to grow metastases in the liver, regardless of whether the animal has disease and where those CTCs are introduced into circulation.

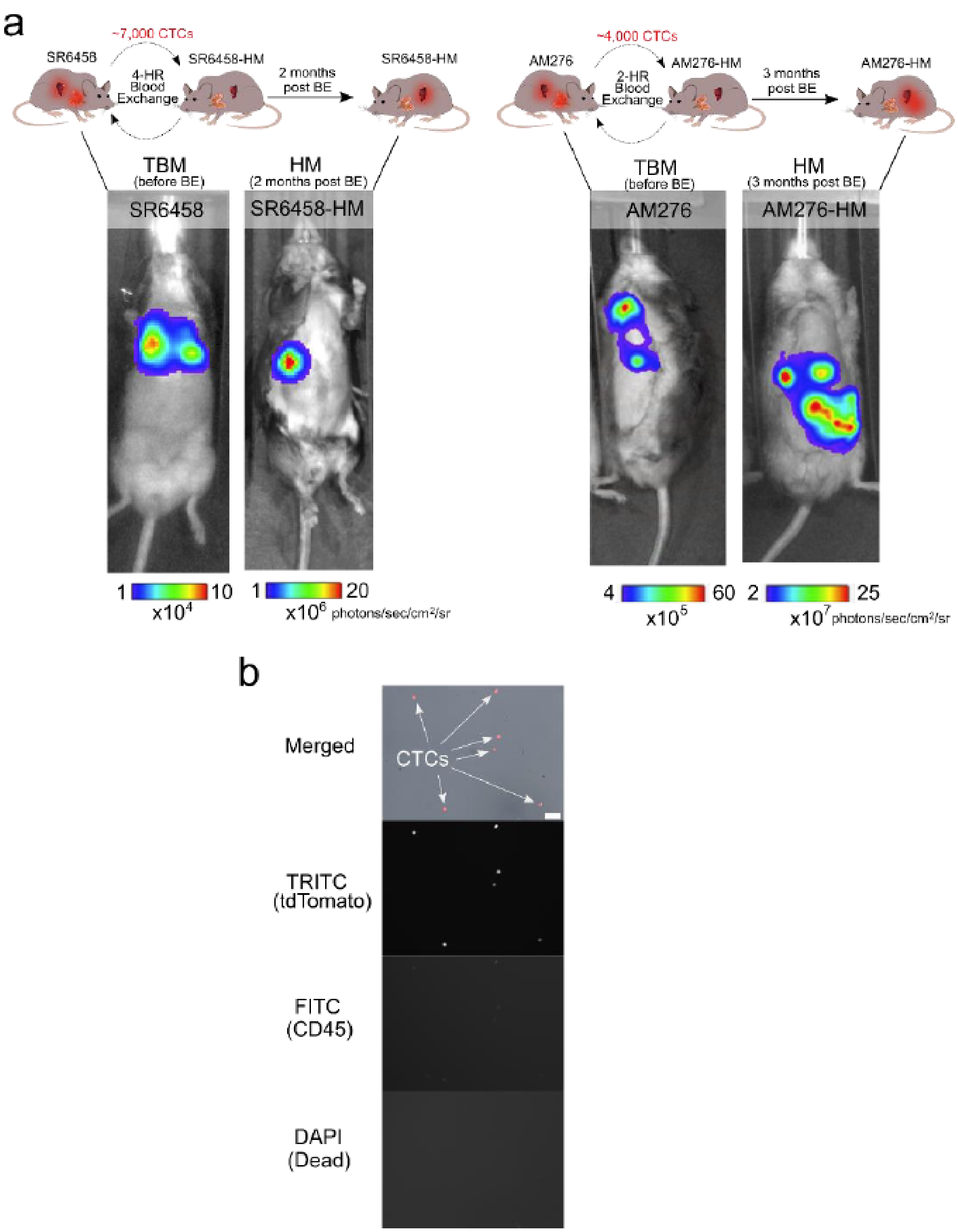

Figure 3.9 Metastatic tumors induced through blood exchange[136]. (a) Additional examples of IVIS imaging demonstrating the utility of blood exchange as a method to generate metastatic lesions in a naïve recipient from as few as 4000 CTCs. (b) Microscopy of purified CTCs isolated from HM recipient mice which developed SCLC metastases. Tumor cells are identified by the tdTomato that is constitutively expressed in the tumor model, and because they lack the white blood cell marker CD45 as well as the dead-cell marker DAPI (scale bar = 20um). These findings were replicated in four separate biological replicates.

Aside from histological analysis, we used sequencing to analyze how the transcriptional signature of the tumor evolves through the various compartments. From the donor animal, three tissues were collected for analysis: the primary lung tumor, the metastatic liver nodules, and CTCs from the blood. From the two recipient animals, the metastatic liver nodules were processed. The transcriptome of each tumor compartment (primary, metastasis, CTCs) was analyzed using Smart-Seq2 (Figure 3.10). The data show clustering of tumor compartments by mouse, whereby the three compartments from the TBM (primary lung, CTC, and liver metastasis) separated from the livers of the two recipient HMs (Figure 3.10a). Next, differential expression analysis was performed to determine which genes drove the changes in gene signature. Clustering the cells by animal and performing differential expression analysis revealed the top 10 genes from each group that defined the signature from that cluster (Figure 3.10b). Further studies will be needed to understand how the transcriptional changes influences the different tumors. Additionally, we compared the signatures of the primary lung tumor to each of the metastatic nodules (TBM liver, HM1 liver, and HM2 liver). Differential expression analysis between the primary lung tumor and each liver metastasis revealed a total of 215 genes that significantly differed (log-fold change >0.6, adjusted p-value <0.01) between the primary tumor and the metastatic tumors (Figure 3.10c). Of these, greater than 20% were found in at least two of the tumors, and over 5% were shared between all three metastatic tumors. Further analysis will be required to determine if this variance is due to differences in tumor size (the TBM had very severe disease, whereas the HMs had much smaller, localized tumors) or inter-mouse heterogeneity. Nevertheless, this experiment shows the potential of the blood-exchange platform as a way of developing metastatic models of cancer directly from CTCs without any *ex vivo* processing. This technique could be especially useful for studying metastasis in mouse models with highly aggressive primary tumors, where there is not enough time for metastases to sufficiently grow before the mice succumb to disease. This platform would allow for the generation of metastatic only models, allowing for the study of metastatic outgrowth without the constraint of an aggressive primary tumor.

In this chapter, we applied the blood exchange method to mouse models of SCLC, NSCLC, and PDAC. By measuring the steady-state transfer rates between tumor bearing and healthy mice, we extracted the half-life times and generation rates for these models. We found that generation rates in these models varied drastically over several orders of magnitude, while the half-life times varied by only 2- to 3-fold, even in models with different metastatic burdens. We additionally demonstrated that *in vitro* cultured cell lines behaved dramatically different than naturally shed CTCs, with a much faster initial clearance rate, even when added slowly to the blood. We used RNA sequencing to show that cell line cells that stayed in circulation had more similar transcriptional signatures to CTCs than to the *in vitro* cultured cells, but still had striking differences from the CTCs. Finally, we showed the utility of the blood-exchange system to generate metastatic models of cancer in healthy mice by infusing only a few thousand CTCs, opening the door for studying metastatic disease in mouse models that traditionally only have primary tumors.

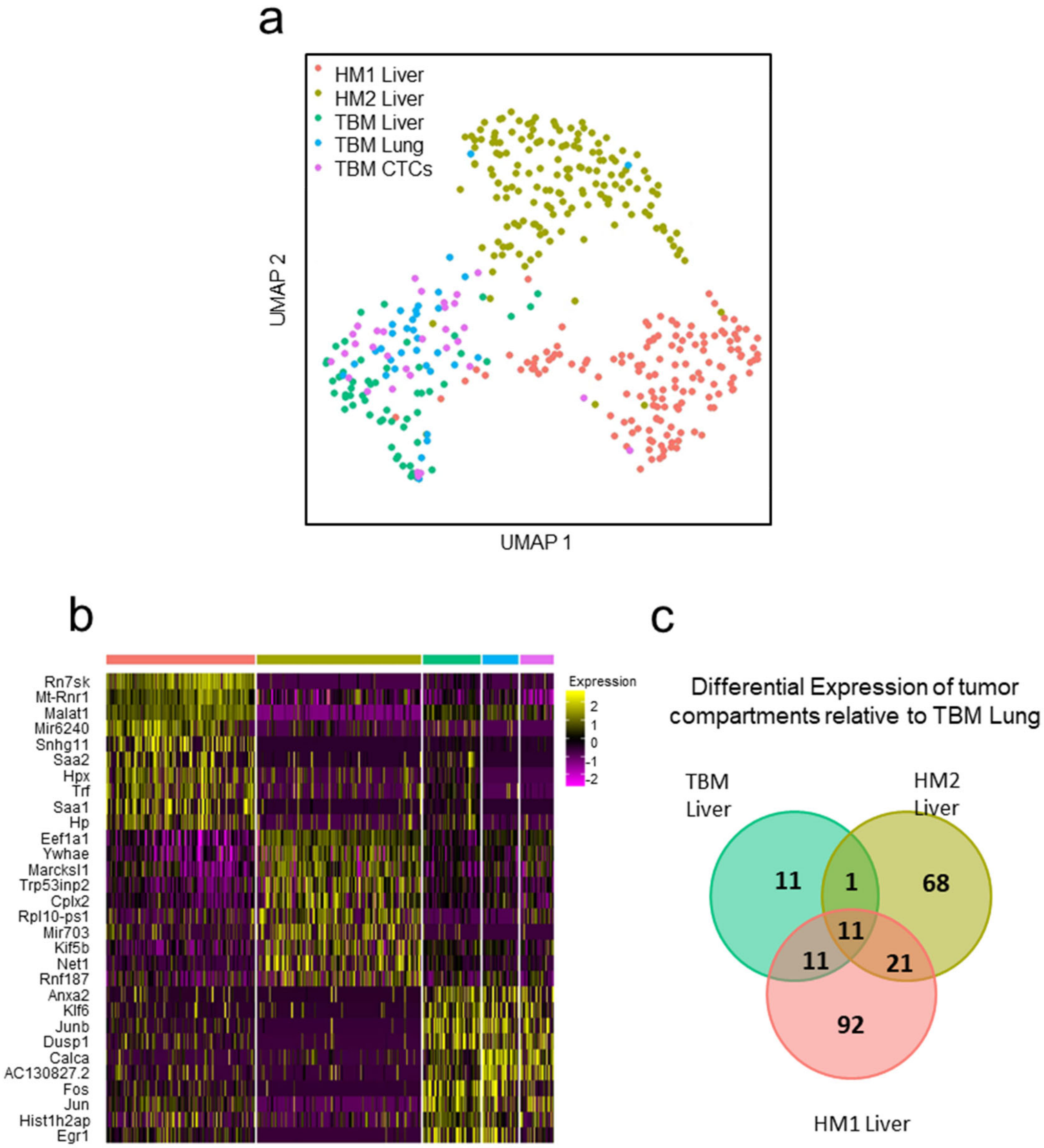

Figure 3.10 Single cell RNA Sequencing (sc-RNA seq) of SCLC tumor compartments from blood-exchanged animals. (a) UMAP plot showing differences in transcriptional signature of cells from five tumor compartments: the primary lung tumor, metastatic liver, and CTCs from the donor tumor-bearing mouse (TBM lung, TBM liver, and TBM CTCs, respectively) and metastatic liver lesions from the two healthy recipients (HM1 liver and HM2 liver). Transcriptional signatures reveal clustering by animal. (b) Differential expression analysis shows the top 10 genes from each cluster that are differentially expressed between the three mice. (c) Venn diagram shows overlap in genes that are significantly differentially expressed (log-fold change >0.6, adjusted p-value <0.01) in the three liver metastases relative to the primary lung tumor of the donor mouse. More than 20% of genes are in common between at least two of the tumors, and more than 5% are shared between all three metastatic tumors.

4. Blood Exchange for Liquid Tumor CLCs

4.1 Background

Leukemias are a diverse set of hematological diseases characterized by heavy involvement of tumors in the blood[4]. As discussed in section 1.2, They can be classified broadly either through lineage status of myeloid or lymphocytic, as well as by differentiation status, with more well differentiated diseases being considered as chronic, and the more blast-like diseases being considered acute. Acute myeloid leukemia (AML) and acute lymphocytic leukemia (ALL) are the more aggressive subtypes in adults, with 20% and 40% 5-year survival rates, respectively[3,80].

Leukemias are commonly thought of as a systemic disease characterized by transport through the blood. They commonly arise from a mutation in a cell in the marrow of one bone, but quickly spread to bones throughout the body and have heavy involvement of not just hematological organs such as lymph nodes and spleen, but also liver and even brain[58,59]. Because of this, a thorough study of the circulation kinetics and the factors that affect circulation in leukemia is crucial to understanding the disease. Additionally, exploring the variation in circulation kinetics between solid tumor CTCs and liquid tumor CLCs will allow for the understanding of how the fundamental differences between liquid and solid tumors translates to trafficking properties in the blood.

While much is known regarding the mutational genetic landscape that can lead to the development of leukemias, little is known regarding the circulation profile of leukemia or the factors that regulate circulation. Recent studies have suggested that a particular vascular adhesion protein, E-selectin, plays an important role for AML[4,104]. The increased expression of E-selectin provides a chemoprotective effect for leukemia cells, and the inhibition of E-selectin allows the bone marrow to release AML cells, leading to an increase in the circulating concentration of AML[100]. While this finding suggests that vascular adhesion molecules may play a key role in modulating the levels of leukemia in tumor compartments (blood, bone marrow, etc), a thorough study of how these proteins can alter circulation kinetics of CTCs has not been done.

Because there is limited knowledge of the kinetics of circulation of leukemia cells in the blood, it is unknown what factors regulate the clearance dynamics of circulating leukemia cells (CLCs). There are two broad categories that could influence the circulation kinetics of CLCs: non-circulating factors and circulating factors (Figure 4.1). The non-circulating category would include both vascular and extravascular features. This could include changes to the endothelial layer of blood vessels, such as increased permeability or changes in adhesion proteins, or tissue specific features of the bone marrow and spleen, such as hypercellularity associated with late-stage disease or changes in extracellular matrix (ECM) deposition.

Alternatively, circulating factors could govern the circulating kinetics of CLCs. While non-tumor components of the blood, such as platelet aggregation or protein changes in the plasma, could theoretically impact the circulatory properties, such changes would be unlikely to directly impact circulating kinetics, and more likely to cause secondary changes to the vascular or extravascular compartments, rather than directly acting on the CLCs. The most likely factors within the blood would be properties of the tumor cells themselves. These properties could include physical properties, such as volume, mass, or stiffness, or could be due to surface proteins that interact with the vascular and extravascular spaces.

The blood exchange platform provides a unique opportunity to probe how circulating and non-circulating factors influence the behavior of CLCs in the blood. Because our system has donor animals with fluorescent CLCs and non-fluorescent recipient animals, we can alter them independently to decouple the influences of circulating and non-circulating factors. To study circulating factors, we can vary the condition of the donor animal in order to query how changes in the tumor cells themselves associated with disease burden and treatment status impact the circulation kinetics. Likewise, by modulating the disease and treatment state of the recipient animal, we can explore whether non-circulating factors can alter the clearance rates of CLCs.

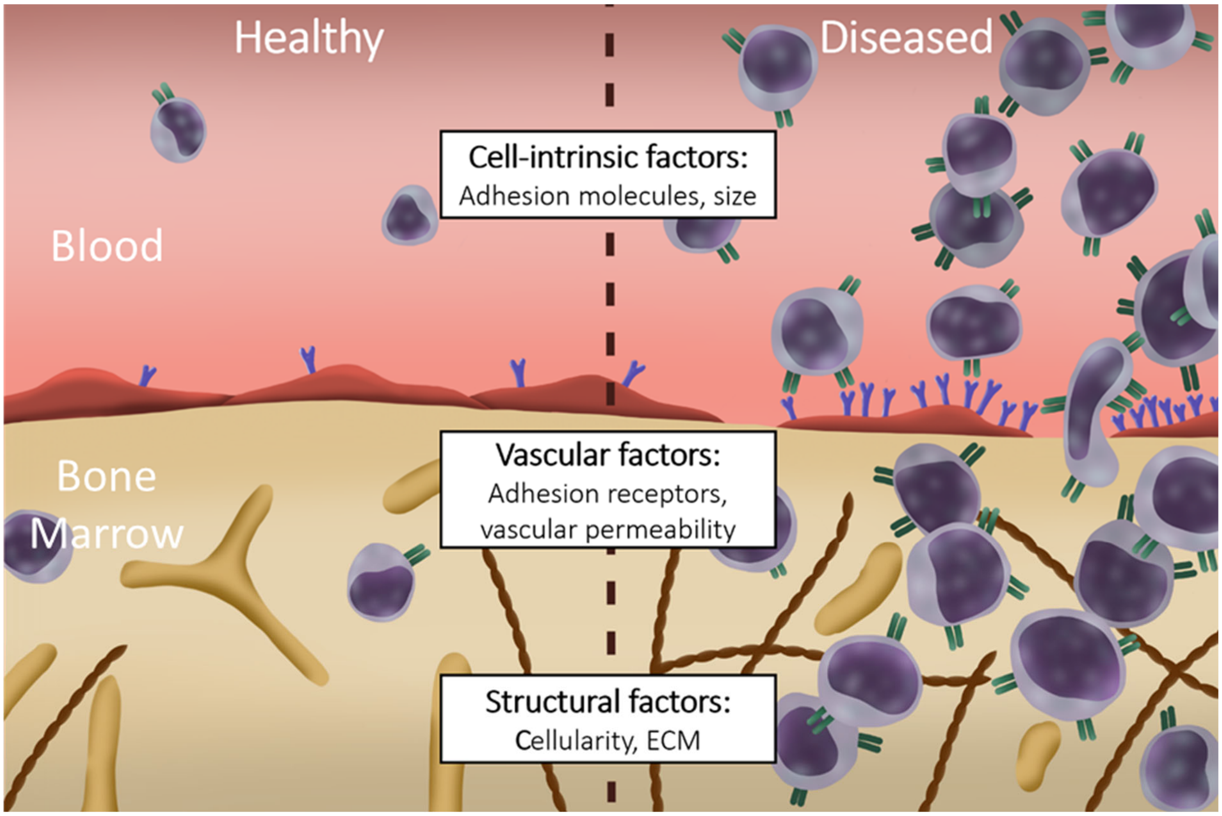

Figure 4.1 Overview of vascular and extravascular changes that occur over the course of disease in leukemia. Circulation kinetics of CLCs could be governed by circulating, cell-intrinsic factors, such including biophysical or immunological properties. Alternatively, non-circulating factors, including changes to the vasculature or extravascular space, could influence the clearance rates of CLCs in the blood.

In this chapter, we demonstrate that the blood exchange system can be used to extract circulation kinetics in both an ALL and AML model. We then vary the donor-recipient pairs to identify factors that govern the circulation and find that increased expression of vascular adhesion factors in a diseased state of ALL causes a decrease in clearance of cells from the blood. Finally, we show that increased levels of adhesion markers associated with relapse AML disease, but not relapse ALL, allow for faster equilibration of circulating leukemia cells.

4.2 Leukemia models

While the blood exchange technique was originally designed to detect and transfer rare circulating tumor cells within the blood of mice bearing solid tumors, it also shows promise for studying models of liquid tumors. And for liquid tumors in particular, which are often thought of as systemic diseases with very high levels of CLCs in the blood, the blood exchange method allows for novel ways of understanding how various factors contribute to the circulation kinetics.

Two different leukemia models were utilized to study circulation kinetics of liquid tumors. The first was an B cell ALL model defined by a BCR-ABL translocation into B cell precursors, which is a very common genetic mutation associated with both ALL and CLL leukemias. This translocation, also known as the Philadelphia chromosome, results in a hyperactive tyrosine kinase, which results in the activation of a number of pathways, including cell growth and metabolism[146]. Historically, this was one of the more deadly mutations associated with leukemias, but in the last several decades, effective tyrosine kinase inhibitors, such as imatinib and desatinib, have been introduced, which have drastically increased the survival of patients with this mutation[68]. This syngeneic model was derived from a male C57BL6 mouse. We also have a version of this model that has been transfected with a puromycin-selective plasmid that expresses the red fluorescent protein (RFP), providing us with both a fluorescent and non-fluorescent version of the same ALL model.

The ALL cell line cultures well *in vitro* prior to initiation of tumor in mice in a media consisting of RPMI-1640, 10% fetal bovine serum (FBS), 1% penicillin/streptomycin, and 1% 5mM beta-mercaptoethanol (BME). To initiate disease, 500k cells are injected intravenously via tail vein into 12-week-old, male C57BL6 mice. Detectable levels of circulating leukemia cells (CLCs) in the blood can be found by day 6-8. The model is highly aggressive, with mice succumbing to disease by around 18-24 days post initiation. Severely diseased mice present with hunched posture, weight loss, and loss of movement in posterior limbs.

The second model of leukemia we used to study circulation kinetics is an AML model with an MLL-AF9 translocation and RFP expression. The MLL-AF9 transgene upregulates cellular transcriptional processes and is associated with high rates of relapse in patients[147,148]. The AML model was also derived from a male C56BL6 mouse. However, unlike the ALL model, the AML model does not culture well *in vitro.* While the cells can be maintained for about a week in culture in a rich media of RPMI, 10% FBS, 1% penicillin/streptomycin, 10µg/mL IL (interleukin)-3, 10µg/mL IL-6, and 20µg/mL SCF (stem cell factor), they begin to crash in culture for any longer. Additionally, after having been culture *in vitro*, they quickly lose their ability to effectively engraft into mice. Thus, this line must be expanded *in vivo,* with spleen from severely diseased animals being frozen down at euthanasia. The frozen spleen samples must then be thawed 24 hours prior to initiation in a new cohort of mice. Similar to the ALL model, this model is initiated via a cell line injection of 500k cells intravenously via tail vein injection into male C57BL6 mice. However, for this model, non-lethal irradiation with 1x 5Gy, to clear out space in the bone marrow, is necessary 24 hours prior to tail vein injection in order for tumors to seed effectively in the bone marrow. This is another highly aggressive model, with mice succumbing to their disease within approximately 17-22 days after tumor initiation. Though severely diseased animals may show weight loss and some hunched posture, some mice in this model do not show these features even at late-stage disease. However, they typically present with pale or cold toes 1-2 days before succumbing to disease.

Both of these models have tumor burden that starts in the bone marrow and has heavy involvement of the blood and spleen. At late-stage disease, the bone marrows of these mice typically have >90% disease burden, and 10-25M cells can be harvested from each cleaned femur through crushing with mortar and pestle. Both of these models also have very high levels of spleen involvement. The spleens of diseased mice expand dramatically and can be 5-10 times larger than that of a healthy mouse. Slicing and mashing a diseased spleen through a 100μm strainer can result with recovery of 200-400M+ tumor cells. Blood burden in these two models varies somewhat, with the ALL model having significantly increased circulating levels relative to the AML model. As seen in Figure 4.2, the concentrations of CLCs in the blood in the two leukemia models increase exponentially, though with different absolute values. Throughout the course of the 3-week disease,

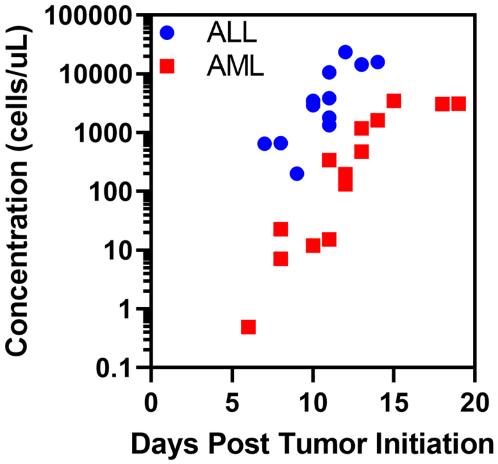

Figure 4.2 Blood burden of leukemia models in mice over the course of disease. Both models increase at a roughly exponential rate, though the ALL model has approximately an order of magnitude higher concentration.

the ALL model has approximately an order of magnitude higher level of blood burden compared to the AML model, though both models have similarly high levels of burden in both the bone marrow and the spleen.

4.3 New blood exchange method for leukemia

There are several key differences between hematological and solid tumors as it pertains to blood exchange. The concentration of CLCs in leukemic mice can be two to five orders of magnitude higher than that of CTCs in solid tumor-bearing mice, which leads to technical difficulties in distinguishing individual cells during blood exchange. In addition, we found that it takes much longer for the CLC concentration in the blood to reach steady state in leukemic models of blood exchange than for solid tumor models (Figure 4.3). Since the method for solid tumors

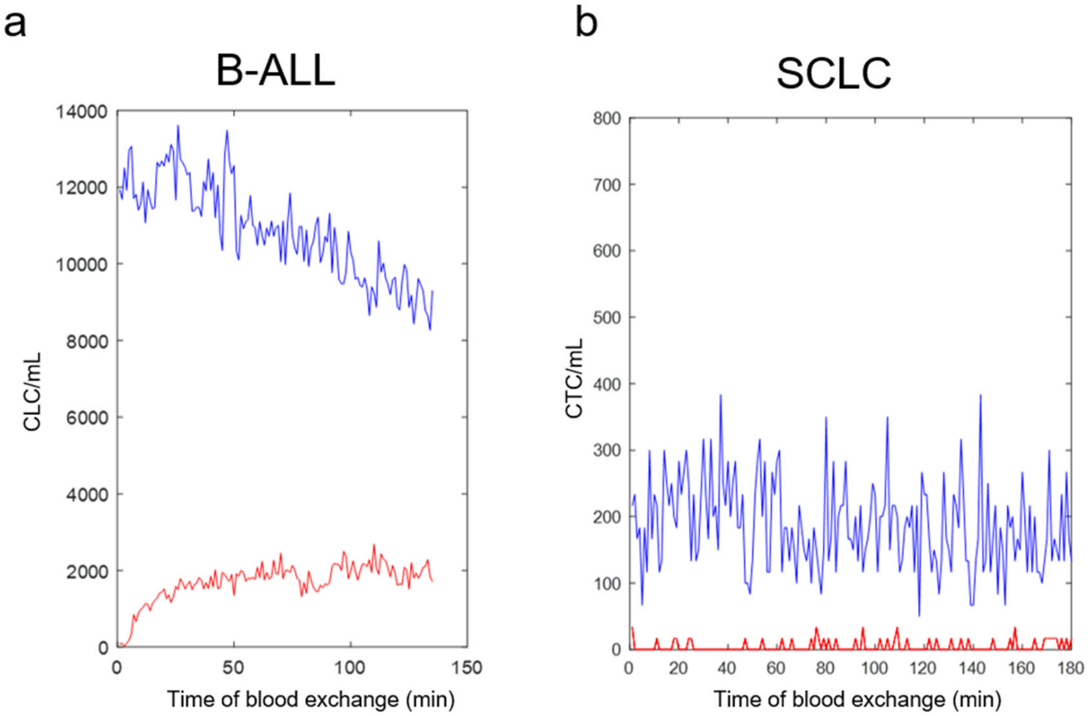

Figure 4.3 Real Time concentrations of circulating tumor cells in donor (blue) and recipient (red) mice. (a) In the B-ALL model, the concentration of CLCs in the blood of the donor mouse does not reach steady state at 2.5 hours. (b) in the SCLC model, both mice quickly reach a steady state concentration, allowing for estimation of circulation kinetics using steady-state exchange rates.

relied on steady-state concentrations, a new method for estimating CLC kinetics was needed. Additionally, the estimation of circulation kinetics using the model from Chapter 2 assumes that the clearance rates in the donor and recipient animals are equivalent. The question arises as to whether this is a fair assumption to make. In the solid tumor models, the tumor presents in discrete nodules, with localized tumors in the lungs or pancreas and distal nodules in the liver. While it is likely that there could be changes in circulation at the tumor sites due to hypervascularization or increased endothelial permeability, it is unlikely that there would be systemic changes to the vasculature in the diseased animals that would drastically change their clearance rates. However, the same cannot be said for leukemia models. Since leukemia is a systemic disease, involving the blood, the spleen, and bone marrow throughout the body, it is likely that a highly diseased animal would have different clearance kinetics from that of a naïve recipient. And in fact, one major goal of this project is to describe how changes in disease state can impact the circulation kinetics. If we were to use the same equations and model as in the solid tumor models, it would be difficult to answer these questions, since the assumption of equivalent clearance rates is crucial to interpreting the results given a steady-state exchange system.

By adding a 3-hour post-blood exchange scan of the recipient mouse following a blood exchange experiment, an exponential decay profile can be fit to the plot of CLC concentration over time to estimate the half-life time of circulating leukemia cells in circulation (Figure 4.4). Two key features are extracted from the decay profiles. First, the fraction remaining describes the relative change in concentration over the course of the 3-hour scan and estimates what fraction of the cells exit circulation over that time period. It can be calculated from the following:

$$Fraction\ remaining = \frac{Concentration\ of\ CLCs\ at\ the\ end\ of\ post\ blood\ exchange\ scan}{Concentration\ of\ CLCs\ at\ the\ start\ of\ post\ blood\ exchange\ scan} \tag{4-1}$$

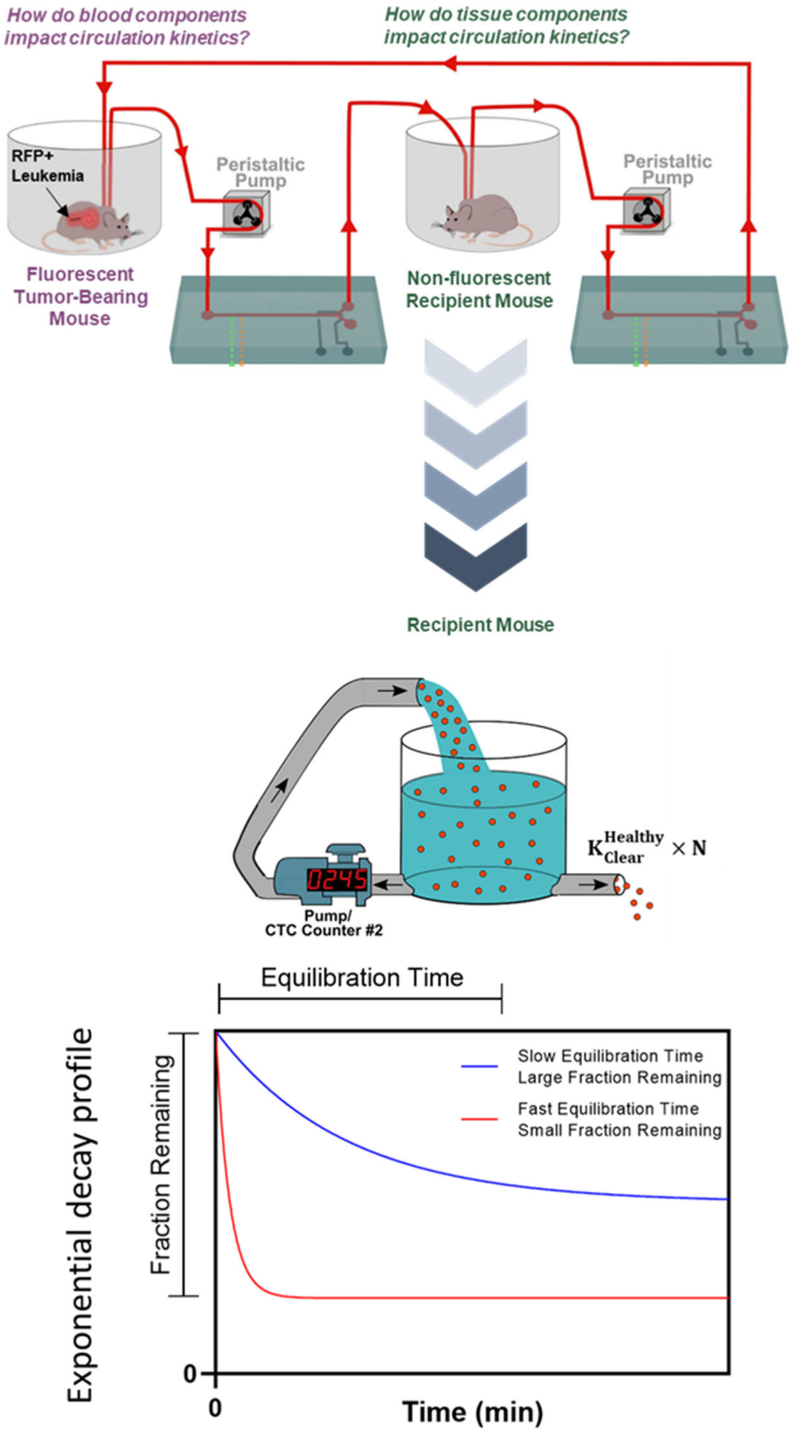

Figure 4.4 Overview of method for estimating circulation kinetics in leukemia models. Following a blood exchange period, where the circulation from a mouse with a fluorescent tumor is connected to that of a non-fluorescent recipient mouse, the recipient is disconnected. The CTC counter is used to monitor the decay profile over a 3-hour post-blood exchange scan. Two key features will be extracted from this scan. The fraction remaining defines the concentration drop of CLCs in the blood of the recipient animal from the beginning of the post-BE scan to the end of the 3-hour scan. The equilibration time defines the exponential decay constant that best fits the 3-hour decay curve, and describes how long it takes for the concentration in the recipient animal to reach a steady state.

The second parameter used to characterize the decay profile is the equilibration time. This parameter is similar to a half-life time and describes how long it takes for the concentration in the blood to reach a steady state. Since not all of the decay curves decay to zero, it is important to add a constant to the equation, such that there is a decay to constant, rather than a decay to zero (a decay to zero would be a half-life measurement). A best fit curve is applied to the decay data, with inputs of concentration and time in minutes, using the following equation:

$$Concentration = a * e^{time/k} + c \tag{4-2}$$

Where k is the equilibration rate in minutes. The parameters a, k, and c are swept over positive values to find the best fit. While the value of "k" is the variable of interest in the equation, the variables "a" and "c" are scaling factors used solely to find the best fit for "k". The variable "c" describes the steady state level of circulation in the mice, but is much less robust of a measurement than the fraction remaining value. Especially when there is a high concentration in the blood at the end of blood exchange, very small changes in measurements in the last few minutes can drastically impact the best-fit "c" value, with relatively little impact on the "k" equilibration

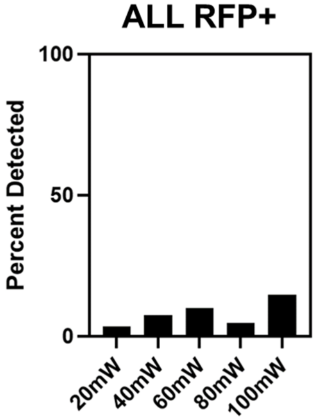

Figure 4.5 Detection percentages of the ALL cell line using the same chip as for the solid tumor models. Even at high laser power, the percent detection does not rise above 20% detection.

rate. Similarly, the variable “a” describes the amplitude from the estimated “c” to the starting concentration, and thus can also fluctuate highly with small changes in measurements.

Aside from the new method of extrapolating circulation kinetic parameters required for the liquid tumor models, differences in the fluorescent intensity of the leukemia models compared to the solid tumor models necessitated a redesign of the microfluidic chip used for detection of CLCs. While the solid tumor models all expressed the very bright TdTomato (red) fluorophore, the two leukemia models are identified through the expression of the dimmer Red Fluorescent Protein (RFP). When run through the same microfluidic chip with the same 20mW laser power, fewer than 5% of cells were detected for the ALL cell line (Figure 4.5). At higher laser powers, up to 100mW, there was still minimal detection, with fewer than 20% of the cells being identified by the system. This necessitated an improvement to the chip design to increase the detection of the leukemia cell lines.

As a first step, we looked to increase the magnification of our objective, thereby narrowing the region of focus, which decreases the background fluorescent noise picked up by the PMT. However, increasing the magnification from 10x to 20x prevented the laser lines from fully

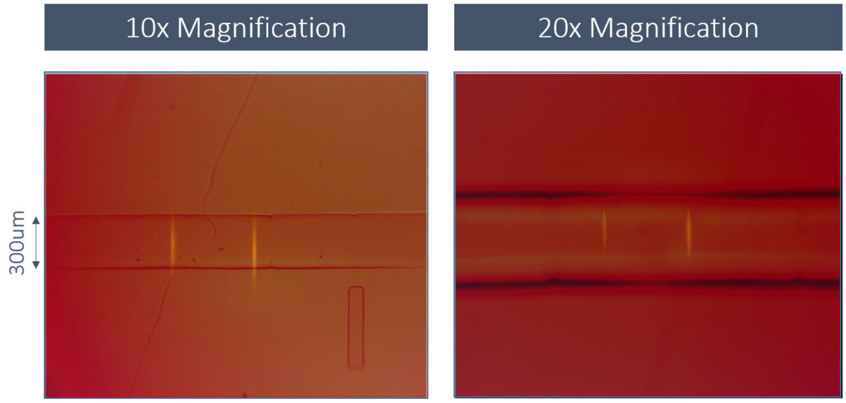

Figure 4.6 Increasing the magnification from 10x to 20x using the same chip design as in the solid tumor models prevents the laser lines from fully covering the 300um channel width.

covering the flow channel (Figure 4.6), which would allow blood and leukemia cells to pass undetected at the channel edge, thereby impairing our ability to accurately determine the real time concentrations and circulation kinetics.

Since higher magnification results in lower background noise, designing a chip that can function using a more powerful objective was crucial to the study of circulation kinetics in leukemia. The chip was thus redesigned such that a narrower channel could pass through the laser lines. Since the purposes of this project do not involve the sorting of cells from blood in real-time, a single inlet and outlet were used, and no valves were required. While the original version of the CTC sorting chip had a channel thickness of 300um, the newly designed chips were fabricated from with channel widths of 100, 150, 200, or 250um (Figure 4.7a). The height was kept the same at 50um. Because no valve layer is required for these devices, fabrication of the mold was performed through negative SU8 resist photolithography, and 1-layer PDMS devices were created by curing a thick ~1cm layer of PDMS on the SU8-on-silicon mold and bonding to glass slides through oxygen plasma treatment (Figure 4.7b).

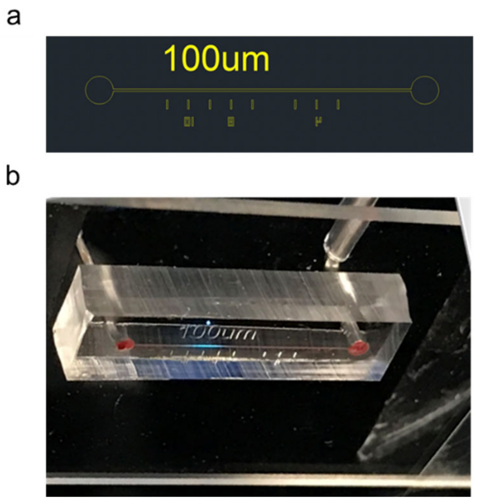

Figure 4.7 New chip for leukemia blood exchange studies. (a) Design of the 100um device. (b) Bottom view of the fabricated PDMS chip

The decreased channel width raised a concern of increased clotting potential, and so the chips were tested by running non-heparinized terminal blood continuously for 15 minutes. None of the channel dimensions resulted in any clotting, and so the smallest width of 100um was chosen to maximize the possible magnification. Because the flow through the system is governed by a constant volumetric flow rate via a peristaltic pump, even thinner channel widths were not explored, as they would increase the linear flow rate through the channel such that the maximum sampling rate of the PMT would not capture a sufficient number of datapoints to confidently identify the fluorescent cells passing through the laser lines. Additionally, the increased flow rate and decreased channel width would apply additional shear stresses onto the passing blood, which could result in cell lysis.

To first test the increased sensitivity of the thin channel chips to detect dimmer fluorescent objects, FACS calibration beads were used. These beads came in 5 brightness levels, with Peak 1 having no fluorescence and Peak 5 being the brightest (Figure 4.8a). The various beads were run through the chip either with the 10x objective that had previously been used, or with a more

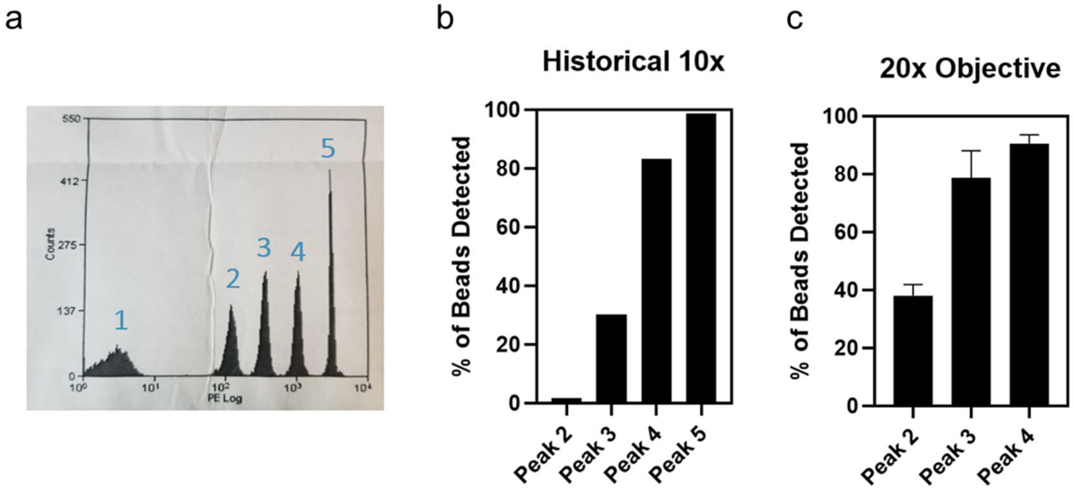

Figure 4.8 Detection of FACS calibration beads at increased magnification. (a) Fluorescent intensity of FACS calibration beads. (b) Percent of beads detected on CTC counter system with 10x magnification. (c) Percent of beads detected on CTC counter system using 20x magnification.

powerful 20x objective (Figure 4.8b-c). While the system using the 10x objective was only able to reliably detect the Peak 4 and 5 intensities, with less than 30% detection of peak 3 and nearly no detection of Peak 2 beads, using a higher magnification allowed for an improved detection rate. Detection of Peak 2 beads increased from under 5% to nearly 40% and Peak 3 from 30% to nearly 80%.

After demonstrating the effectiveness of increased magnification on detection of beads in the thin channel chip, we aimed to explore the maximum magnification possible to use with the system. We applied objectives with 20x, 40x, 50x, and 100x power and observed how the laser lines aligned with the channel. We found that with the 100μm chip, any magnification above 40x resulted in laser lines that were unable to fully cross the channel path (Figure 4.9a). We therefore

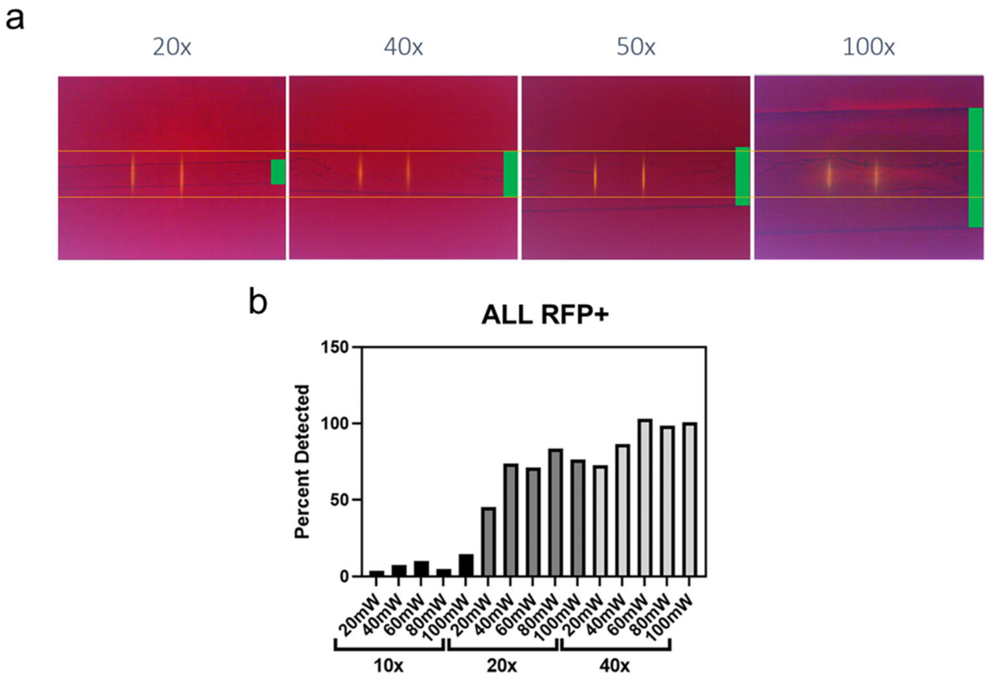

Figure 4.9 Increased magnification in thin channel system. (a) Various optical magnifications were used to identify the maximum magnification that allows for full coverage of the laser lines on the channels. The channel width of 100um is noted with the green bar on the right side of each image, and the extent of the laser lines are shown with yellow lines. (b) Percent detection of the RFP+ ALL cell line increases dramatically with increased magnification. At 40x with high laser power, nearly 100% of cells were detected.

selected the 40x objective to continue with further testing. We retested the ALL cell line at various magnifications and laser powers and saw that the increase in magnification significantly improved the detection capabilities of the system. With the 40x objective, nearly 100% were detected when laser powers about 40mW were used (Figure 4.9b).

Next, it was important to determine whether the higher magnification and laser power negatively impacted the viability of the passing cells. While high laser powers could cause cellular damage, these cells were only exposed to the laser for a fraction of a second, so understanding whether cellular damage occurred was critical to finalizing the settings for the system. We ran the cells through the system either with the laser off or with varying degrees of laser power and objective magnification. Five hours after the scan, we counted the cells and found no difference in the short-term following laser exposure (Figure 4.10a). Next, we used the 40x objective at four laser powers: 0mW, 20mW, 60mW, or 100mW. We flowed equal volumes of the RFP+ leukemia cells through the system at either 60uL/min (or standard flow rate) or 30uL/min (a slower speed

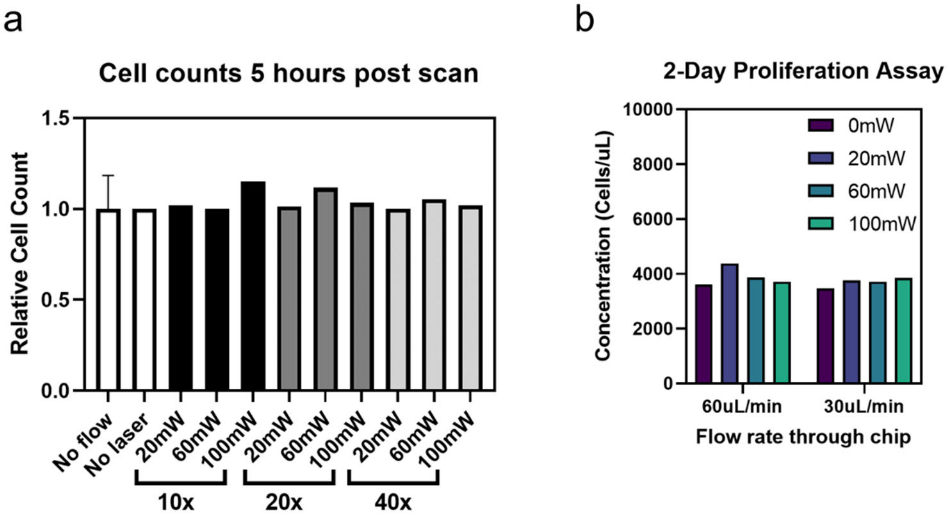

Figure 4.10 Cell survival and proliferation following laser scanning. (a) Cell counts five hours after scanning were not affected by various laser powers and objective magnification (all conditions had >95% viability). (b) Two days following scanning, cells had similar proliferation regardless of the laser power or flow rate they experienced.

that should increase laser exposure and test for higher cell damage) and let the cells grow in the incubator at 37C for 2 days. No difference in proliferation was observed, indicating that even at the highest laser power, no significant damage to the cells occurred (Figure 4.10b). We therefore chose to use 100mW as our standard laser power for the new chip system to maximize our chances of detecting dimmer cells. With the new chip design and optics validated, and with the system assessed for viability of the leukemia cells, we were able to move forward with using the system to study the circulation kinetics of leukemia cells.

4.4 Impact of non-circulatory factors on kinetics of clearance

We started by testing both fluorescent syngeneic models of leukemia to study circulation kinetics, the BCR-ABL driven B-ALL model and the MLL-AF9 driven AML model. By

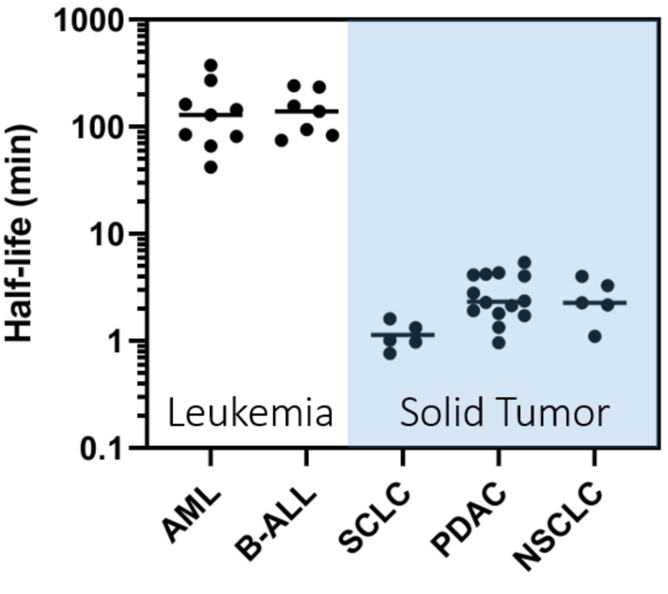

Figure 4.11 comparison of half-life times in liquid tumors (AML and B-ALL) compared to solid tumor models (SCLC, PDAC and NSCLC) in blood exchanges with naïve recipients.

performing blood exchange experiments with healthy mouse recipients, as was done in the solid tumor models, and disconnecting, we could compare the half-life times in circulation of the tumor cells in the leukemia models. We found the half-life times of CLCs in both leukemia models to be several orders of magnitude longer than those of solid tumor CTCs (Figure 4.11), with an average half-life time in the liquid tumor models to be approximately 200 minutes, compared to between 1 and 5 minutes for the solid models.

There are several factors that could influence the circulation kinetics of CLCs. Several studies have suggested that factors relating to the tumor cells themselves, including surface proteins, including integrins and selectins, or physical properties, such as cell stiffness, can contribute to chemotherapeutic resistance[70,100,149]. The physical properties can alter the way that objects flow through channels, pushing them toward the edges, where they could more easily bind to the vascular wall, thereby exiting active circulation[112,150]. Additionally, changes to the vasculature and tumor microenvironment, including endothelial binding proteins, vascular permeability, and ECM deposition, have been shown in leukemia, and could influence how quickly cells can exit from the blood[61,64,151,152]. Finally, increased cell numbers in the bone marrow and spleen, leading to fully packed organs, could contribute to the available space for cell to extravasate into, leading to changes in the circulation kinetic[4,153].

By varying the tumor status of donor and recipient animals, we hoped to distinguish the impact of tumor/blood components from the microenvironment/extravascular state on circulation kinetics, and thereby understand what factors may increase the circulatory compartment of leukemia, leading to more effective responses to therapy. We were also interested in discovering whether any tumor-induced changes to kinetics were due to permanent remodeling of the tissue space, or temporarily induced by the presence of disease.

To begin, we needed a model of disease and treatment for recipient animals as a baseline. We used the ALL model for this purpose, since we had both an RFP+ and RFP- version of the same BCR-ABL driven model. The treatment option explored was a one-dose treatment of the chemotherapy cyclophosphamide (CTX), an alkylating agent that is activated in the liver to produce phosphoramide mustard, which crosslinks DNA to kill actively dividing cells. A single 50mg/kg dose was given intraperitoneally (IP) 8 days after tumor initiation of 500k cells via tail vein injection.

We found that the CTX treated mice had a 2-3 week life extension compared to the untreated animals (Figure 4.12a). Additionally, histology sections show dramatic changes in the

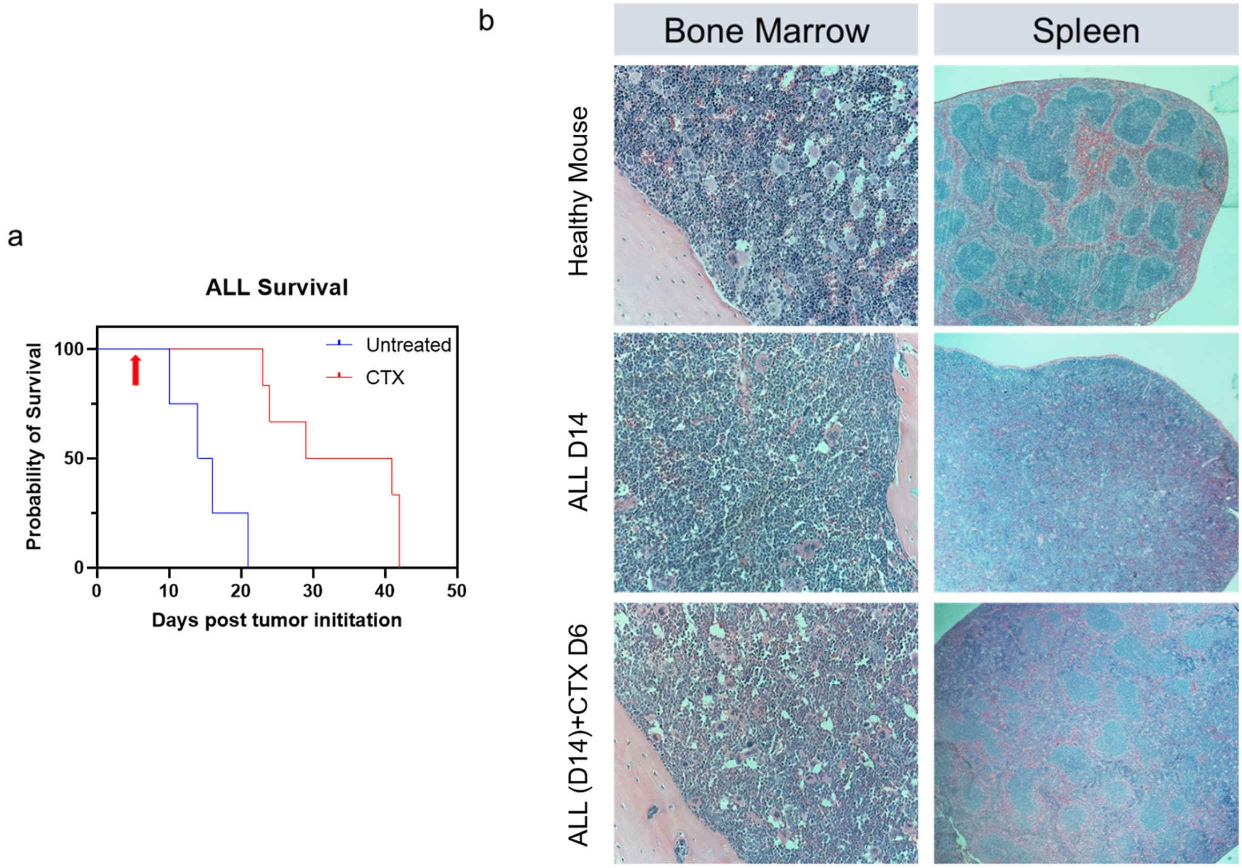

Figure 4.12 Cyclophosphamide (CTX) treatment of ALL model. (a) Survival curve shows 2-3 weeks life extension in mice treated with one dose of 50mg/kg CTX 8 days post tumor initiation. (log-rank test p value = 0.0019). (b) Histology sections of bone marrow and spleen of healthy mice, diseased ALL mice at 14 days post initiation, and mice 6 days post treatment show major alterations to tissue in the context of disease, which are at least partially reverted upon treatment.

spleen and bone marrow were at least partially reversed through treatment (Figure 4.12b). In the healthy bone marrow, diverse populations of cell types, including many large megakaryocytes, were present, and open spaces of adipocytes were present. As disease developed in the mice (ALL D14), there was much more homogeneity of cell types, as the leukemia cells crowded out the normal blood cells and created a much denser tissue. After treatment (ALL (D14) + CTX D6), the marrow contained a higher diversity of cell types and less densely packed cells, suggesting a return to a more normal histology. Similar trends were seen in the spleen. In the healthy spleen, a normal architecture, regions of blue "white pulp" surrounded by the red "red pulp", was seen. But in the context of disease, the structure was highly disrupted, and leukemia cells crowded out the space. The spleen was also highly enlarged and could be up to 10 times more massive than a healthy spleen. In the treated mice, the spleen shrank back toward a normal size and began to show the reemergence of normal architecture, as the white pulp was clearly discernible.

Next, we looked at whether changes to the tissue associated with disease had an impact on the circulation kinetics of the CLCs. We started by comparing clearance rates when an RFP+ ALL mouse was connected to a naïve healthy mouse (HM) as opposed to a mouse with a non-fluorescent ALL disease (RFP-). We found a striking difference in the clearance profiles (Figure 4.13a). While clearance of RFP+ ALL CLCs followed a steady decrease over the 3-hour post-blood exchange scan in a naïve healthy mouse, in a diseased mouse there was a relatively small drop followed by a period of very stable circulation levels. And in a CTX-treated mouse (RFP- treated), the clearance kinetics returned to that of the healthy mice.

We quantified these changes by calculating the fraction of cells remaining in circulation from the beginning to the end of the 3-hour post-blood exchange scan. The data showed approximately 2-fold increase in fraction remaining in the diseased (RFP-) recipients compared with healthy mouse (HM) recipients, about 0.6 compared to 0.3 (Figure 4.13b). This phenotype was fully reversed with CTX treatment (RFP- treated), where recipient mice returned to a fraction remaining of approximately 0.3. These findings suggest that changes in non-circulating factors in a diseased state impart a transient decrease in the extravasation potential of CLCs that is reversible through treatment.

Because the changes are reversed within several days after CTX treatment, it is unlikely that such changes are due to vascular remodeling, since these processes can take up to three weeks to be observed[154]. This suggests that temporary changes in the extravascular tissue or changes in endothelial cells lead to the differences in decay kinetics, rather than more permanent remodeling.

As a next step, we wanted to see whether the hypercellularity associated with a diseased state could be contributing to the changes in circulation kinetics. Based on the findings, one could infer that the increased hypercellularity of the bone marrow in the diseased state prevents CLCs

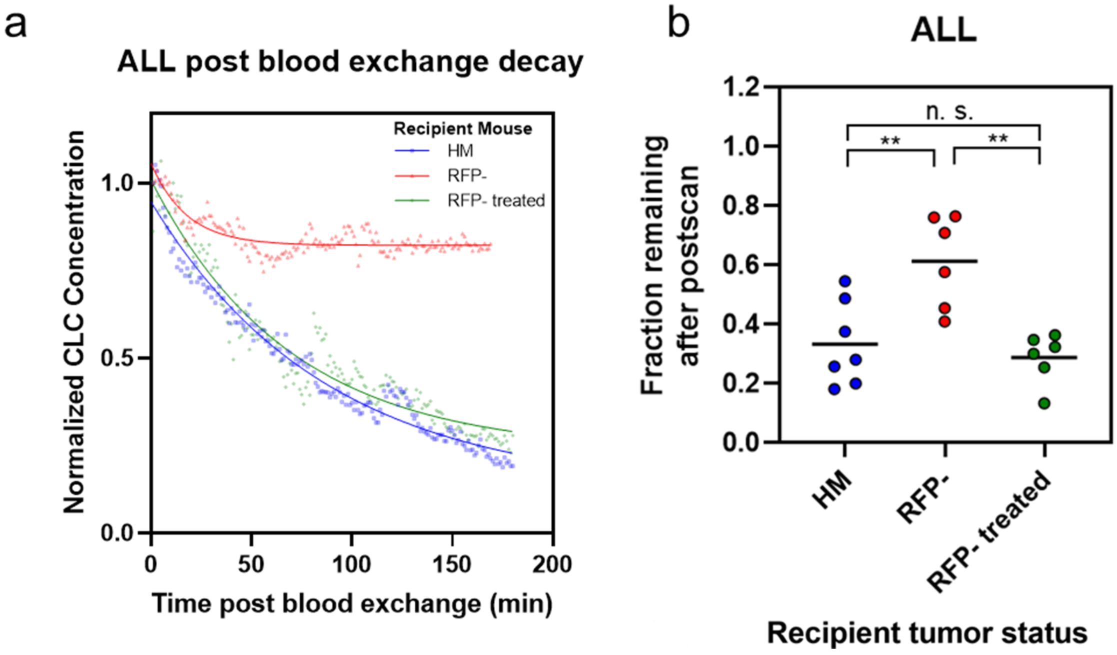

Figure 4.13 Clearance of ALL CLCs in recipient mice with varied tumor status. (a) Normalized CLC concentration after being disconnected from blood exchange shows a profound difference in clearance kinetics with a diseased state (RFP-) compared with a healthy (HM) or CTX treated (RFP- treated). (b) Fraction remaining at the end of the post-blood exchange scan shows significantly increase with a diseased recipient compared to healthy or treated. (**p<0.005; Tukey's multiple comparison test)

from exiting circulation simply because there is no physical space for them to exit into. And when the mice are treated with chemotherapy, the freeing up of space associated with cell death allows for more cells to extravasate, returning the clearance rates back to the baseline seen in the healthy mice. Because there are few ways to increase cellularity without inducing a cancerous state, we decided to ask the alternate question of whether increasing empty space in the bone marrow in a healthy mouse could induce the opposite observation. To that end, we compared the clearance rates of ALL CLCs in healthy recipients that had been treated either with chemotherapy (1 dose of 50mg/kg CTX) or irradiation (1x 5Gy), which kills all rapidly dividing cells, including normal blood cells in the bone marrow. First, we confirmed that both chemotherapy treatment and irradiation induced hypocellularity in the bone marrow of healthy mice. Histological findings showed a dramatic reduction of cells in the bone marrow (Figure 4.14a), and half to two-thirds reduction of total cells in the bone marrow (Figure 4.14b). Then, we performed blood exchange experiments using ALL RFP+ donor mice and monitored the decay in the post-blood exchange scan (Figure 4.14c). While there was a small change in the clearance, there was no significant decrease in the fraction remaining at the end of the post-blood exchange scan in either the irradiated or chemo-treated healthy mice (Figure 4.14d). This could either suggest that cellularity of the tissue does not significantly influence the clearance kinetics, or that there may be a lower limit, such that inducing hypocellularity does not allow for additional cells to exit circulation into the marrow.

Both of these interpretations suggest that cellularity alone does not sufficiently change the kinetics of CLCs, and might suggest that something with the endothelium plays a role. However, the increased vascular permeability associated with endothelium in the context of leukemia does not seem to agree with our observations. That is, increased vascular permeability in a diseased state would likely decrease the fraction of CLCs remaining, rather than increase it as we saw in our results. Therefore, we decided to look into changes in the endothelial binding proteins to see if they were the primary culprit in keeping the CLC fraction high in diseased mice.

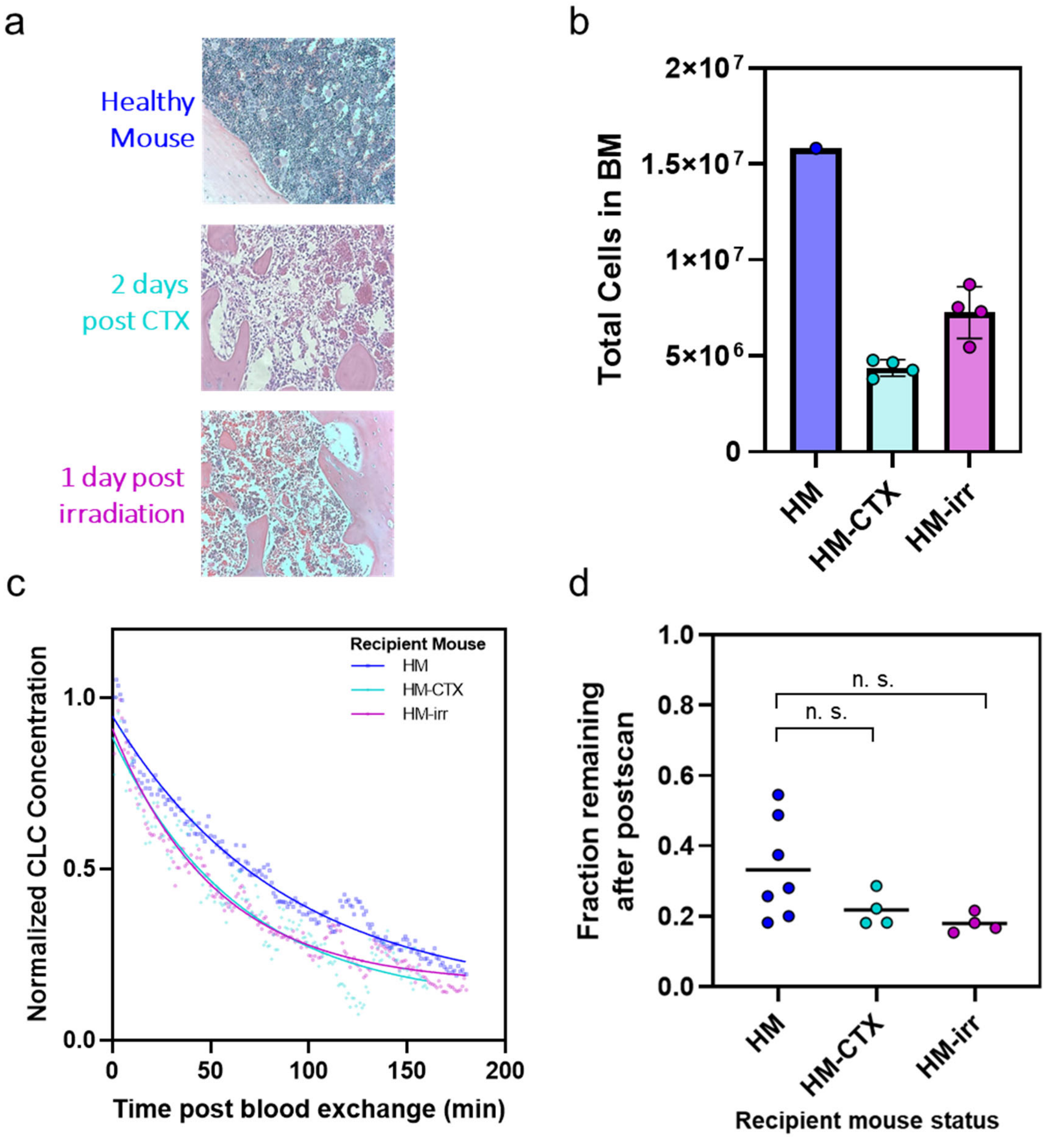

Figure 4.14 Hypocellularity does not induce significant reduction in fraction remaining after post-blood exchange scan. (a) Histology shows significant decrease in cellularity of bone marrow upon either chemotherapy treatment (CTX) or irradiation (1x 5Gy). (b) Cell counts shows half to two-thirds reduction in total cell count of the bone marrow (BM) after chemotherapy or irradiation. (c) Decay profiles show modest change in clearance rate in the depleted mice compared to healthy mice. (d) A slight, but non-significant, decrease in fraction remaining at the end of post-blood exchange scan was observed in hypocellular mice. $p = 0.09$ and 0.22 comparing HM to HM-CTX and HM-irr respectively; Tukey's multiple comparison test.

We performed flow cytometry analysis on bone marrow endothelial cells throughout the course of disease and treatment. The two endothelial surface proteins associated with adhesion that we looked at were E-selectin and VCAM1. E-selectin binds several glycans and glycoproteins by binding to sialylated carbohydrates[100]. E-selectin is important in leukocyte recruiting, and is upregulated in response to inflammatory cytokines, including TNF-α (tumor necrosis factor α), and IL-2 (interleukin 2)[4]. VCAM1 binds to the integrin VLA4 (very late antigen 4: α4β1) and has been implicated in regulating ALL chemotherapy resistance[105,106].

Bone marrow cells were isolated through manual grinding with mortar and pestle, and red blood cells removed through ACK lysis buffer before staining. Flow cytometry was then used to identify the fraction of endothelial cells expressing the adhesion proteins. The gating strategy used for identifying bone marrow endothelial cells (BMECs) is shown in Figure 4.15a. After selecting for single cells through forward and side scatter, endothelial cells were selected as DAPI- (live), CD31+ (endothelial marker), and CD45- (white blood cell marker). A cutoff on the endothelial cells in the channel of the adhesion molecule antibody (PE for E-selectin and FITC for VCAM1) was used to identify high expressing cells within the BMECs. Treated mice were given 1 dose of CTX 8 days after tumor initiation. Diseased mice (B-ALL) and acutely treated mice (B-ALL + CTX) were analyzed on day 10 post initiation (2 days post CTX for the treated mice), and relapse mice were analyzed on day 25-27 post initiation (15-17 days post CTX).

For E-selectin, we found an increase in the percent positive expression of BMECs from about 5% for healthy and acutely treated mice, to around 15% in diseased and relapse mice (Figure 4.15b). This finding correlates with the findings from the blood exchange experiments with diseased and treated mice, where a shift in the phenotype with a diseased recipient was reversed through treatment. These findings match previously reported findings of acutely treated AML, as well as data that suggest AML cells create inflammatory signaling that upregulates E-selectin expression on BMECs[100].

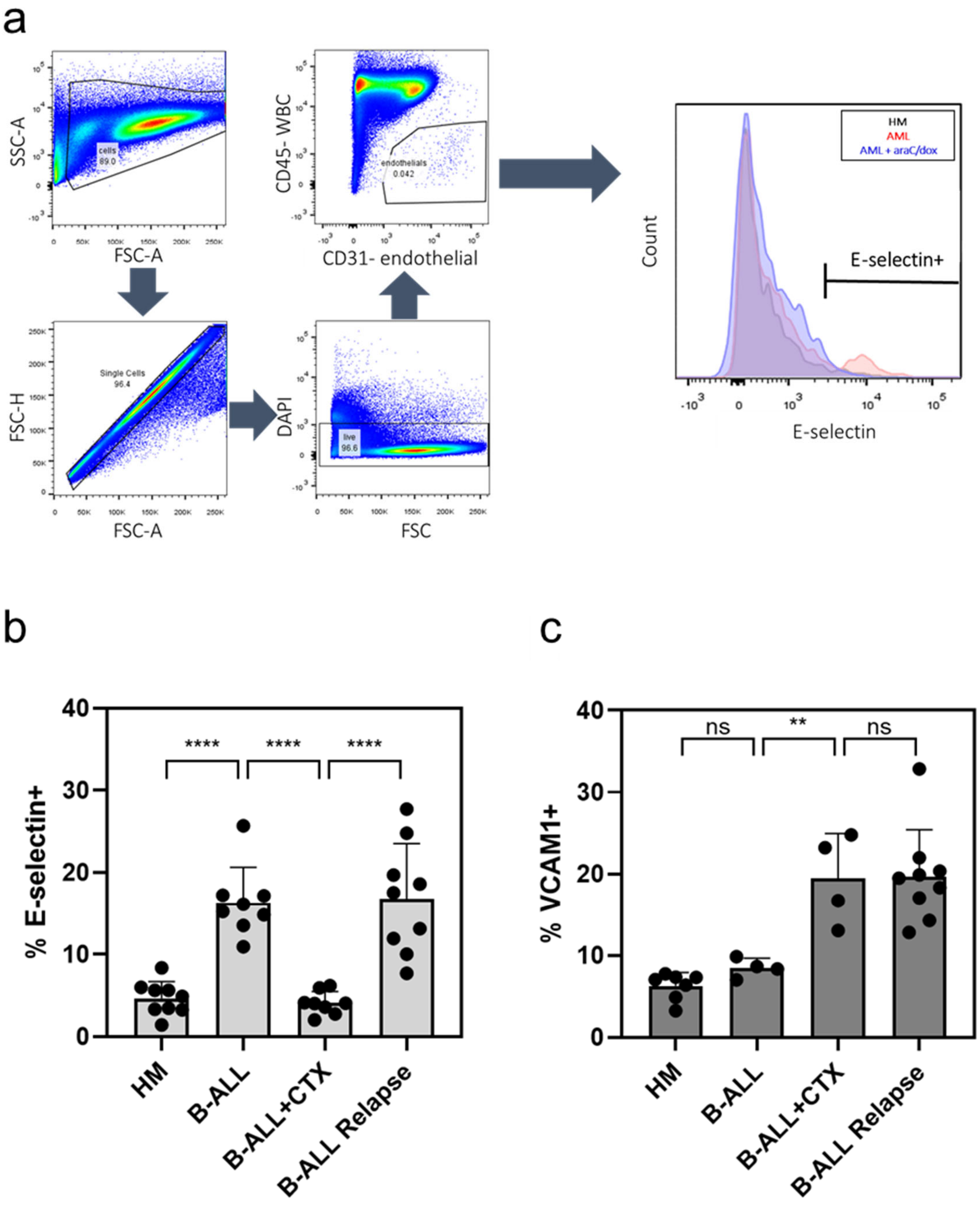

Figure 4.15 Flow cytometry analysis of adhesion expression on bone marrow endothelial cells. (a) Gating strategy for measuring expression on endothelial cells (DAPI-, CD31+, CD45-). Example shows increase with AML disease that is reverted after treatment of cytarabine and doxorubicin (araC/dox). (b) E-selectin expression increases and decreases over the course of disease (B-ALL) and acute treatment (B-ALL + CTX), and increases again at relapse. (****$p<0.0001$; Tukey's comparison test) (c) VCAM1 expression does not increase with disease but is increased and remains elevated after treatment through relapse. (**$p=0.0093$, ns: $p>0.85$; Tukey's comparison test)

For VCAM1, a different phenotype was observed (Figure 4.15c). Both the healthy mouse and diseased mouse had similarly low levels of VCAM1 expression, around 5-10%. However, after CTX treatment, the levels of VCAM1 increased and remained elevated until relapse at around 20%. Interestingly, CTX treatment in healthy mice did not induce a similar increase in VCAM1, suggesting that the presence of tumor in combination with treatment is required to induce and increase in VCAM1 expression (Figure 4.16). These findings indicate that VCAM1 is unlikely to influence the clearance rates, as it is not upregulated between the healthy and diseased conditions and is increased in the treated state.

Since the E-selectin expression modulated over the course of disease and treatment, we decided to test whether inhibiting the E-selectin expression on BMECs using blocking antibodies would reverse the shift in clearance kinetics observed from blood exchange experiments. We used RFP- ALL mice as the recipients of blood exchange with RFP+ ALL mice, but dosed the recipient with 100μg of α-E-selectin antibody intravenously 20 minutes before the start of blood exchange (Figure 4.17a).

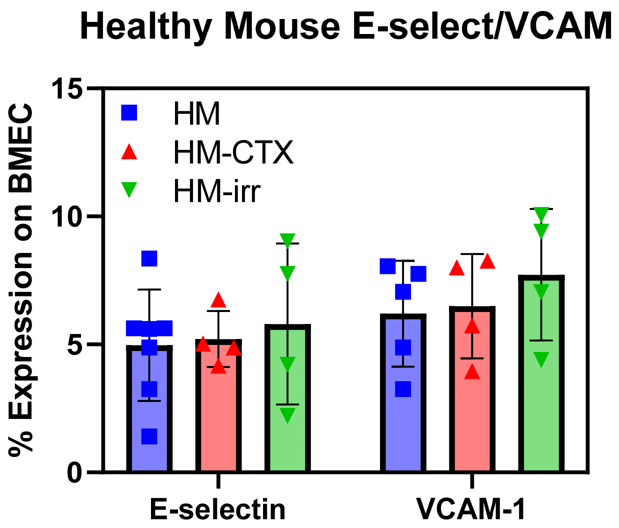

Figure 4.16 Expression of E-selectin and VCAM1 on BMECs of healthy mice (HM), healthy mice 2 days post CTX (HM-CTX), and healthy mice 1 day post irradiation (HM-irr). Tukey's multiple comparison test showed p values >0.57 for all pairs

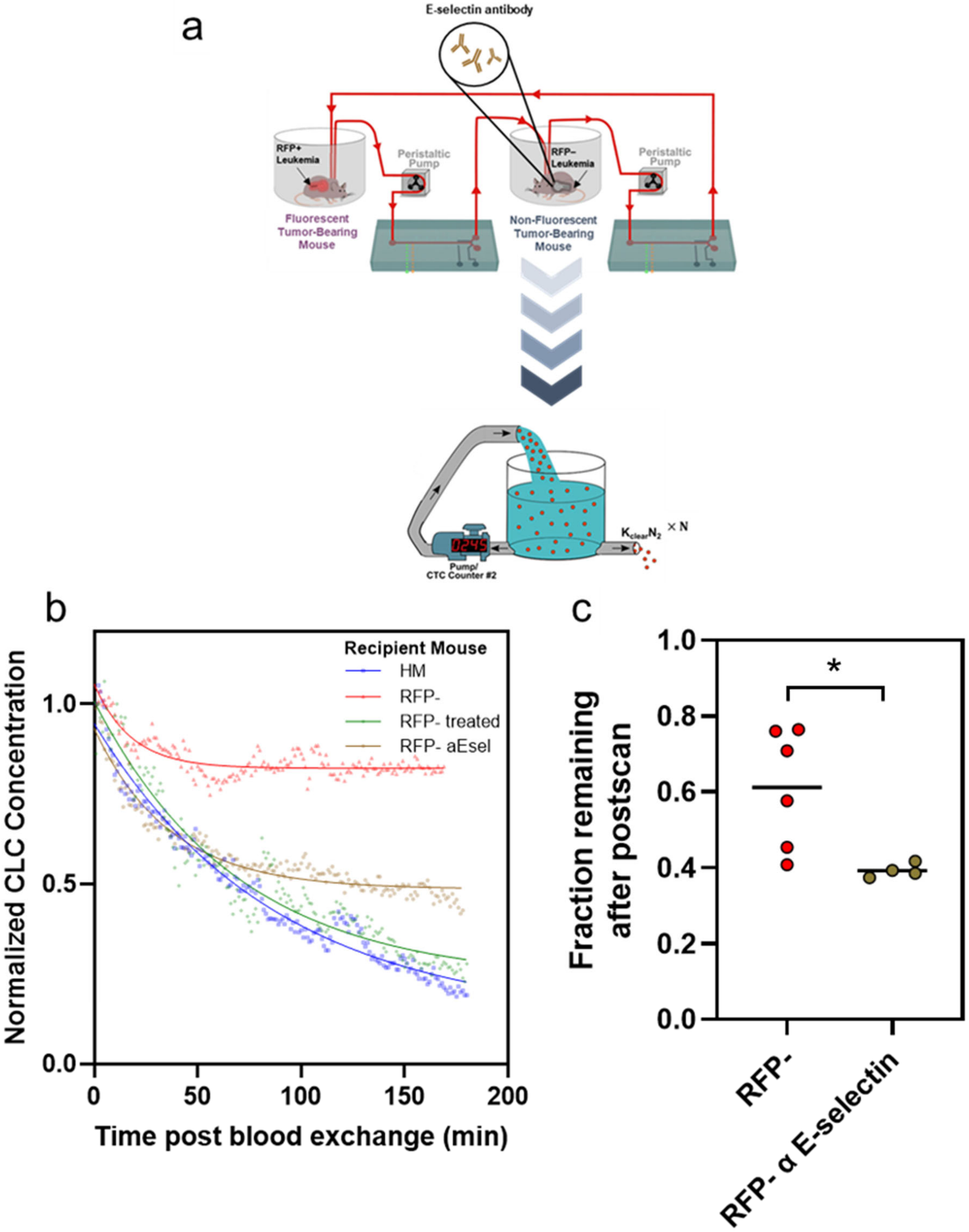

Figure 4.17 Blood exchange in diseased mice with α-E-selectin. (a) Overview of experiment. RFP- recipient mouse was injected with 100μg of E-selectin antibody 20 minutes prior to blood exchange. (b) Decay profiles of post-blood exchange scans show a shift from the RFP- mice. (c) E-selectin treated mice (RFP- aEsel) had decreased fraction remaining compared to the non-dosed RFP- mice. (* $p=0.025$ with unpaired two-tailed t-test)

The decay profile of RFP- mice dosed with E-selectin antibody showed a distinct shift from the non-dosed RFP- mice (Figure 4.17b), and the fraction remaining at the end of post-blood exchange scan was found to be significantly lower in diseased mice treated with E-selectin antibody (Figure 4.17c). These results show that modulating E-selectin expression alters the circulation kinetics of CLCs. This likely occurs because of the retention capabilities of E-selectin. A previous study showed that the inhibition of E-selectin led to an increase in the circulating number of CLCs in a model of AML[100]. By blocking E-selectin, several factors are likely in play. In the non-fluorescent diseased recipient mouse, high levels of E-selectin on BMECs likely bind up leukemia cells both along the vascular walls and in the marrow, creating a fairly static environment with minimal mixing between the blood and bone marrow compartments, preventing the fluorescent donor cells from exiting circulation. By blocking E-selectin in this recipient environment, non-fluorescent leukemia cells of the recipient could be released and more free to interchange between blood and marrow, allowing for the infused fluorescent donor cells to clear more readily. Another contributing factor is that blocking E-selectin decreases the available adhesion proteins, which could prevent some circulating cells from binding to the vascular walls, where they can exit circulation, which would result in less clearance of fluorescent donor cells from the blood. The results from our experiments, where we see more clearing when E-selectin in blocked, suggests that the former explanation is more critical to defining the circulation of CLCs. By blocking E-selectin in the diseased recipient, non-fluorescent leukemia cells from the marrow can enter into the blood more easily, allowing for higher turnover of cells between the compartments. This then allows for the fluorescent cells from the donor mouse to flow more freely into the marrow, leading to the observed decrease in fraction remaining at the end of the post-blood exchange scan.

4.5 Impact of circulating factors on clearance kinetics

To address whether changes in the tumor cells themselves can alter their circulation kinetics, we varied the mice used as donors in our blood exchange pairs. This allowed for the introduction of fluorescent cells of different conditions clearing in the same healthy mice, and served as a method of decoupling changes imparted from the tissue with those imparted from the tumor cells themselves.

Our first experiment was to vary the disease burden of the donor to test whether the leukemia models evolve over the course of disease to alter the rate of clearance in healthy mice. The burden of CLCs in the blood of our AML and ALL models increases several orders of magnitude over the 2 to 3-week course of disease, and the number of days post tumor initiation (days post injection) correlates well with the burden in the blood (described earlier in Figure 4.2). We performed blood exchange between RFP+ diseased mice and healthy counterparts at various timepoints of detectable disease burden in the blood and monitored the decay kinetics in the recipient mice for a 3-hour scan after disconnecting from blood exchange. We looked at the two main parameters for the decay profile, fraction remaining and equilibration rate, and plotted the values against the days post tumor initiation (Figure 4.18). We found that neither of these decay parameters had a significant correlation with the disease burden in either model of leukemia.

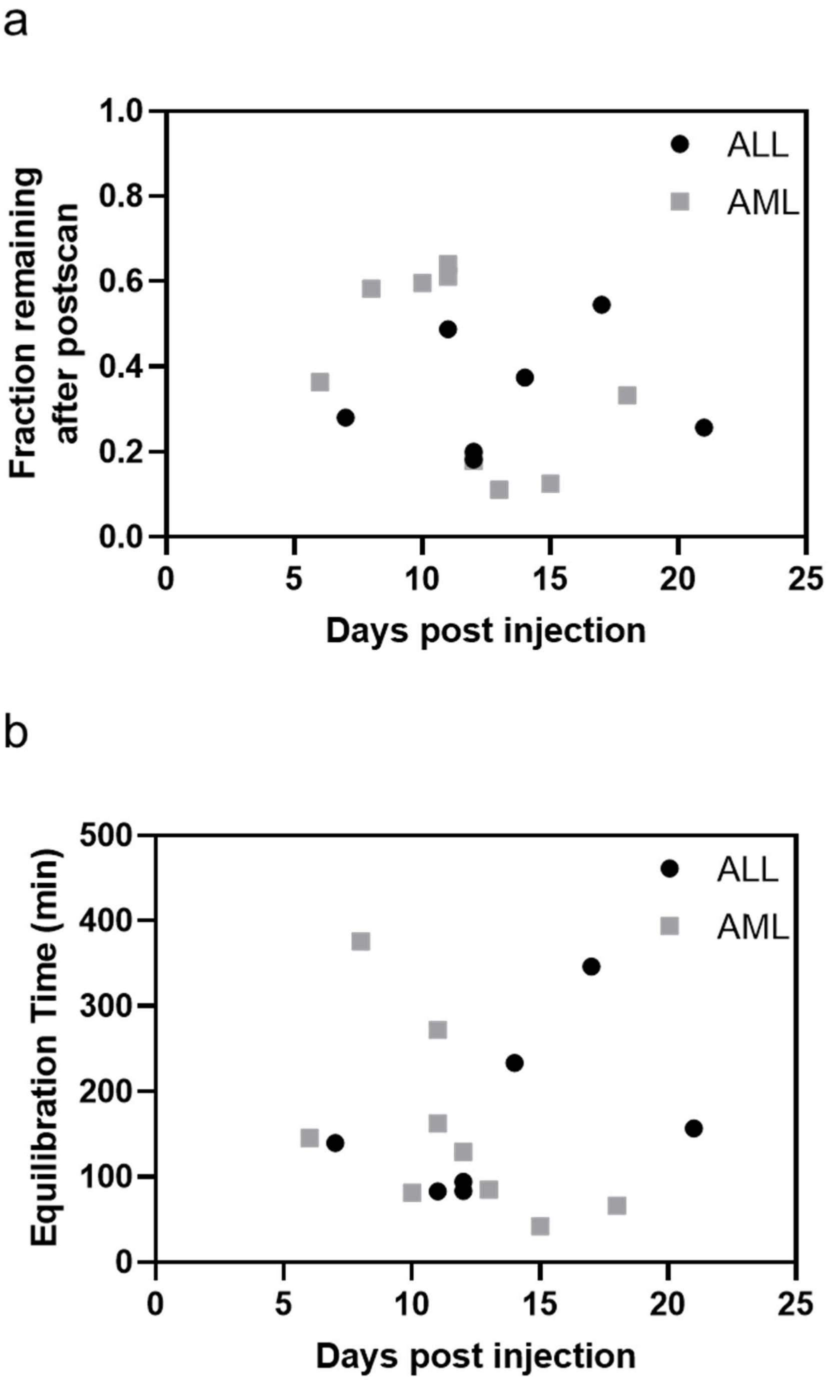

Figure 4.18 Circulation kinetics with varied donor disease burden. (a) No correlation is seen in either leukemia model between days post tumor initiation and fraction remaining at the end of post-blood exchange scan. R^2 values of 0.02 and 0.21 for ALL and AML respectively, with non-significant p-values 0.75 and 0.21 respectively. (b) No correlation is seen in either leukemia model between days post tumor initiation and equilibration time. R^2 values of 0.21 and 0.32 for ALL and AML respectively, with non-significant p-values 0.30 and 0.11 respectively.

These findings are not necessarily surprising. The models we are using are both based on injected cell lines and are relatively short models (less than 3 weeks to morbidity), which may not have sufficient time to evolve dramatic physical and transcriptional changes that would impact the clearance rates. Nonetheless, these findings suggest that there are no significant changes to the CLCs between low and high tumor burden in the blood that is enough to impact the clearance of these cells in healthy recipients.

Since we saw no significant impact of disease burden on circulation kinetics, we decided to test whether treatment, and relapse in particular, led to a change in the tumor cells that could affect the clearance rates. For the ALL model, we used the same dosing regimen as before (1 dose of 50mg/kg CTX 8 days post tumor initiation). For the AML model, we used a 5+3 treatment of cytarabine (araC) and doxorubicin (dox). For 5 days, beginning 8 days post tumor initiation of 500k AML cells, the mice were dosed IP with 20mg/kg araC. And on the first three of those days (days 8-10 post tumor initiation), mice were given a concurrent dose of 2mg/kg dox. The 5+3 araC/dox treatment provided roughly one week life extension (Figure 4.19a). Histologically, treatment freed up space in the bone marrow that was refilled by late relapse (Figure 4.19b). And relapsing mice attained similar levels of CLCs in the blood as were reached in the untreated mice, and increased at a similar rate, shifted approximately one week (Figure 4.19c).

We next used these treatments to explore whether relapse CLCs had a different clearance profile than untreated mice. In our ALL model, we saw similar clearance kinetics in the recipient healthy mice, with no change in the equilibration time (Figure 4.20a-b). However, in the AML model, a striking difference was observed. While the clearance profiles showed that the fraction remaining at the end of the post-blood exchange scan were similar in both cases, the relapse AML CLCs had a very rapid initial clearance (Figure 4.20c). Quantitatively, this was reflected in the

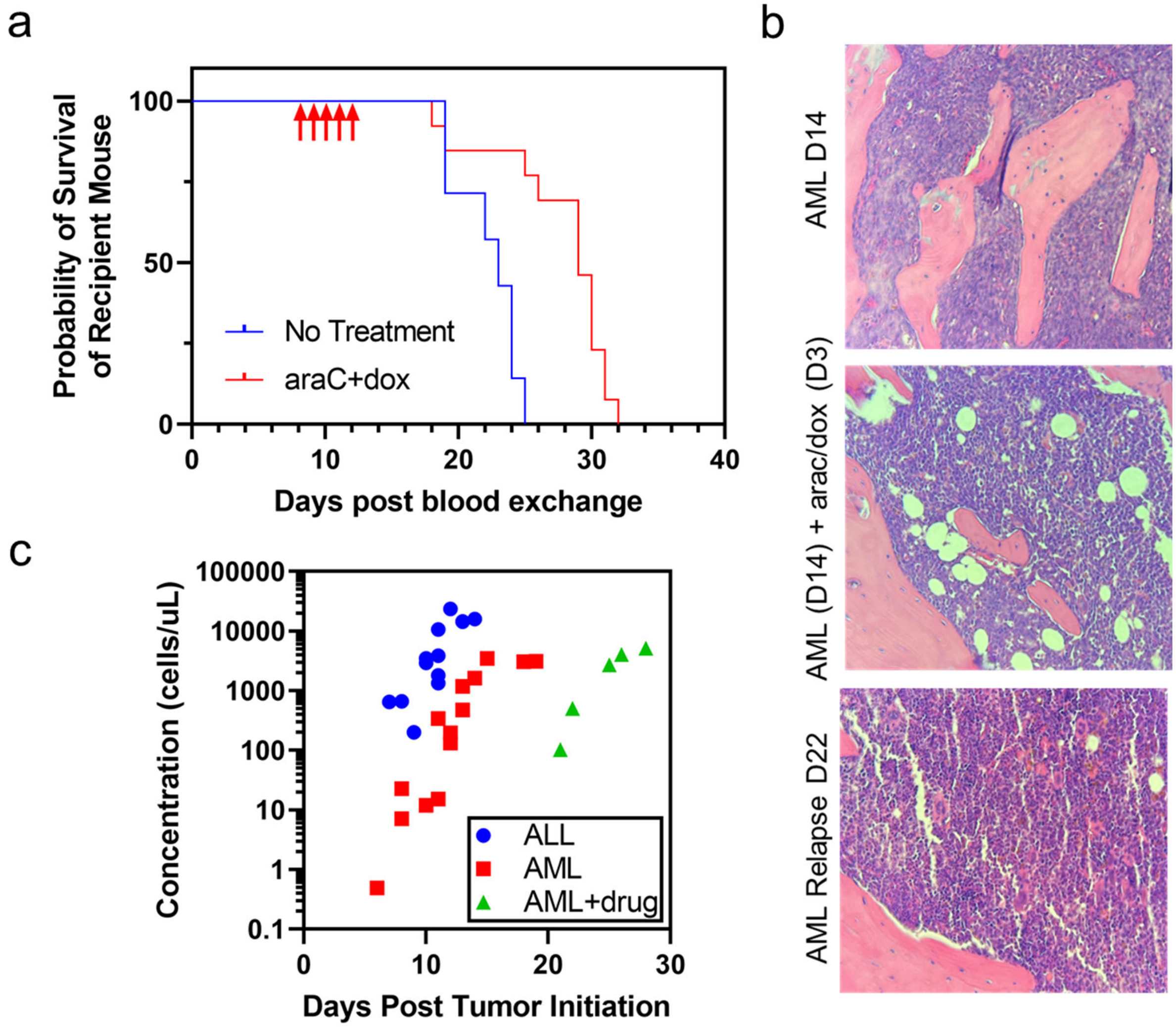

Figure 4.19 Drug treatment in AML model. (a) A 5+3 dosing regimen of cytarbine (araC) and doxorubin (dox) (5 days of 20mg/mL araC, with first 3 days receiving concurrent 2mg/mL dox) results in approximately 6 day extension in life (log-rank test p value = 0.0008). (b) Histology showing bone marrow from diseased (AML D14), acutely treated (AML + araC/dox D3), and relapsing (AML Relapse D22) mice. (c) Blood burden of CLCs with drug treatment shows relapsing disease attains similar levels of CLCs at a delay of about 1 week.

equilibration times, where relapse CLCs had a significantly faster equilibration than the untreated CLCs, over 100 minutes in the untreated mice compared to around 20 minutes in the relapse mice (Figure 4.20d).

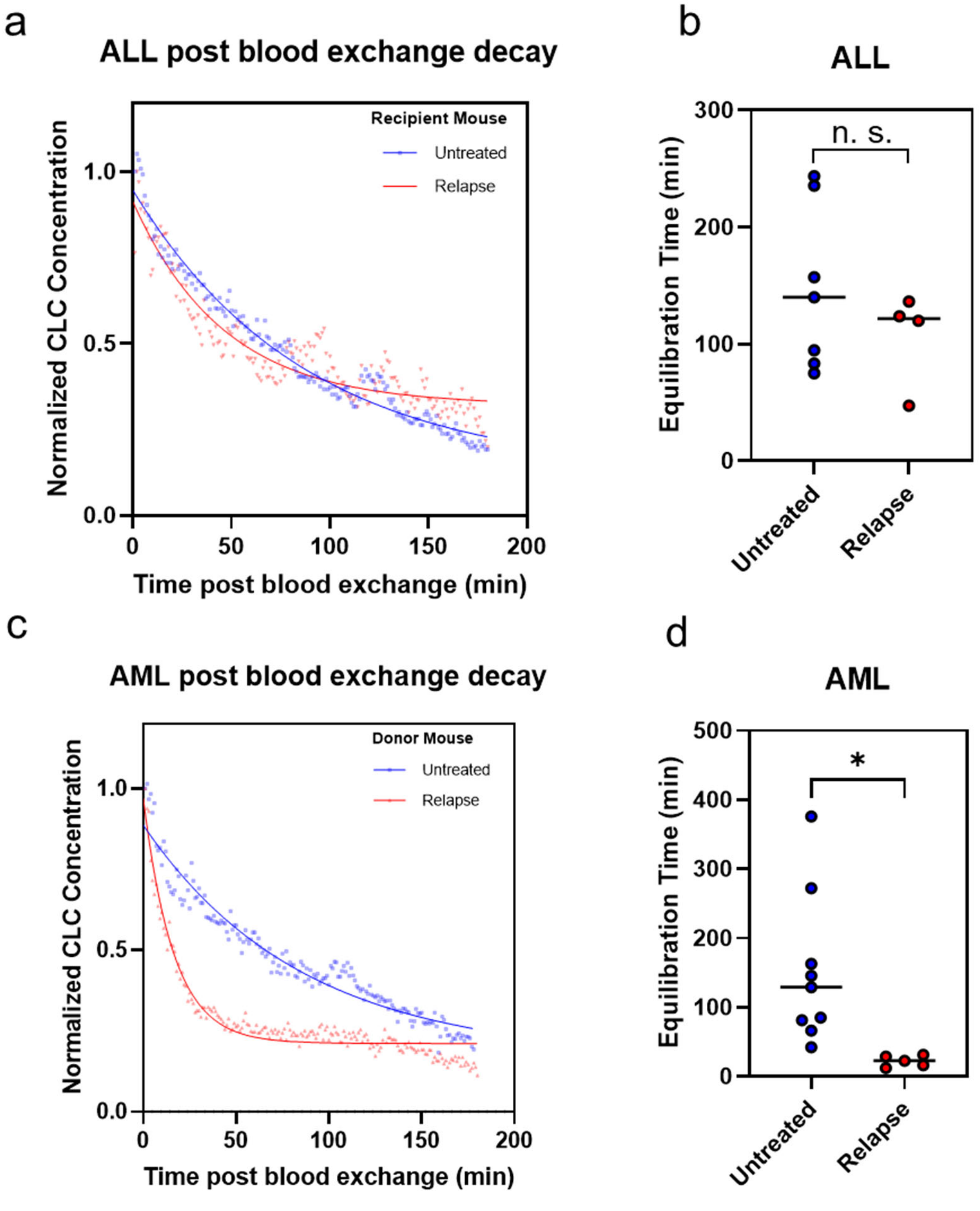

Figure 4.20 Blood exchange with relapsed donors. (a-b) Decay profile and quantification of clearance rates in healthy recipients with either untreated or relapse ALL donor mice shows no significant difference in equilibration time (two tailed t-test p value = 0.33). (c-d) Decay profile and quantification of clearance rates in healthy recipients shows AML donors with relapse disease have significantly faster equilibration time compared to untreated donors (two tailed t-test p value = 0.023)

These findings suggest two things. First, something in the AML relapse CLCs is sufficiently different than in the untreated cells to impart an altered clearance rate. This could be due to a change in biophysical properties of the cells, such as cell volume or mass, that would change the fluid dynamic properties of the cells in the vasculature that could allow them to more rapidly exit circulation. If the relapse CTCs are larger, heavier, or stiffer, they would be more likely in a fluidic system to be pushed toward the edges, leading to faster clearance rates[112,150]. Alternatively, a change in the surface proteins of the cells could alter the adhesion capacity to the endothelium. Stickier cells could more readily bind to the vessel walls, resulting in a faster clearance.

Second, these findings indicate that the changes that occur between untreated and relapse CLCs in the AML model do not occur in the ALL model. If both models experienced the same changes, either in biophysical properties or surface molecule expression, then we would expect to see a similar decrease in the equilibration rate in the ALL relapse scenario, which was not observed.

To begin exploring what features of AML relapse impart the changes to circulation kinetics, we analyzed the biophysical properties of the leukemia cells both of untreated and relapse tumors. The tool we used to characterize the cells is device our lab developed called a suspended microchannel resonator (SMR) (Figure 4.21a). The device consists of a hollow microfluidic cantilever that vibrates in the z direction (like a springboard) at its resonant frequency. As cells flow through the vibrating cantilever, the added mass from the cell changes the resonant frequency of the cantilever in proportion to the buoyant mass of the cell. Using this system, incredibly accurate measurements of buoyant mass can be made for single cells[142–144]. Additionally, a fluorescent exclusion method can be used to assess the volume of single cells. By flowing the cells past a detection region in a media with fluorescent dextran, which is cell impermeable, a drop in fluorescence will be observed proportionally to the excluded dye, which equals the volume of the cell. In this way, we can measure both the buoyant mass and volume of single leukemia cells (Figure 4.21b). We found that there were no significant differences in the measured biophysical properties of untreated and relapse AML, suggesting that physical changes in the CLCs do not explain the observed differences in clearance kinetics.

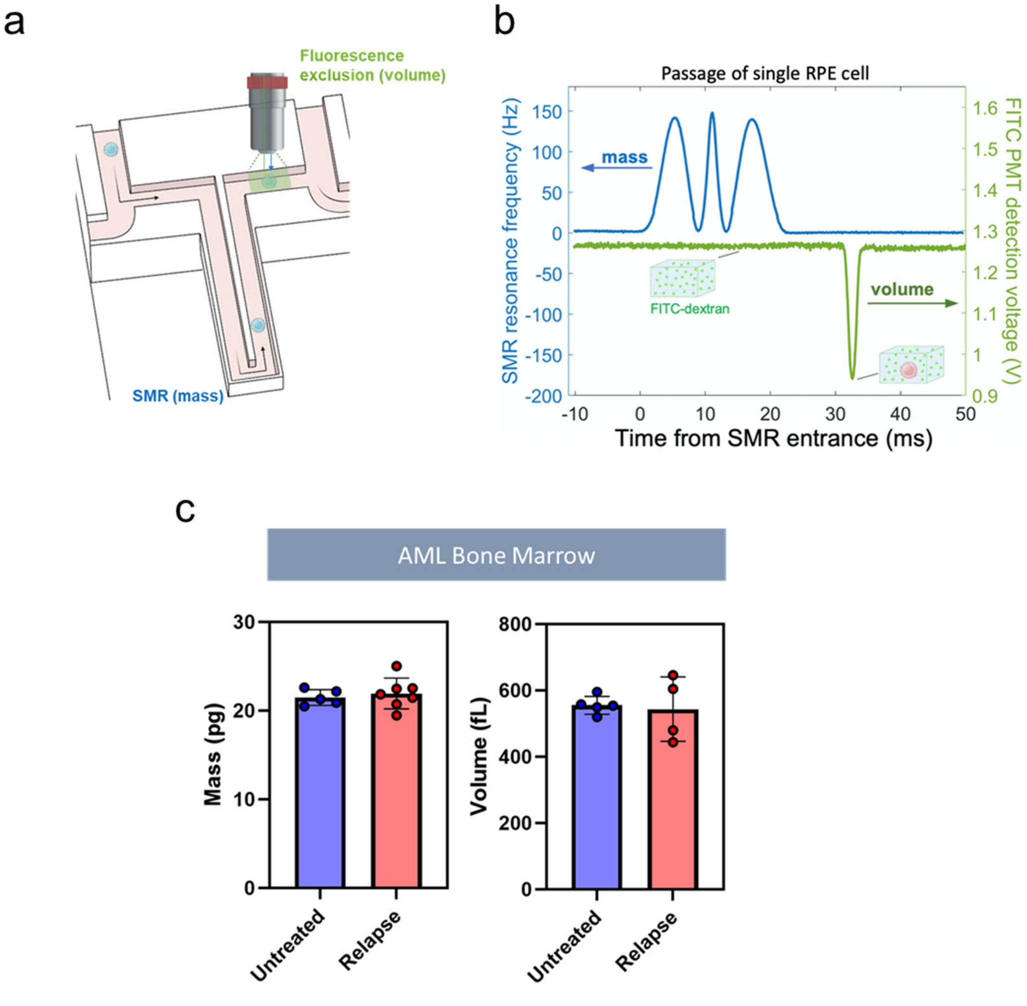

Figure 4.21 Biophysical properties of untreated and relapse AML tumor cells. (a) Schematic of SMR with volume exclusion. (b) Examples showing how change in resonant frequency gives a mass readout (blue) and change in fluorescence gives a volume measurement (green). (c) No change in mass or volume of bone marrow cells was observed between untreated and relapse AML mice. ($p=0.61$ and 0.80 respectively for mass and volume from 2-tailed t-test)

We then focused to explore whether there were changes in the expression of surface adhesion molecules that could explain the increased clearance rate in relapsing cells. If the cells indeed are more likely to adhere to the vascular walls, that would readily explain the observed changes in kinetics that is seen in our blood exchange experiments. We assessed the presence of three binding molecules using flow cytometry, on leukemia cells in both the blood and bone marrow compartments. Because E-selectin, found on endothelial cells, binds to silyl groups of glycans and glycoproteins, there is no single antibody to effectively assess the ability of leukemia cells to bind E-selectin. As such, we incubated the leukemia cells with a fluorescently conjugated E-selectin protein (using a chimera of recombinant mouse E-selectin and human IgG with a fluorescent α-human IgG antibody). To assess the capacity to bind VCAM1, another endothelial adhesion molecule, we incubated leukemia cells with an antibody for integrin β1, part of the integrin dimer VLA4 that binds to VCAM1. However, because integrins have several opened and closed configurations with various capacity to bind VCAM1, similar levels of the integrin on the surface could have varied capacity to bind due to slight changes in their configurations[155]. Therefore, we also used a binding assay with fluorescent recombinant VCAM1 to directly assess the capacity of the leukemia cells to bind VCAM.

For the AML model, we found significant differences in the expression of the various binding molecules between untreated and relapse cells in both the blood and bone marrow compartments, with relapse cells having universally higher expression (Figure 4.22a-c). Similar trends between untreated and relapse disease were seen in the ALL model as well, with relapse

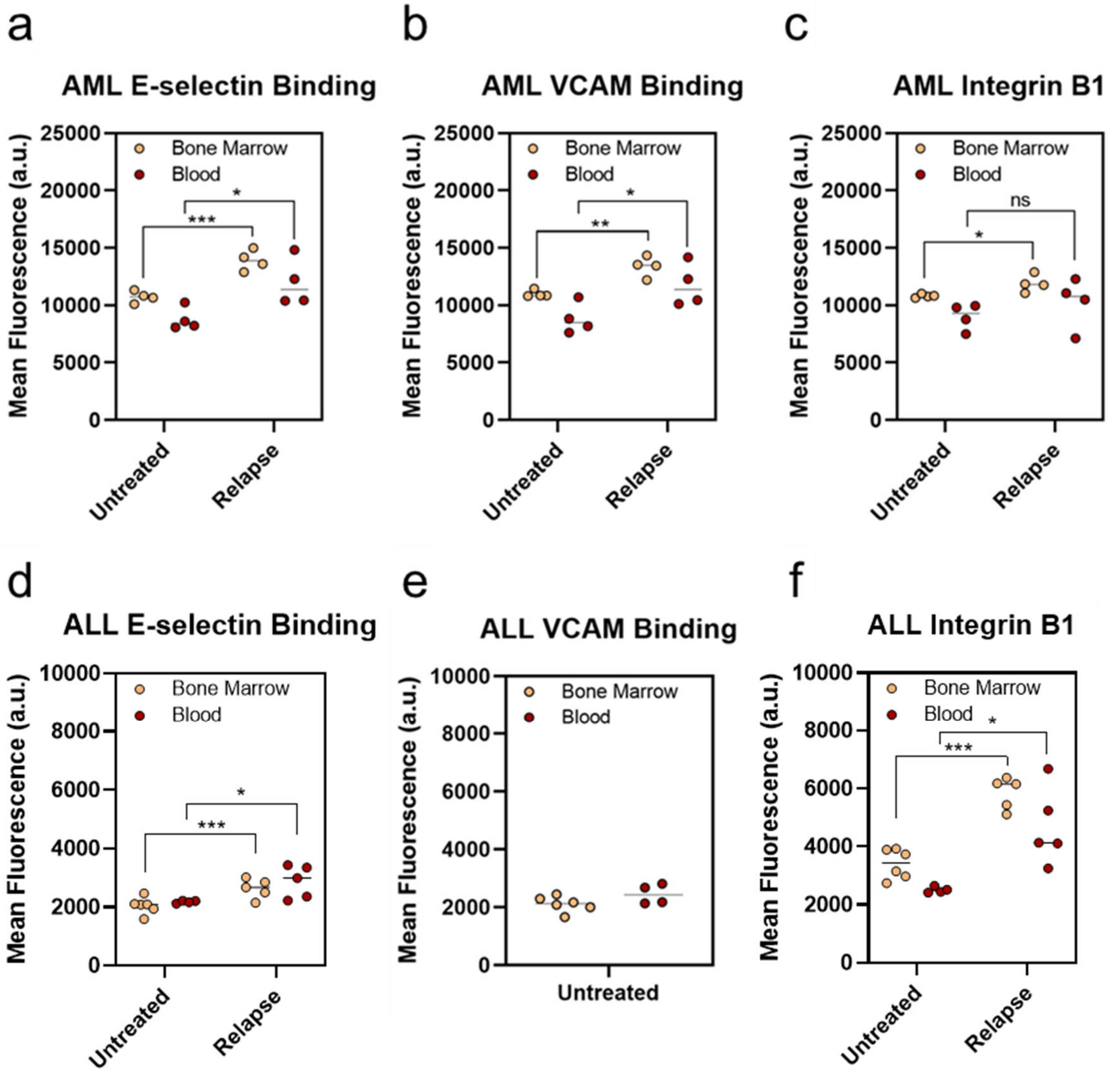

Figure 4.22 Expression of adhesion molecules in untreated and relapse leukemias. (a-c) Mean fluorescent intensity in AML model from flow cytometry of recombinant E-selectin (E-selectin Binding), recombinant VCAM1 (VCAM Binding), and integrin β1 antibody, show increases between untreated and relapse in both blood and bone marrow. (d-f) Mean intensity of ALL model with the same binding assays. Limitations in reagents prevented measurements of VCAM binding in relapse ALL. *p<0.05, **p<0.01, ***p<0.01. All p values are two-tailed t-tests.

leukemia cells in both blood and bone marrow showing significantly elevated levels of adhesion molecules.

Comparing these findings to that of mice shortly after treatment demonstrated that the binding capacity of both the AML and ALL cells increased acutely post treatment in the bone marrow and remained elevated throughout relapse (Figure 4.23). While other studies have

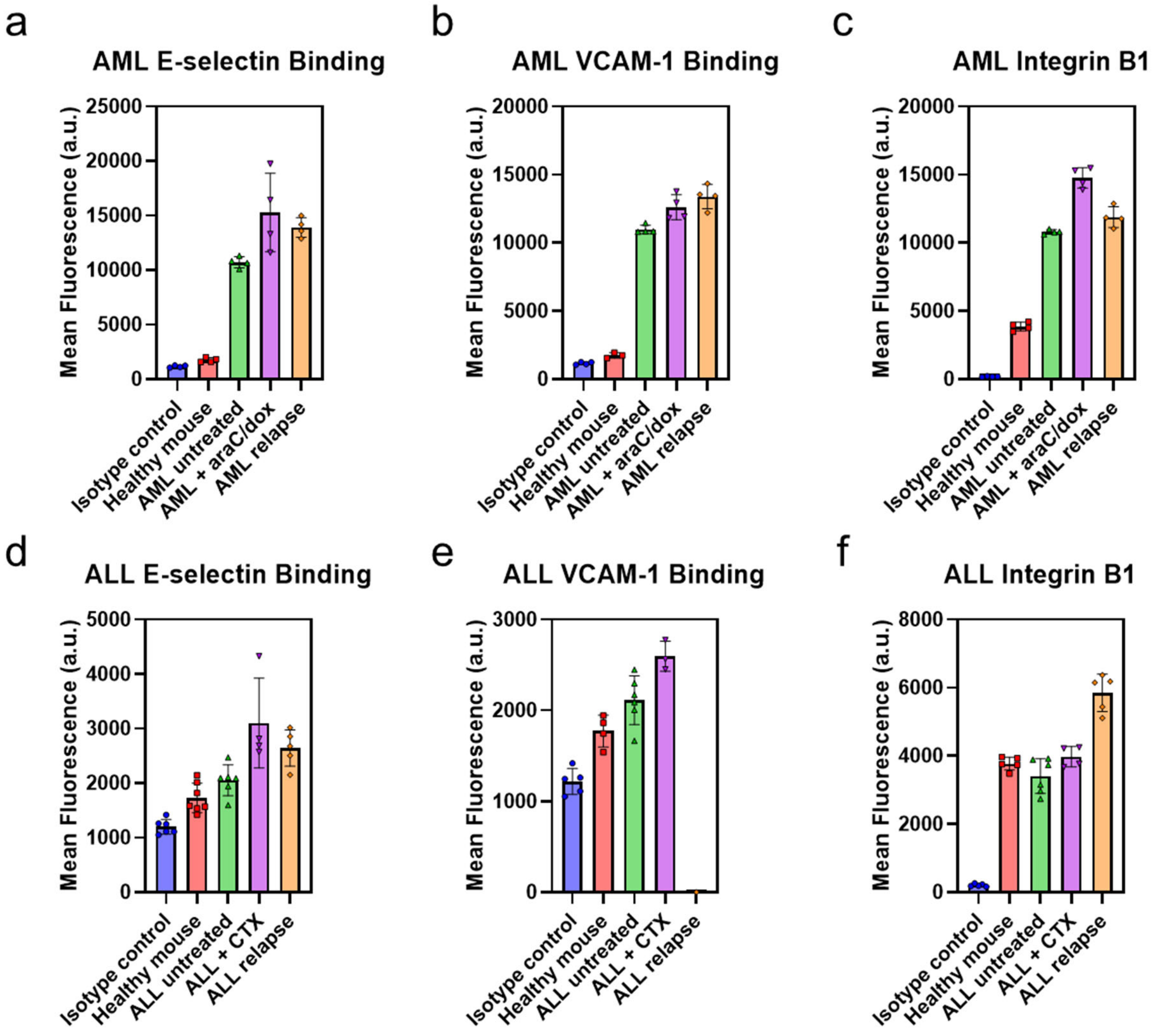

Figure 4.23 Adhesion molecules increase acutely and remain elevated after treatment in both AML (a-c) and ALL (d-f) models. AML untreated = D14 post initiation, AML + araC/dox = D2 post final treatment (D14 post initiation), AML relapse = D13 post final treatment, ALL = D10 post initiation, ALL + CTX = D2 post treatment, ALL relapse = D19 post treatment.

similarly shown increases in adhesion expression directly following chemotherapy, there has been little evidence of whether that expression remains increased during relapse[100].

While we see that expression of adhesion molecules in both the AML and ALL models increased from an untreated to relapse state, our blood exchange findings showed that only in AML was there a phenotypic change in clearance kinetics. However, when directly comparing the expression of adhesion molecules between the two models, an interesting observation emerges. For both E-selectin binding potential and integrin expression, the levels in the AML models are

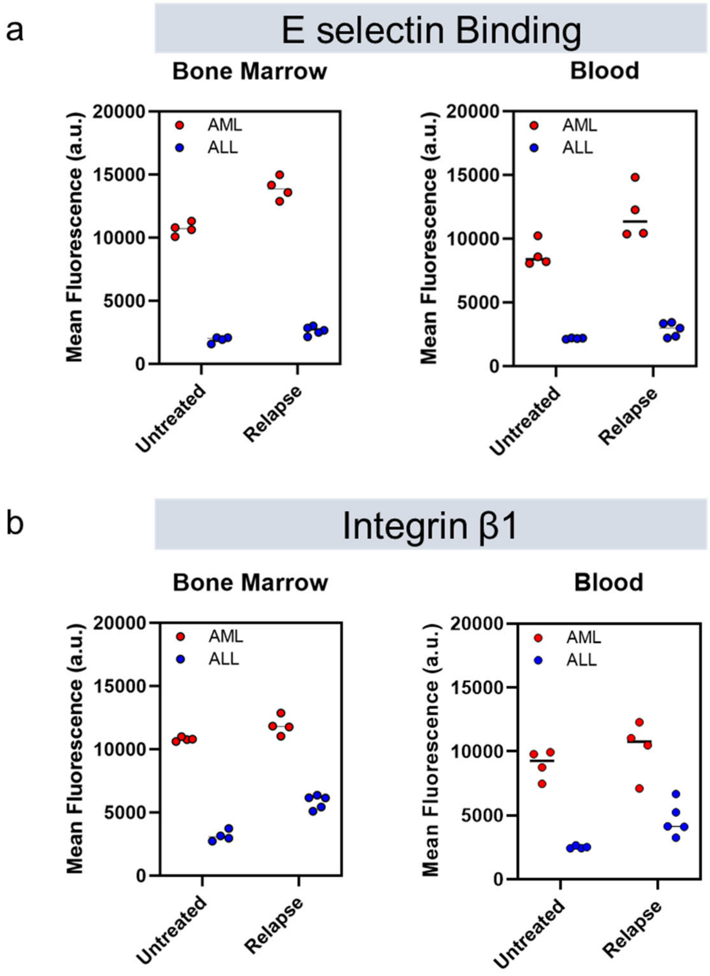

Figure 4.24 Comparison of binding expression between ALL and AML models. (a) E-selectin binding potential assayed through flow cytometry shows strikingly higher expression in AML compared to ALL in both blood and bone marrow. (b) Integrin β1 expression assayed through flow cytometry shows strikingly higher expression in AML compared to ALL in both blood and bone marrow

strikingly higher than in the ALL model (Figure 4.24). This difference in expression levels was also seen with untreated VCAM binding, though limitations in reagents prevented measuring the capacity of relapse ALL cells to bind VCAM. This could suggest that the slight increase in binding capacity observed in ALL is not sufficient to alter the clearance rates.

Because E-selectin inhibition on endothelial cells was sufficient to alter clearance kinetics in a diseased ALL mouse, we wanted to explore whether interfering with E-selectin binding of the AML leukemia cells could explain the observed changes associated with relapse

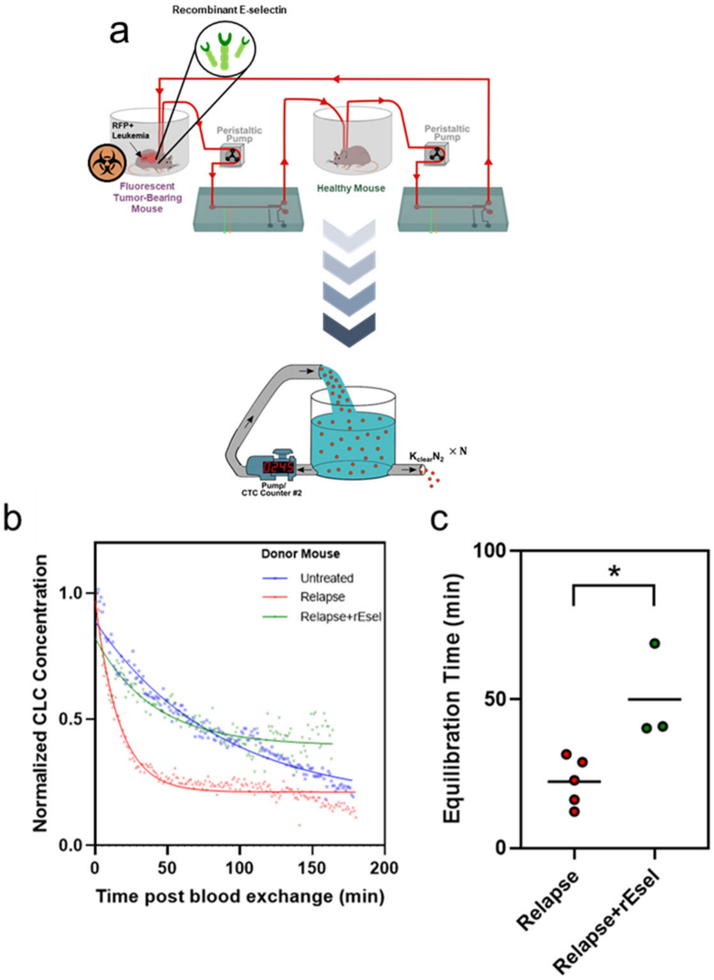

Figure 4.25 Blood exchange with recombinant E-selectin (a) Overview of experiment. AML relapse donor mice were injected with 20μg of recombinant E-selectin antibody 20 minutes prior to blood exchange. (b) Decay profiles of post-blood exchange scans show a shift from the relapse mice. (c) E-selectin treated mice (Relapse+rEsel) had increased equilibration time compared to the non-dosed relapse mice. (*p=0.017 with unpaired two-tailed t-test).

disease. To that end, we dosed relapse AML mice with 20μg of recombinant mouse E-selectin 20 minutes prior to blood exchange with a healthy recipient, as a way to bind up the glycoproteins on the leukemia cell surface (Figure 4.25a). We found that indeed, a difference in the decay kinetics was observed. Relapse mice dosed with recombinant E-selectin showed a significantly longer half-life than non-dosed relapse mice (Figure 4.25b-c). These results indicate that the increase in E-selectin binding molecules on AML relapse cells increases the ability of the relapse cells to exit circulation faster. Inhibiting E-selectin binding on the AML relapse cells prevents them from rapidly leaving circulation.

As a final check, we wanted to verify the metrics being measured, fraction remaining and equilibration time, are not directly correlated, but in fact independent variables. We compared the equilibration times and fractions remaining for ALL mice with varied recipient animals and found no correlation between the variables, indicating that these two metrics are independent (Figure 4.26).

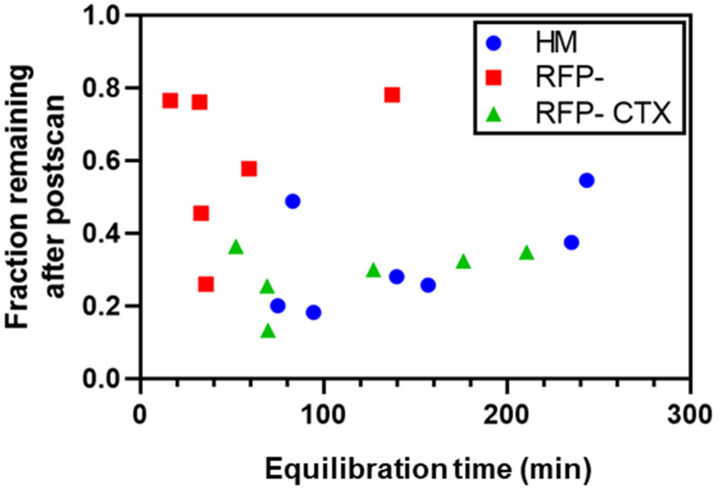

Figure 4.26 No correlation seen between Fraction Remaining and Equilibration time. $R^2 < 0.30$ and $p > 0.2$ for each linear regression

In this chapter, we applied the blood exchange method to two models of leukemia, a BCR-ABL driven ALL model and an MLL-AF9 driven AML model. We found that both of these models had longer circulation times compared to our previous measurements of solid tumor CTCs. Then, by varying the donor and recipient animals in blood exchange, we assessed the factors that contribute to changes in circulation kinetics.

In our ALL model, we found that presence of disease in the recipient animal transiently decreased the ability of circulating cells to extravasate, as seen by a higher fraction of donor cells remaining in circulation, and we showed that treating the mice to decrease tumor burden reversed the finding. We then sought to address what factors of disease presence contributed to the altered circulation kinetics. We demonstrated that hypocellularity alone, induced either through sublethal irradiation or chemotherapy, was insufficient to increase the extravasation of donor ALL cells. This suggested that a factor other than cellularity was responsible for governing clearance rates. We saw that expression of an endothelial adhesion protein, E-selectin, was upregulated in the presence of disease and downregulated after treatment, in correlation to the observations of blood exchange. And by blocking E-selectin through antibodies, we were able to increase extravasation in diseased recipient mice, demonstrating that E-selectin can modulate the clearance capacity of circulating leukemia cells. We suspect that high levels of E-selectin in a diseased mouse traps cells in the bone marrow and along the endothelial walls. By blocking E-selectin, leukemia cells are released from the bone marrow and vascular walls, allowing for leukemia cells to more freely mix between the compartments, leading to a higher turnover between the blood and marrow, which allows for more of the fluorescent cells from the donor mouse to exit circulation.

Next, we looked to assess the impact of changes in the tumor cells on clearance kinetics. We showed that disease burden did not impact clearance rates in either the ALL or AML model.

Then, we explored the differences in clearance rates between untreated and relapse disease. While we found no changes in the ALL model, our AML relapse disease cleared at a significantly faster rate. We assessed the biophysical properties in the AML untreated and relapse cells and found no significant difference, but we found that the expression of adhesion molecules increased after treatment and remained elevated throughout relapse, with AML expressing much higher levels of adhesion molecules than the ALL model. Finally, by blocking the capacity of AML cells to bind E-selectin, via dosing with recombinant E-selectin, we were able to slow the clearance rate of relapse AML disease.

These findings indicate the importance of adhesion molecules, and E-selectin in particular, at modulating the clearance rates of circulating leukemia cells. E-selectin has been explored as a potential therapeutic target for concurrent chemotherapy in AML[104], and the data we have shown here supports this and suggests that other types of leukemia, such as ALL, may also benefit from E-selectin based therapies. Our findings also show that adhesion proteins are important to consider in the relapse context, especially because the cells themselves can have a prolonged alteration in the expression of adhesion molecules, providing additional potential targeting factors for therapy.

5. Concurrent projects and conclusion

While the CTC counter platform has been used in the blood exchange method to study the circulation kinetics of tumor cells in the blood, there have been a number of other concurrent projects utilizing this system. These preliminary studies vary from new chip development to analysis tools to increase the capabilities of the system. First, we designed and tested a new chip to sort and purify single CTCs in real time directly from the bloodstream of mice within a single chip without off-chip manipulation or user input. Next, we developed a method to estimate the size of fluorescent objects as they pass through the laser lines, as well as a method to estimate the concentration of cells when they are so concentrated that multiple cells pass through the laser lines at once. Finally, we worked on a project aiming to understand how immune checkpoint blockade impacts tumor cells of responding and non-responding tumors, and what physical and transcriptional changes may be associated with each phenotype.

5.1 On-chip single-cell purification

One of the initial goals with the development of the CTC sorting system was to allow for the longitudinal sequencing of single CTCs sorted from the bloodstream of mice. While improvements in the sorting methods (described in Chapter 2) provided for a more efficient purification protocol, we wanted to determine whether further enhancements could be made to the system to allow for a more streamlined process to collect and purify CTCs.

To that end, we developed a new chip design based on the concept of multiple rounds of dilution-based purification (Figure 5.1). In this chip, blood from a tumor bearing animal enters the chip through the same peristaltic pump as in previous designs, and the same laser system is used to identify the fluorescent CTCs.

Once a CTC is detected, it is sorted in ~100nL using actuatable valves and flushed downstream on the chip with a flush buffer. The flush buffer acts in this case as a diluting agent, diluting out the other RNA-rich cells of the blood: red blood cells, platelets, and importantly, white

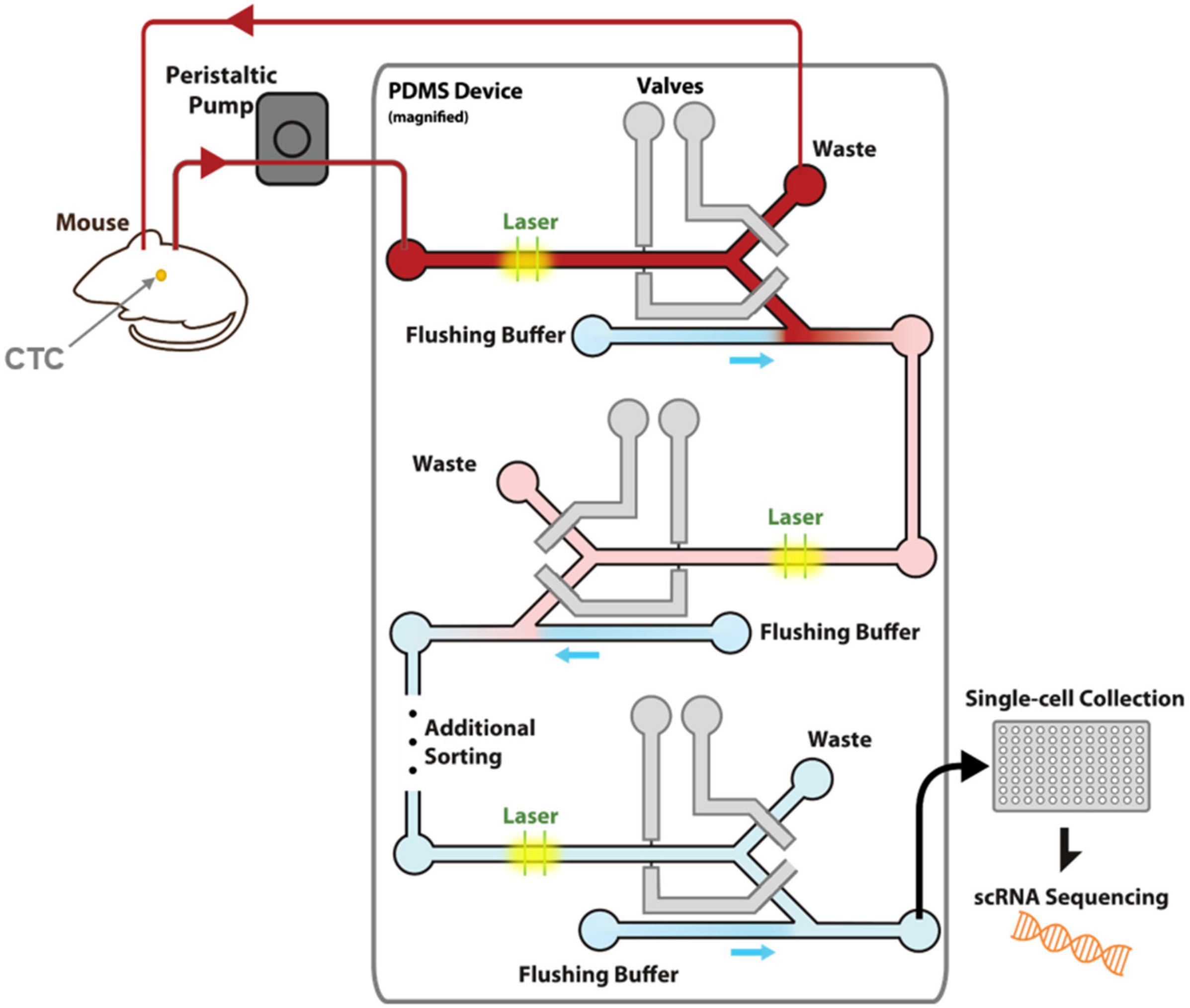

Figure 5.1 Schematic of single chip sequential sorter. In this design, blood from a mouse is drawn through peristaltic pump into the main inlet of the chip. Laser lines identify the fluorescent CTCs, allowing valves to actuate appropriately to divert the CTC in a small blood volume, while the remainder of blood is returned to the mouse through the venous catheter. The diverted blood is diluted using a flushing buffer, until it passes through the next set of laser lines, where the CTC is resorted and re-diluted. Additional sorting steps are performed until the CTC is at a single-cell resolution, where a sorting volume (~100nL) contains only a single cell. The final sorting of the CTC allows for the flushing buffer to push the CTC off-chip and into the well of a collection plate, where it can be sequenced.

blood cells. The diluted blood containing a CTC is then re-run through laser lines, and the CTC is sorted out in ~100nL of the diluted blood. This blood is then even further diluted in subsequent sorts, until the blood is so diluted that only 1 cell (the CTC) is present in a 100nL volume. At this point, the detected CTC is sorted and flushed off-chip into the well of a collection plate, where it can be lysed and processed for downstream single-cell RNA sequencing.

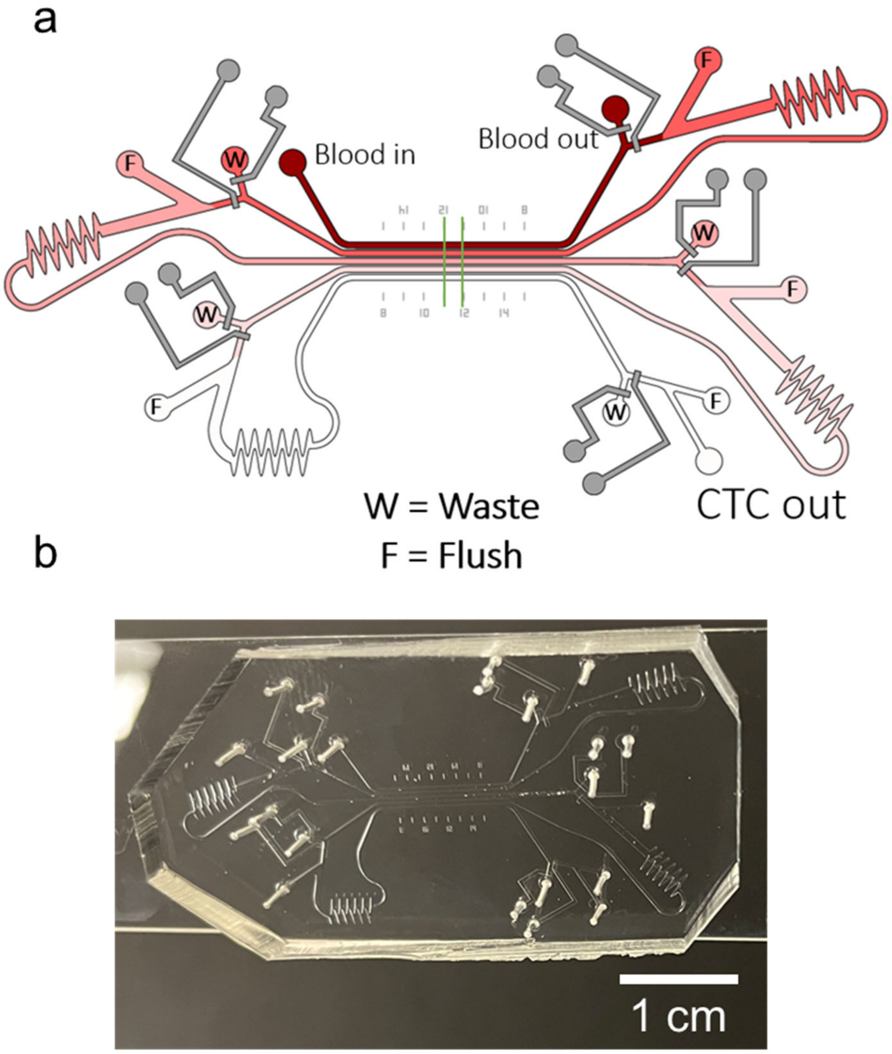

Figure 5.2 Chip design for sequential sorting chip. (a) Schematic of new chip. Color within the channels represents the dilution of blood as it passes through the chip, with dark red as whole blood directly from the mouse and white as the pure CTCs in flushing buffer. Valves are shown in gray. Laser lines are shows as green lines across the center of all 5 channels. (b) Fabricated PDMS device.

In the actual design of the chip, we decided to utilize a single extended set of laser lines to excite the fluorescent CTCs instead of splitting a laser line into multiple separate laser lines that would need to be independently aligned throughout the chip (Figure 5.2). We decided on a design that utilized 4 sequential sorting steps, for a total of 5 detection channels, as the final flush off-chip does not provide additional purification. In addition to the inlets, outlets, flush channels, and valves, zigzag shaped sections of channels were implemented after each flush port to induce mixing of the sorted blood at each step, allowing for more reliable purification through the dilution and sorting based chip.

To maximize the purity of the final product, we needed to maximize the dilution at each step of detection/sorting. However, the higher the dilution factor, the longer it would take to flow through the system, as additional flush buffer would need to be mixed in with the sorted blood. For example, doubling the dilution-fold at a single step from would take twice as long, so doubling each of the 4 steps would take 16 times longer. Running the system with around 20-fold dilution at each step can take around 1 minute, so running it with a 40-fold dilution could take more than 15 minutes per cell. To determine the optimal dilutions for our purposes, we calculated the estimated number of blood cells that would be present in the final sort of the chip depending on

4 series of sequential dilutions

Fold dilution at each step	Final # of cells sorted with 1 CTC		
	RBCs	WBCs	Platelets
10	80	0.1	10
20	5	.006	.63
30	1	.001	.12
40	.3	.0004	.04

Table 5-1 Estimated number of blood cells sorted (red blood cells, white blood cells, and platelets) if each of the four sequential dilutions have a given dilution fold. For example, to achieve only 1 RBC and no platelets or WBCs in the final sort, each dilution step would need to dilute the sample 30-fold.

the dilution at each step (Table 5-1). We determined that a dilution factor around 20 or higher at each of the 4 sorts would result in a product that contained on average, no WBCs and less than 1 platelet. To minimize red blood cell contamination, further diluting would be required, and purification above 30-fold at each step would result in a final product with less than 1 RBC per sort. Because WBCs contain the most contaminating RNA, even a 10-fold dilution at each step would sufficiently mitigate a significant source of non-CTC RNA, but we decided to aim for between 20- and 30-fold dilution at each step to minimize the contamination from RBCs and platelets as well, which can obscure the gene signatures of the CTCs.

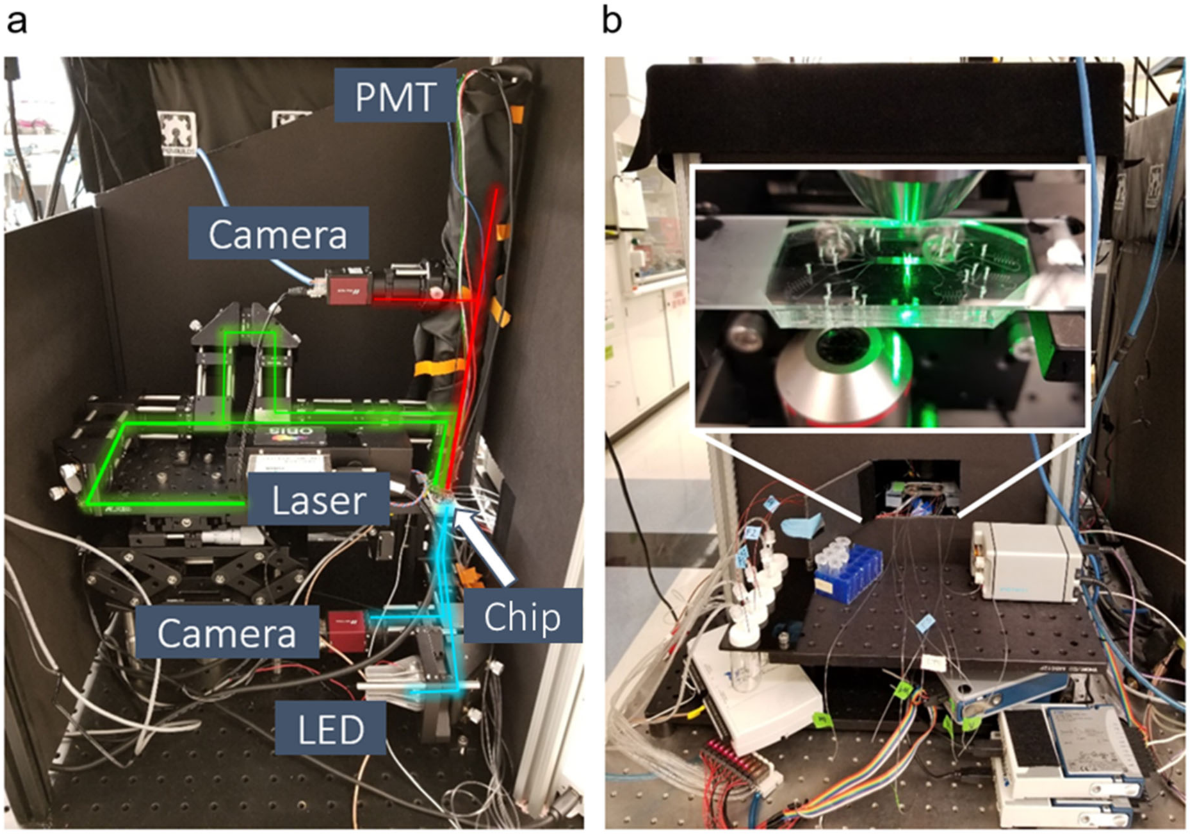

Figure 5.3 System for single-chip sequential sorter. (a) Optical train demonstrating the path of the laser lines as they are projected onto the chip (green), the emitted fluorescent light detected by PMT and camera (red), and the LED light used for brightfield imaging (blue). PDMS chip is identified with a white arrow. (b) Front view of the sorter system with inset showing an up-close view of the laser lines being projected across the 5 channels of the chip.

The design of the optical system followed a similar path as in the traditional CTC counter (Figure 5.3). The laser beam was split in two using a polarizing beam splitter, and the beam spots were projected onto the PDMS chip into lines using a cylindrical lens. The subsequent emitted fluorescent light was then directed to a PMT for fluorescent detection, as well as a camera to visualize the laser lines. A bottom optical train allowed for LED based illumination of the chip for brightfield imaging to monitor the blood flow throughout the chip.

In order to use the system, a modified version of the software control system was needed (Figure 5.4). The LabView project was built upon the system that was used for the CTC detection system, but with added logic controls to actuate the valves and flush channels appropriately. As there is only one PMT detector for the system, only one cell can be tracked through the system at any one time. Therefore, when a CTC is sorted into the downstream channels for the dilution-based purification, the upstream channels must stop scanning through the blood to detect new CTCs until the sorted CTC has fully made its way off-chip. Only then can the system state be reset, and the pump continue scanning through the blood of the mouse.

To do so, the channels and valves operate by the following logic: when the PMT first detects a cell, the valve to the outlet (return of blood back to mouse) is closed and the valve to sort (downstream for purification) is opened. The flushing buffer is turned on to begin dilution of the blood. In order for the CTC to be pushed through into the downstream system, the peristaltic pump must remain on but at a very low rate, in order to maintain a high dilution ratio with the flushing buffer. In this way, the downstream flushing buffer operates at a high pressure (high flow rate), while the upstream pump operates at a low flow rate. This allows for the CTC to be slowly pushed through the mixing region, increasing the degree of dilution of the blood. The system remains in this state until the CTC passes through the laser line in the second channel. At this point, the peristaltic pump is turned off and the valves are actuated such that the flush channel that was

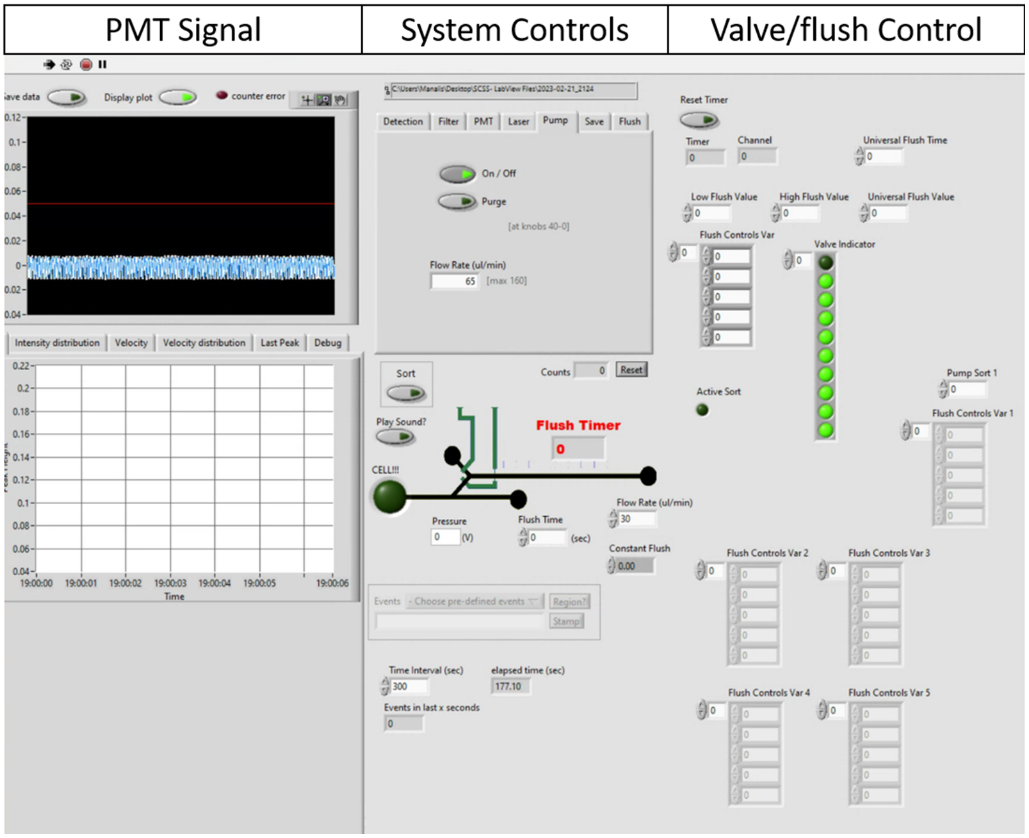

Figure 5.4 LabView display for single cell sequential sorting chip shows the three sections- a live readout of the fluorescent PMT signal and detected peaks; controls for the system including pump speed, laser, PMT gain, filtering specification, etc.; and a valve/flush controller showing the state of each valve and flush channel.

previously diluting the CTC now acts as the force pushing the cell through the system with a low pressure and low flow rate, while the next downstream flushing channel is activated at a high pressure to allow for increased dilution through the chip. Similar logic continues as the CTC progresses through the chip, with the PMT keeping track of which channel the fluorescent cell was last detected in and activating valves and flush channels appropriately. This continues until the CTC is detected in the final channel, where the last flush buffer fully pushes the cell off-chip by remaining on at a high level for several seconds to rapidly push the cell through tubing into the well of a collection plate. At this point, the system state returns back to the starting condition, with the peristaltic pump on and valves actuated to allow for blood to be returned to the mouse as it is scanned through the first channel of the chip, searching for the next CTC. A final condition of the code creates a scenario to fully flush the chip in case of a cell that is lost through the system. The user can set a maximum time to scan for the cell in a dilution step, and if this limit is reached, all flush channels will be activated and all waste channels will be opened, to fully flush the system and reset to the starting condition, where search for a new CTC begins.

The next step was to determine the ability of the new chip to detect fluorescent events. Because a cylindrical lens was used to project the laser beam spots into lines, it results in a gaussian projection, with a bulge in the center and less intensity at the edges. Because of this, when the lines are projected across the five channels of the chip, the top and bottom channels get less illumination, while the center channels have brighter intensity of the laser lines (Figure 5.5a). We looked to see the impact this had on the detection capabilities of the system. Additionally, since the area to cover

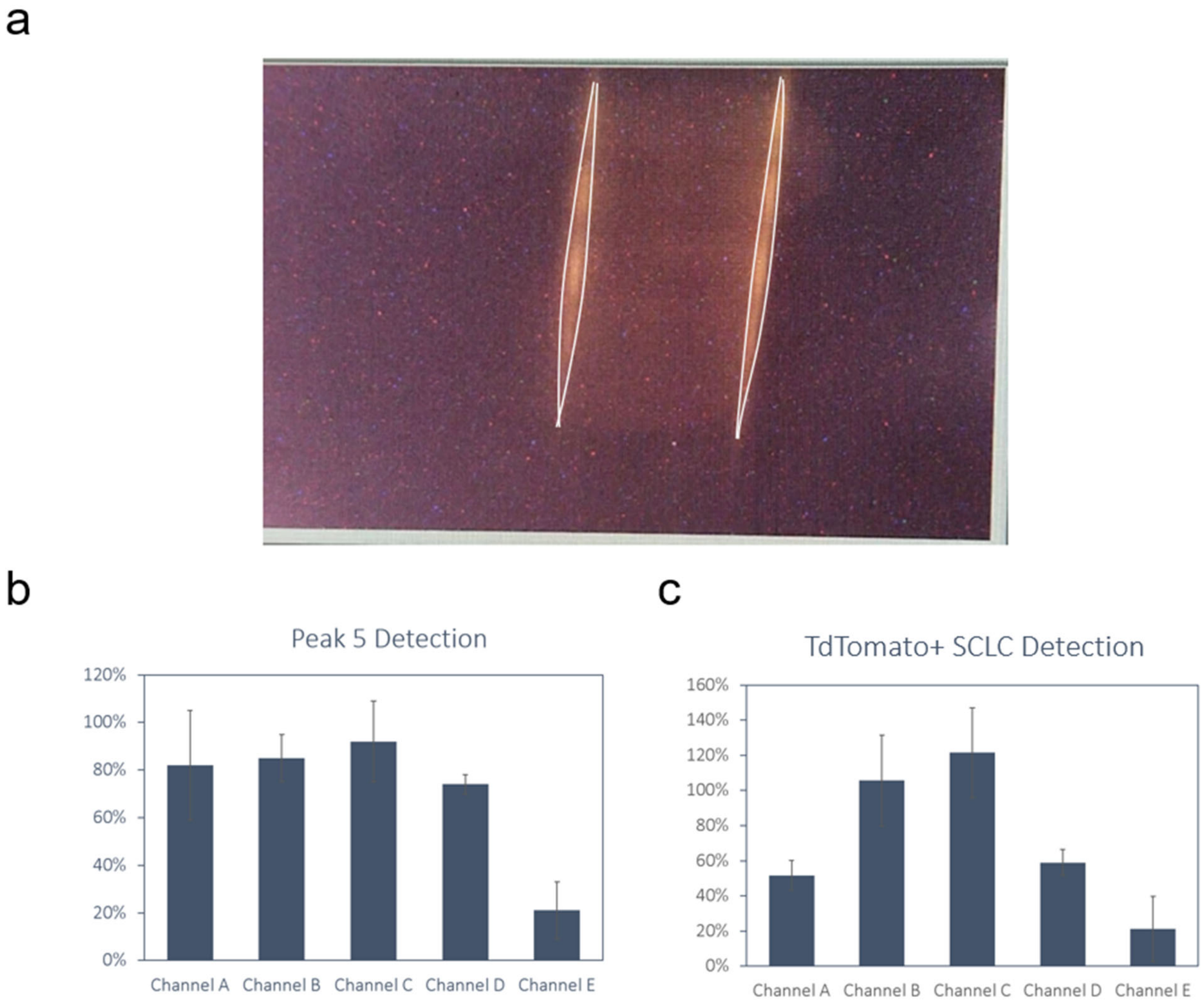

Figure 5.5 Detection of fluorescent events in the single-cell sequential sorting chip. (a) The laser lines pass through all 5 channels, as seen by the bright spots of fluorescent dye. However, a clear difference in laser line width/intensity is seen, as outlined in white. (b) Detection of bright Peak 5 flow cytometry calibration beads shows high percent detection in all by the final channel. (c) Detection of fluorescent cell line shows strong detection in the center channels, with lower percent detection in the first and final channels.

the 5 channels is significantly larger than the needs of a 1-channel system, a lower power objective was required. Rather than a 10x objective, we needed to use a 4x objective in order to fully visualize all 5 channels in the same field of view. As described in Chapter 4, decreasing the magnification power of the objective increases the amount of background signal, thereby decreasing the signal-to-noise ratio, which makes it more difficult to distinguish true fluorescent peaks from the background signal.

First, we used a set of fluorescent beads used for flow cytometry calibration. The brightest of these beads, Peak 5, was used to explore the detection capabilities of the new system. As expected, the final channel, Channel E, had significantly lower detection compared to the more central channels, detecting around 20% of the beads compared to over 70% in the other 4 channels (Figure 5.5b). And when running the fluorescent small cell lung cancer (SCLC) cell line, even more variation was seen within the channels. The central channels detected nearly 100% of the cells, while the first channel, Channel A, and the final two channels, Channels D and E, detected 60% or fewer (Figure 5.5c).

Next, we tested how changing the pressure ratios of neighboring flush channels resulted in a change in the dilution factor of the product (Figure 5.6). In the upstream channel, we flowed through the chip a concentrated fluorescent dye as a proxy for whole blood. In the downstream channel, we flushed water as a proxy for the flushing buffer. We collected 50uL of output for each condition and compared to the fluorescence of a dilution curve of the starting dye using a plate reader. We found two scenarios that increased the resulting dilution factor. First, by increasing the ratio of the pressures between the downstream and upstream channels, higher dilutions were achieved. This follows from the logic that adding additional diluent to a sample increases the dilution factor. We also saw that decreasing the average driving pressure while maintaining a given pressure ratio also increased the dilution factor. However, if the absolute pressures were too low

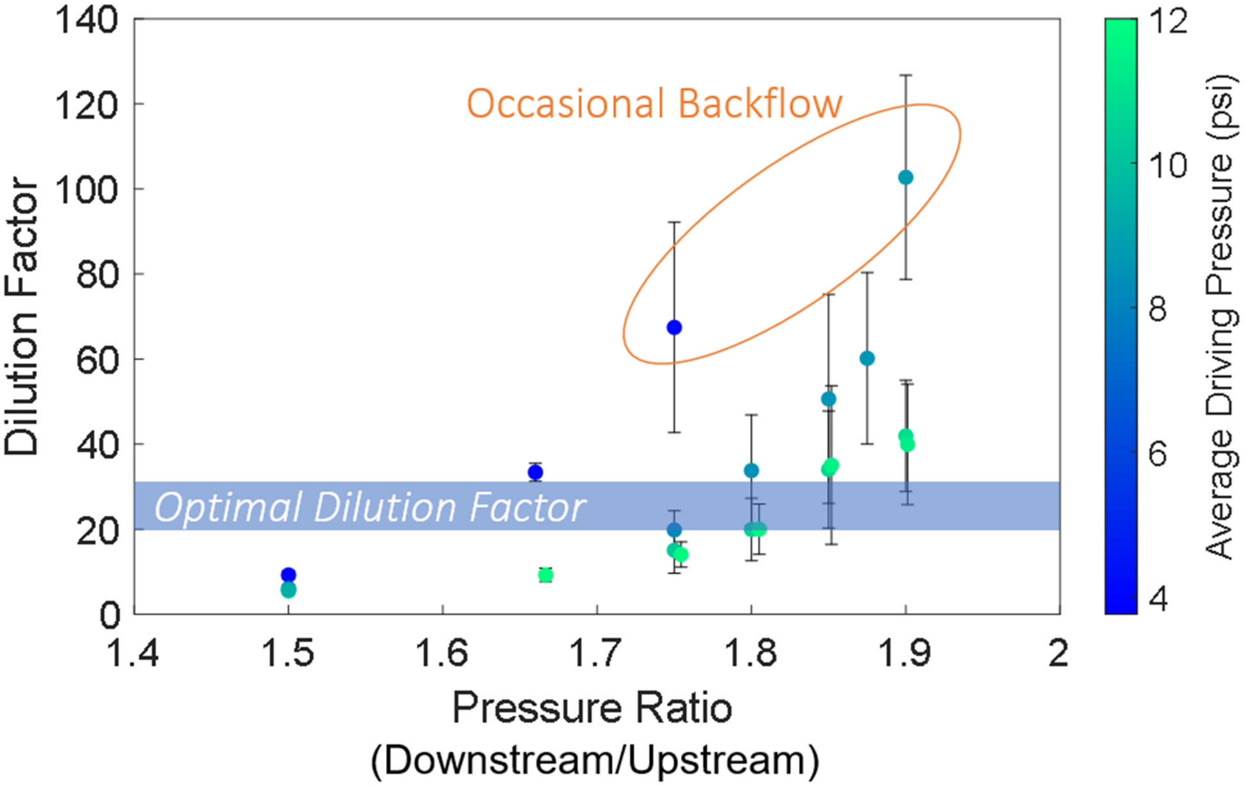

Figure 5.6 Impact of pressure ratios of downstream to upstream flushing channels on the dilution factors achieved. For conditions with very high dilution factors, backflow was occasionally seen, where the high downstream pressure prevented the lower upstream pressure from moving forward.

and the ratio of downstream to upstream was too high, we occasionally saw backflow in the channel, where instead of flowing down chip, dye would reverse directions and flow back towards the inlet of the dye. This is undesired, as backflow would confuse the PMT detection system as to which channel the cell is in or result in the CTC being flushed back into the tubing of the upstream flushing buffer. It was therefore important to select pressure ratios in our optimal dilution factor region, which allows for sufficient dilution without creating backflow in the system.

Finally, we performed an experiment testing the dilution efficacy of flow cytometry calibration beads spiked into blood. Peak 5 calibration beads were added to terminal mouse blood and flown through the chip. As the product flowed through the 5 channels, clear visual dilution was seen via brightfield imaging, with the highly concentrated dark blood getting diluted by the clear flush buffer (Figure 5.7a). Product was collected at the outlet of each channel, as well as from the whole blood inlet, and run through a Coulter Counter to determine the cell concentration. Dilution factors were estimated for each step by comparing the blood cell concentration of that channel outlet to the concentration of the previous channel outlet (Figure 5.7b). We found that, as expected, no strong change in cell concentration was seen between input blood and outlet of the blood before the first dilution. However, each of the dilution steps produced a marked increase in the dilution factor of the sample. The smallest dilution was seen in Dilution 1, with a <5-fold dilution factor. It is important to point out that this first dilution is the only one driven not by the pressure difference between two flush channels, but rather by the difference between a peristaltic pump and a pressure-driven flush channel, which gives less control over the dilution factor. However, the final 3 dilution steps all had greater than 15-fold dilution of the blood, with up to 250-fold dilution in one replicate of Dilution 2.

The cumulative dilution factor was also calculated for each experiment, with promising results. In one experiment, the final dilution factor was ~30,000 and in the other nearly 200,000. These cumulative dilutions correspond to an average of 13.1 and 21.1-fold dilutions at each step, respectively. These are right on the cusp of our desired dilution of 20 to 30- fold per step.

As of now, the biggest limitation of the system is with detection and recovery rate. With beads, our cumulative recover rate is below 25%, primarily due to the poor laser coverage of the

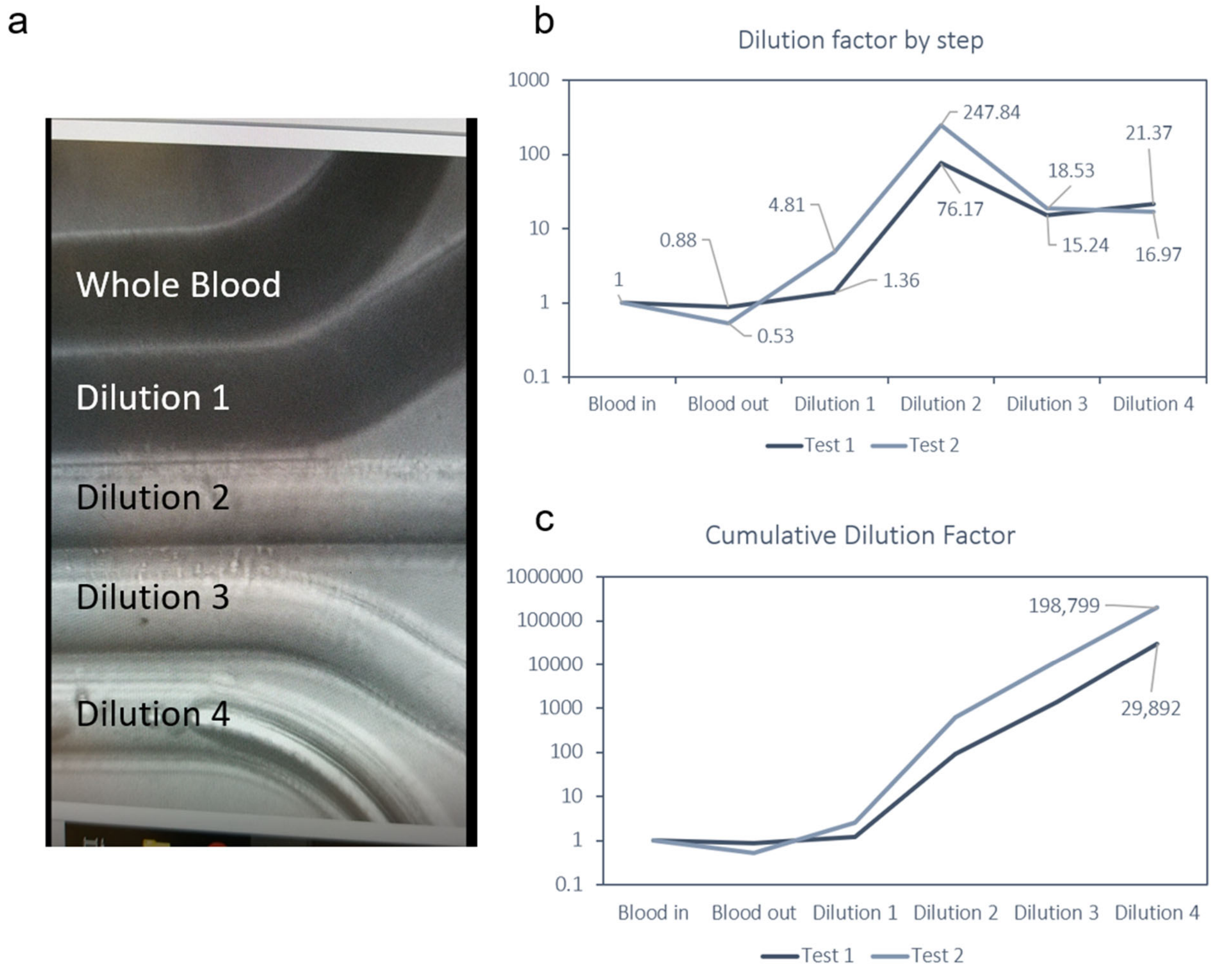

Figure 5.7 Dilution of fluorescent beads spiked into blood. (a) Brightfield image shows the dilution of blood through the single cell sequential sorting chip in the 5 channels. (b) Dilution factors at each step across two pilot tests show minimal difference in dilution between the blood inlet and outlet, but clear dilutions at each of the four dilution steps, with Dilution 1 having the least dilution factor of the four, and Dilution 2 having the highest dilution factor. (c) Cumulative dilution factors in two replicates shows strong levels of dilution throughout the chip, with nearly 30,000-fold dilution in one experiment and nearly 200,000-fold dilution in the other.

final channel. And with cells, our cumulative recovery rate is less than 10%, again due to the issues with laser coverage. Ideally, we would want the system to have a cumulative recovery rate >50%.

Several improvements will need to be made for the system to be fully functional. First, fully addressing the issue with laser line coverage of the channels could vastly improve the detection in the outside channels and the reliability of the system. This could be achieved using a fast-steering mirror, which could shift the laser lines to center around the subsequent channel once a cell is detected. Additionally, follow up experiments to quantify the dilution efficiency with cell lines spiked into blood and CTCs from tumor bearing animals is critical to assess the limitations of the platform. Also, a thorough testing of the recovery fraction of the various beads and cells will be necessary to understand where losses occur in the system.

Modifying the flush control could drastically improve the control of the dilution rates. Rather than using the current pressure-driven flow, volume-controlled flow could provide better control of the mixing and reduce the likelihood of backflow. Either syringe pump or peristaltic pumps could be used toward this goal.

The single-chip sequential sorting platform shows promise as a tool for sorting and purifying single fluorescent cells directly from the bloodstream of mice. This system could serve as an excellent method to capture CTCs longitudinally over the course of disease and treatment to understand how CTCs evolve at a transcriptional level. The system would allow for the sampling of blood of the same mouse at different timepoints, providing a drastic improvement to previous methods of euthanizing mice of the same cohort at different timepoints, leading to mouse-to-mouse heterogeneity. And by purifying cells immediately upon sorting, cells would not sit around in buffer for the duration of a CTC scan, as was historically done in our lab, preventing any *ex vivo* changes in transcriptional signature that can occur over the several hours between the first and final sort of CTCs. Instead, each cell would be immediately purified and lysed to maximally preserve the RNA signature of each CTC.

5.2 Size estimation from real-time measurements

One thing we have been interested in is utilizing the raw data from our CTC sorter system to extract additional information. Currently, the fluorescent data detected from the PMT is only used to determine either the presence or absence of a CTC to determine when a sort should occur, or to determine CTC concentration. However, the PMT data is a rich set of information that monitors the fluorescent intensity of the CTCs as they traverse the laser lines. Similar to how flow cytometry analyzes the peak and height information as cells pass by, we aimed to determine what additional features could be assessed using only the PMT data that we currently collect.

Biophysical properties of cells are crucial to their function. Because CTCs are non-blood cells that traverse through the vasculature, it would be interesting to get a better sense of their physical properties. Single CTCs can be 10-20μm in diameter, but are also known to form clusters or microemboli that can be 15-30μm in diameter or more, which can alter how they circulate in the bloodstream[125,156–158]. If our system could extract cell size from real-time scans of tumor bearing mice, we would be able to study how their properties change over time and how they respond to drug treatment. Therefore, we decided to explore whether we could extract CTC size as a parameter from the PMT data that we already collect.

To begin, we developed a mathematical model that would describe how the physical dimension of a single CTC would translate into our measured fluorescent data. As a fluorescent cell passes through the laser lines, it emits light beginning from the time it first enters the laser line until the moment it exits. TdTomato has a fluorescence lifetime of ~3 nanoseconds, much shorter than the PMT sample rate of ~33 microseconds[159]. Therefore, by measuring the width of the width of the fluorescent peak as a cell passes a laser line, we should be able to get a sense of the time a cell spends under the laser lines. However, the dwell time under a laser line is dependent on two parameters: the diameter of the particle and the speed at which it is traveling. A small particle moving very slowly can have the same dwell time as a larger particle moving very quickly. In a microfluidic channel with laminar flow, the velocity of a cell depends on the position within the channel, with cells near the walls passing slower and cells in the center moving faster, as is determined through Poiseuille flow[160]. Luckily, this can be easily addressed in our system, since we have two laser lines that each cell passes through. This allows us to accurately measure the velocity of each cell, and should thus enable us to calculate the diameter of the fluorescent cells. The equations that describe this model are as follows:

$$dwell\ time\ under\ laser\ line = \frac{d+\delta}{v} = \frac{W}{sampling\ rate} \tag{5-1}$$

The dwell time can be described physically by the diameter of the CTC (d - µm), the width of the laser line (δ - µm), and the velocity of the cell (v - µm/sec). The same dwell time can also be calculated in terms of the PMT data by the width of the fluorescent peak (W- number of datapoints) and the sampling rate (datapoints/second) (Figure 5.8).

$$v = \frac{D}{time} = \frac{D \times sampling\ rate}{S} \qquad (5\text{-}2)$$

The velocity of the cell can be described by the distance between the laser lines (D - µm) and the time it between the detection of the two fluorescent peaks, which can be described in the data space as a ratio of the sampling rate (datapoints/second) and the separation between fluorescent peaks (S - number of datapoints). Substituting velocity from Equation 5-1 with Equation 5-2 yields the equation:

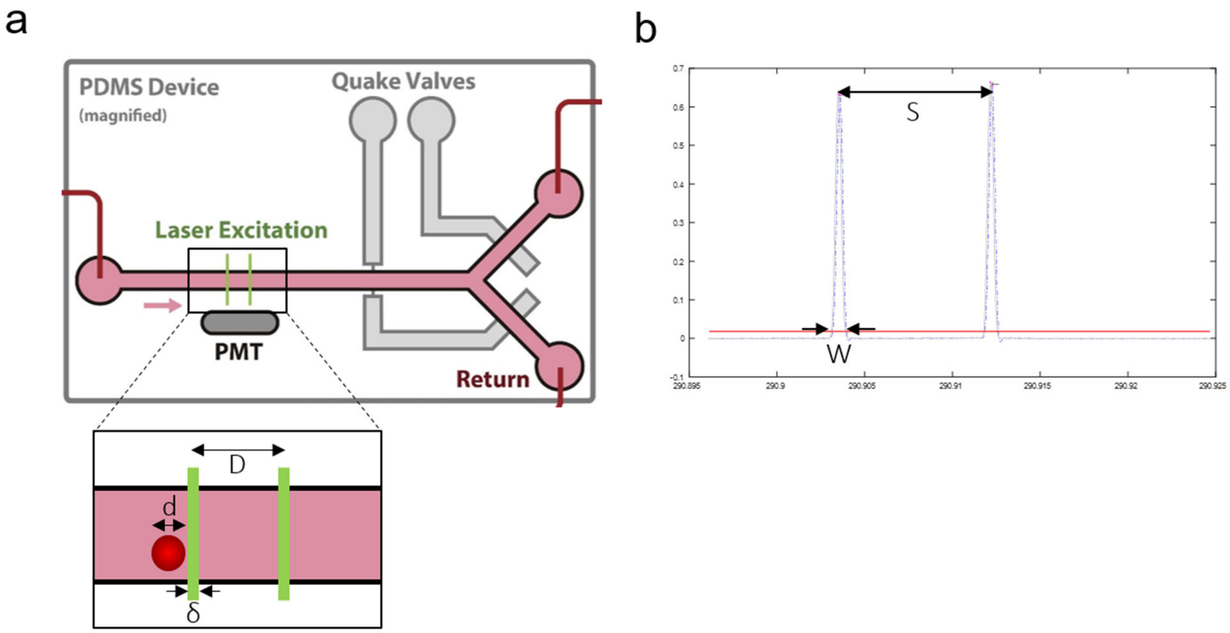

Figure 5.8 Schematic showing the parameters that are used to extract cell diameter from the fluorescent data. (a) Physical measurements on the chip are diameter of the CTC (d - µm), the thickness of the laser lines (δ - µm), and the distance between the laser lines (D - µm). (b) Measurements extracted from the fluorescent dataset include the width of the fluorescent peak (W – number of datapoints), and the spacing between the two peaks (S – number of datapoints)

$$\frac{d+\delta}{D\times sampling\ rate/_{S}} = \frac{W}{sampling\ rate} \tag{5-3}$$

And solving for d, the diameter of the CTC, gives us our final equation:

$$d = \frac{D\times W}{S} - \delta \tag{5-4}$$

This final equation relies solely on physically measurable variables that remain constant throughout the experiment, laser line separation (D – 300μm) and laser line width (δ – 20μm), as well as data from the PMT fluorescent signature that defines each fluorescent cell, average width of laser peaks (W) and peak spacing (S).

To begin testing the accuracy of the model, we used a set of fluorescent beads that come in defined sizes of 10, 15, and 19μm. We flowed these beads through the CTC detection system at a variety of flow rates and plotted their average peak width vs peak spacing (Figure 5.9). As seen in Equation (5-4), these variables should be linearly correlated for beads of a given diameter and should have an increasing slope as the diameter of the beads increases.

When the beads of varied width were run on the system at low flow rates, we indeed saw a clear separation between diameters as expected (Figure 5.9a-b). However, at high flow rates, the data began to overlap for the different bead sizes (Figure 5.9c-e). This is explained by a limit of sampling rate for the system. At high flow rate, an insufficient number of datapoints were above the detection threshold. With only 1 or 2 datapoints above threshold per peak, the average peak width variable (W) was unable to accurately distinguish between beads of different sizes.

Because the studies flowing the beads at low flow rates showed significant separation, we compared the recorded fluorescent data to the predicted values from the model. Since the beads can travel through the channel at a variety of linear velocities (based on Poiseuille flow), the model

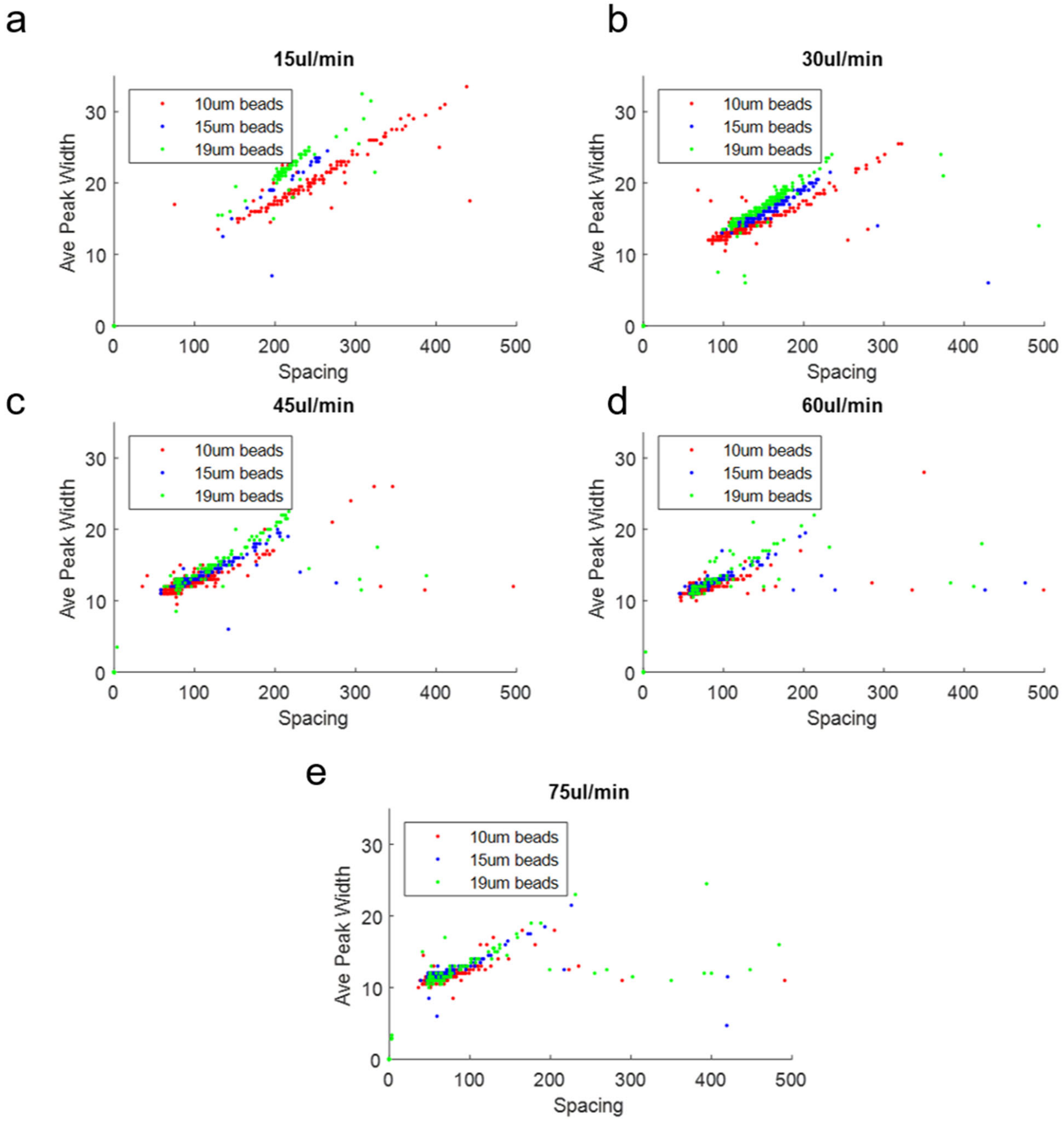

Figure 5.9 Detecting beads of defined sizes at different flow rates. Average peak width and spacing of peaks for 10, 15, 19µm fluorescent beads were measured from samples run at 15 (a), 30 (b), 45 (c), 60 (d), and 75 (e) µL/min.

describes the line of values that that beads of a certain size are expected to fall on. There was a strong correlation between the detected beads run at 30µL/min and the lines that the model predicted, indicating the promise of the system to identify cells of specific sizes (Figure 5.10).

To test the capability of detecting cells of different size, rather than fluorescent beads, the TdTomato+ SCLC cell line was use. Since the cells grow with variable diameters, a ground truth was needed to compare the sizes of the cells. To that end, we utilized a drug called barasertib, with is an Aurora B kinase inhibitor. The addition of barasertib to cell culture media allows cells to continue growing, but prevents the cytokinesis step of mitosis, such that cells cannot divide their membranes. By culturing in barasertib, cells will continue to double in volume and mass without creating daughter cells, providing an excellent tool for us to study the accuracy of our size detection method.

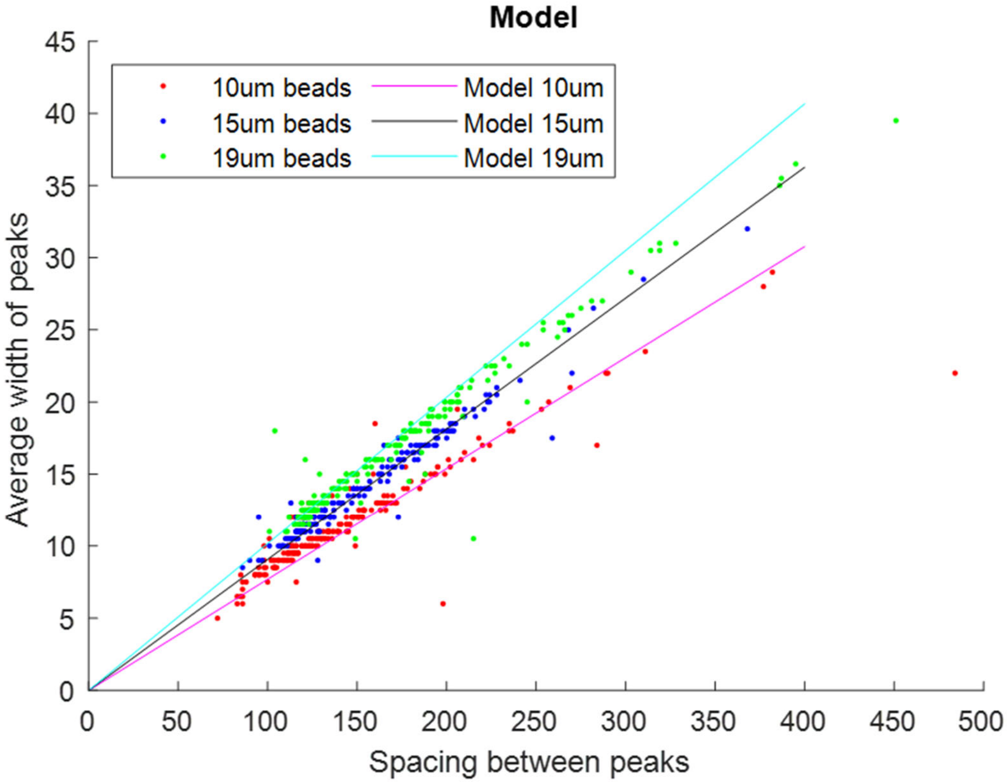

Figure 5.10 Comparison of bead sizing estimation to the predicted model shows strong correlation at 30µL/min

Barasertib treated cells showed a significant increase in size after 24 hours of treatment at a concentration of 5µM, as measured by Coulter Counter (Figure 5.11a). The cells with low diameter (<8µm) represent dead and dying cells, which quickly lose their fluorescence and would not be detected on the CTC Counter system. The same populations were run through the CTC Counter, and estimates of the cell size (determined by the slope of the peak spacing and average peak width), showed a distinct right-shift in the treated cells, as was seen in the Coulter Counter measurements (Figure 5.11b). There is certainly room for improvement in the estimation of the measurements, but these results clearly show the potential of utilizing the fluorescent peak signature to identify changes in volume of cell populations.

The previous experiments were performed using post-processing of fluorescent data in Matlab to identify the peaks and measure the corresponding peak widths and spacing distances. However, we next wanted to test whether or not the system would be able to separate out cells of different sizes in real time. As discussed previously, CTCs are known to exist either as single cells or as clusters in the blood, with clusters being implicated as more aggressive and more likely to

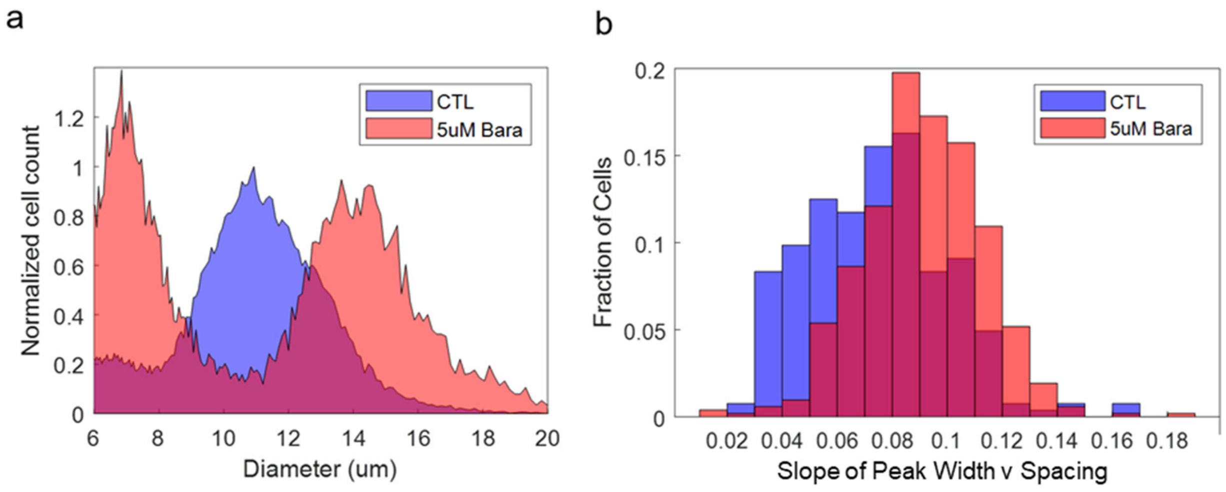

Figure 5.11 Size detection with barasertib treated cells. (a) Coulter counter measurement shows ground truth of cell size measurements in control cells (CTL) or those treated with 5µM barasertib (Bara). (b) Size estimation using the slope of peak spacing and width correctly shows a rightward shift in barasertib treated cells.

seed a distant metastasis. As such, developing a technique to distinguish clusters from single CTCs in real time could be used with the blood exchange method to send only CTCs of certain sizes, and sorting out other sizes, to directly test their metastatic propensities. Such techniques would need to rely on real-time analysis of peak information. To test this, we ran beads of two sizes through the system, and used Labview to plot the measured spacing and peak width in real time (Figure 5.12). The data from the measured fluorescent peak signatures were able to identify the 10µm beads with 90.4% accuracy, and the 19µm beads with 96.0% accuracy, validating the use of this method to distinguish between large and small fluorescent objects in real time.

In the future, further improvements can be made to this size detection method. Increasing the sampling rate of the PMT by optimizing the computer processing within the LabView code would allow for more datapoints to be collected per peak, giving more accurate estimations of the peak width and heights, as well as the duration of time between the peaks. Similarly, as described

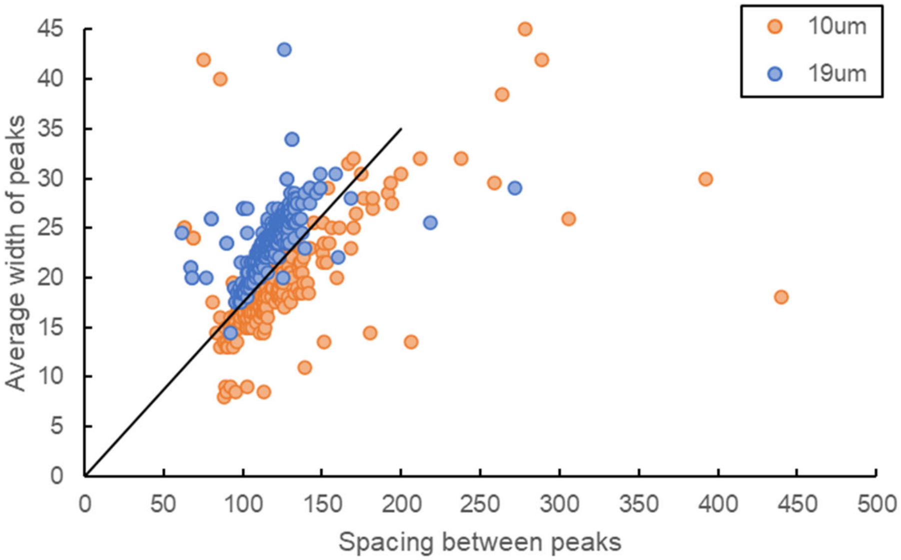

Figure 5.12 Real time size estimations in Labview. 10 and 19µm beads were run through the system, and a linear cutoff was able to distinguish 10µm beads at 90.4% accuracy and 19µm beads at 96.0% accuracy.

above, flowing the cells at a slower speed should increase the ability of the system to distinguish between sizes, by generating more datapoints per peak. Additionally, increasing the magnification of the microscope objective could lower the background signal, decreasing the threshold required to identify a peak and resulting in a more accurate peak width estimation.

Having the capacity to determine the size of fluorescent CTCs in the blood using the already recorded fluorescent data would be a strong advancement in the capabilities of the CTC sorter system. Such a technique would allow us to study whether CTCs change in their biophysical properties over the course of disease and treatment without taking the cells from the blood. Since there are so few CTCs in solid tumor models, it is infeasible to collect cells and measure *ex vivo* from the same animal longitudinally, so a system that can measure whole blood in line without diluting would be the only way to monitor changes in CTC size over time. Additionally, the sorting capacity of our CTC sorter coupled with the CTC size detection system would allow for the study of the impact of CTC size on the propensity to form metastatic nodules. CTCs of certain sizes could be sorted out of the blood in real time, and only the cells of a desired size range would be infused into a recipient naïve animal. Then, tumor outgrowth could be monitored in the recipient to see whether certain size ranges of CTC are particularly effective at seeding metastases.

5.3 High concentration estimation

One limitation in using the CTC sorter system to track the real-time concentration of fluorescent cells in the blood is that the nature of the detection method limits the maximum concentration that can be measured. Our current method identifies a two-peak signature in the fluorescence data that occur as a cell passes through the laser lines. Each cell produces the distinct fluorescent profile, and by counting the total number of cells traversing the lasers, we can determine the concentration. However, this method relies on the assumption that only a single cell passes through the laser lines at any given time. In the solid tumor models, CTCs are present at concentrations around 1000/mL (1/µL) or lower. However, in the leukemia models, CLCs can be found at concentrations up to 10,000,000/mL (10k/µL). As such, it is important to understand what the maximum detection rate of the system is and pursue new techniques to expand the limits of detection.

The maximum concentration that can be calculated through matched peaks requires each cell to pass through both laser lines before another cell enters the first line. This method was used for cell sorting and for the size detection application described above. In our solid tumor setup, the laser lines are 300µm apart, and with a channel width of 300µm and height of 50µm, the total volume per cell can be no more than 300 x 300 x 50 = 4.5M µm^3, or 0.0045µL. This comes out to 222 CTCs/µL, though assuming a Poisson distribution of cell spacing, any higher than ~100 CTCs/µL would likely result in overlapping signals, and thus, a misrepresentation of the concentration.

However, if size estimation and sorting is not needed, matched peaks is not essential, so one laser line could be used instead of two. Therefore, the minimum volume per cell required to estimate concentration using a single-cell approach would be the total volume covered by one laser line, which is the sum of the width of a cell and the width of the laser line. Since the width of a laser line is ~20µm and the width of a cell is ~10µm, the volume per cell could be no higher than (20+10) x 300 x 50 = 450k µm^3, or .00045 µL. This would mean that cells could be at a concentration of 2.2k CTCs/µL, though again, at any concentration about ~1k/µL, overlap would likely occur given a Poisson distribution.

However, since the high concentrations of fluorescent cells in the blood is typically seen more frequently in the leukemia models, it is important to estimate these values for the chip design used for the leukemia studies, with a thinner channel. In this system, the channel width is 100µm, so the minimum volume per cell to have one cell under the laser line is (20+10) x 100 x 50 = 150k µm^3, or .00015 µL, which comes out to 6.6k CLC/µL, so any concentration about ~3k/µL will likely create overlap.

To understand how different cell concentrations impact the ability to detect high concentrations of fluorescent cells, the RFP+ ALL leukemia cell line was run through the detection system at concentrations ranging from 200 to 50k/µL. A small segment (0.05 seconds) is shown in Figure 5.13, demonstrating that especially at high concentrations, significant overlap in fluorescent peaks is observed.

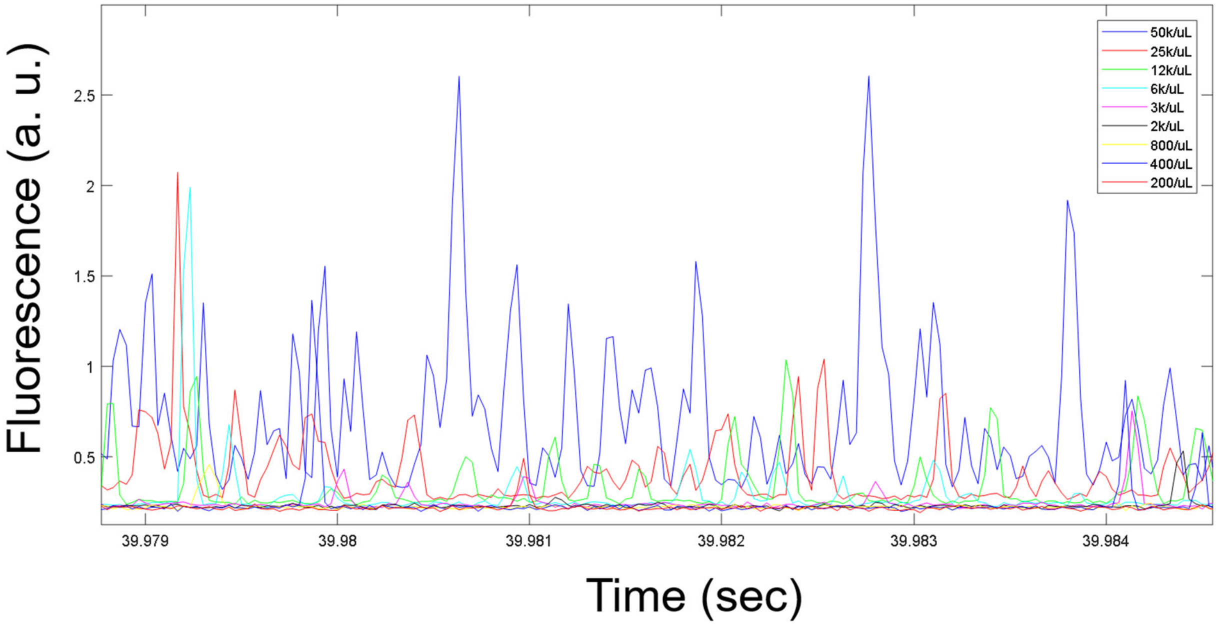

Figure 5.13 Fluorescent signal of RFP+ ALL cell line at various concentrations demonstrates the overlapping signature that appears at high concentrations.

The overlapping signatures result in significant added noise in the fluorescent signal. Therefore, we looked to see how to quantify the added noise as a way to estimate the cell concentration. The higher the concentration, the more overlapping peaks, and the more noise that should be seen in the signal.

We decided to look at the root-mean-squared (RMS) of our signature. RMS is calculated by squaring the full dataset centered around zero (to make all value positive), taking the mean, and then taking the square root. This value is similar to standard deviation and describes the variance of the signal. We calculated the rolling RMS in 1000 datapoint chunks for each of the concentration tested (Figure 5.14). We found that the RMS increased with increasing concentrations of cells, as expected. While some variation across time in RMS was seen, particularly at the highest

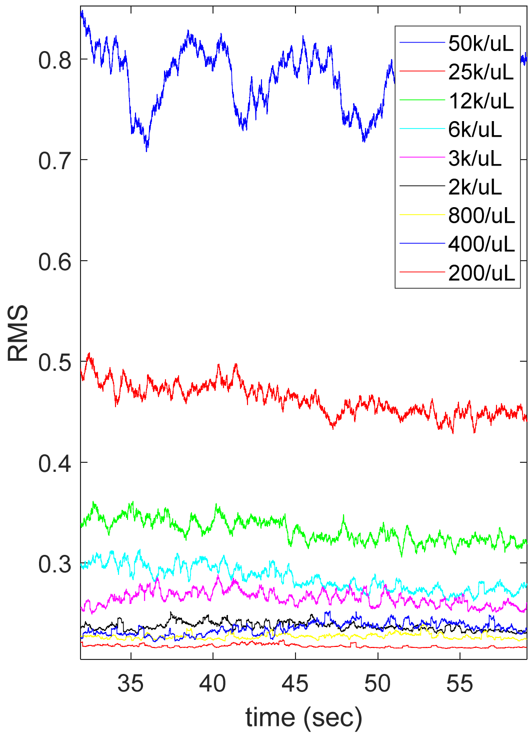

Figure 5.14 RMS of signal from RFP+ ALL cell line at various concentrations in the CTC sorter system. Clear correlation is seen between the RMS and the concentration of the cells.

concentration of 50k/µL, most of the other concentrations showed little variation in the RMS over the course of the study.

Next, we looked to see the correlation between RMS and the concentration of cells. We plotted the average and standard deviation of the RMS as calculated from taking 1000 datapoint chunks and fit to a linear regression (Figure 5.15a). We found an incredibly strong correlation between the two, indicating the power of using RMS to estimate the concentration of high numbers of cells in the blood.

However, upon closer look, we found that the correlation between RMS and concentration broke down at lower concentrations. At concentrations below 3000 cells/µL, there was a much poorer correlation between RMS and cell concentration. This matches up nicely to the estimated limit of single-cell detection. When no overlap in fluorescent peaks is present, as calculated for this system setup for concentrations <3000/µL, there should be only single peak events followed

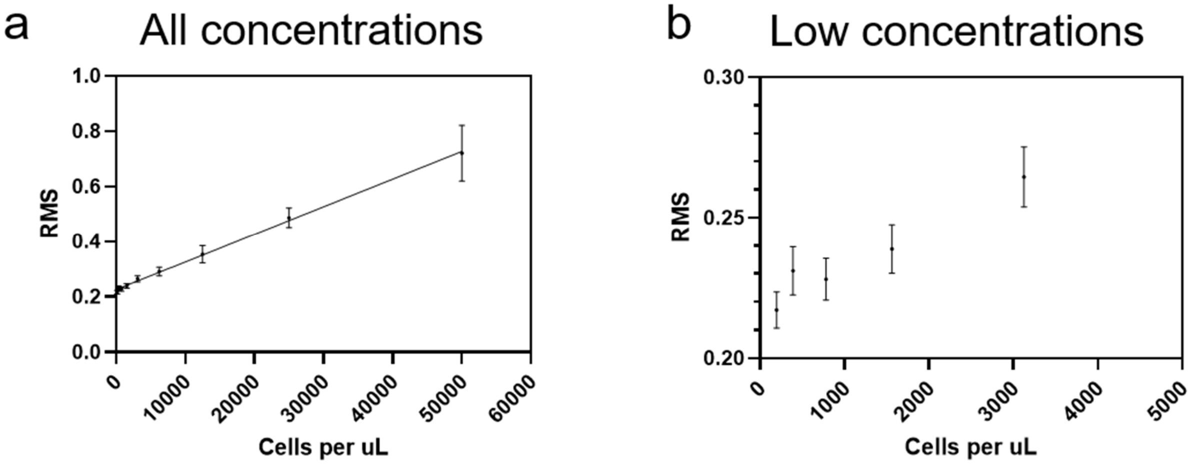

Figure 5.15 RMS as a metric to estimate high concentrations of cells. (a) RMS of fluorescent signal shows strong linear correlation to the number of cells per µL. R^2=0.998, p<0.0001 (b) At low concentrations, especially below 3000 cells/µL, there is much higher error of signal, such that it would be difficult to effectively distinguish between similar concentrations of cells.

by the background noise signal. This would correspond to very little added variance to the signal, and thus, the RMS does not significantly change.

The method of using RMS to estimate cell concentration showed major promise at high concentrations of cells, where fluorescent peaks of neighboring cells overlap into a noisy signal. However, at lower concentrations, the method of single-peak detection remained the most effective method for determining concentration, especially since it measured the true instantaneous concentration, rather than an approximation.

Additional experiments are needed to verify the potential of the RMS high concentration estimation. Testing on multiple chips will determine the chip-to-chip variation in background signal. This will determine whether calibration will be required for every new chip, or if a standardized linear regression will suffice. Additionally, the above experiments were performed with saline as a medium. It will be important to determine the impact of blood on the RMS, as well as the variation in background signal of blood in different animals. The experiments will also need to be performed on both of the leukemia models, to understand how the RMS varies with different cell lines. The more generalizable the linear regression, the more utility the method will have to estimate the concentrations.

Finally, a thorough characterization of the regime of single-cell detection versus the population-based RMS detection will be essential to determine whether there is a range of concentrations at which neither method is particularly effective at estimating the concentration, or whether the two methods have an overlapping region of concentrations, such that any physiological concentration of CLCs in the blood could be estimated by one of the methods.

5.4 Checkpoint blockade in mouse models

A side project looked to study the effects of immunotherapy on tumor growth, and specifically, why there is heterogeneity in response to immune checkpoint blockade (ICB). In order to avoid attack from the immune system, many tumors develop mechanisms to avoid immune detection. One of the most well studied method is the use of modulating immune checkpoint expression. T-cells express a number of proteins, including PD1 and CTLA4, that, when bound, act to mitigate a killing effect of the immune system. This helps prevent T-cells from killing normal cells. However, many cancers evolve to express proteins that bind strongly to these checkpoints, allowing the tumor cells to evade the immune system and grow without regulation. The expression of PDL1 on tumor cells binds to PD1, and the protein B7 can be expressed to bind CTLA4.

New cancer therapies have been developed that interfere with this signaling pathway, allowing the T-cells to do their job and efficiently kill tumor cells. These are ICB therapies, and are often antibodies for either PD1 or CTLA4. ICB treatments can be incredibly effective, curing even metastatic disease in many patients[72,75–77]. However, these therapies are not universally successful. While they can be curative in a subset of patients, usually only a fraction of patients effectively respond to these immunotherapies. As such, it is crucial to understand why there is a heterogeneity in response, and whether there are means of predicting response or determining why certain patients have better outcomes than others.

To study this question, we chose a syngeneic mouse model of breast cancer using an orthotopic injection of a cell line, E0771, into the mammary fat pad. The line is from a C57BL/6 background, and is EGFR+, Erα+, and importantly for the study of immunotherapy, PDL1+[161]. We began by initiating disease in C57BL/6 mice with injections of 500k cells. We followed the tumors over the course of several weeks and treated a subset with 12mg/kg of αPD1 immunotherapy at three timepoints, on days 11, 14, and 17 (Figure 5.16). Interestingly, we saw that the treated mice fell into two categories: those that had similar growth kinetics to untreated mice (non-responders) and those that showed minimal tumor growth upon treatment (responders).

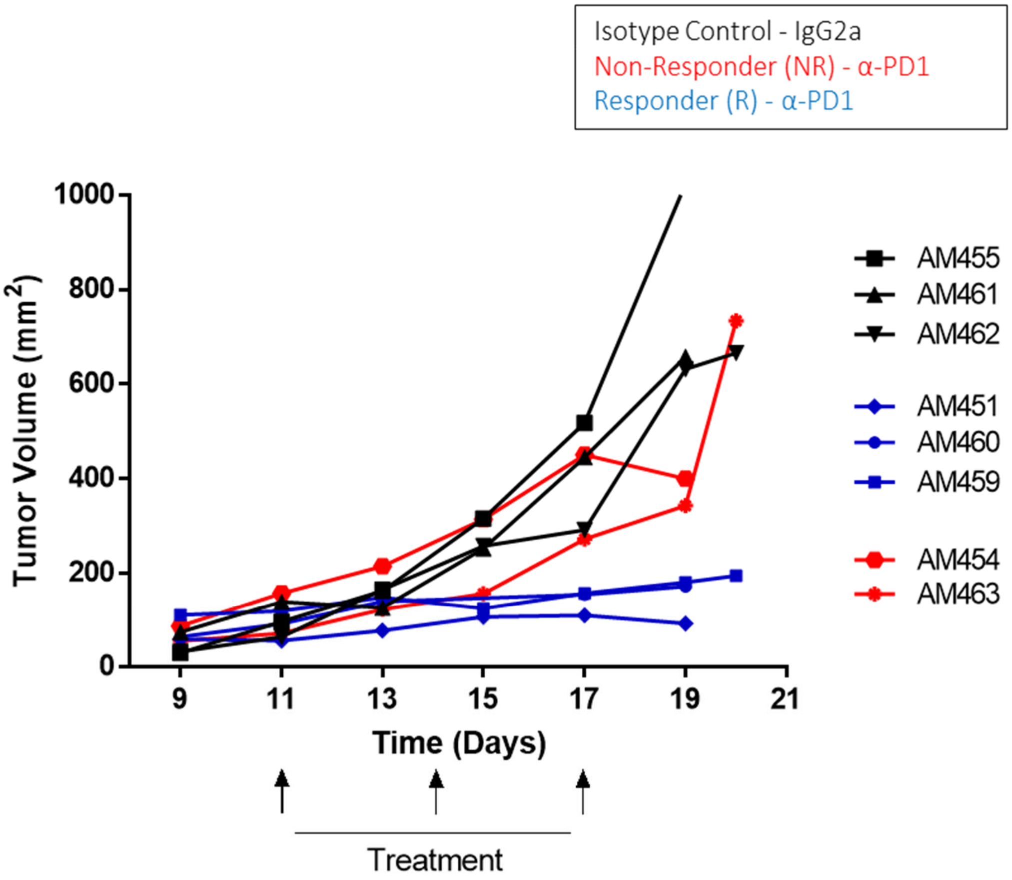

Figure 5.16 Growth kinetics of E0771 tumors with and without treatment. Untreated mice (black) show strong growth over the course of 3 weeks post treatment. Mice treated with three doses of αPD1 showed two phenotypes: responders that showed very little growth (blue) and non-responders which had similar growth kinetics to the untreated mice (red)

Because this model showed both responding and non-responding tumors in a genetically identical set of mice, it provided an excellent tool to begin to understand the differences that allow for varied responses to immunotherapy across patients. We began by performing biophysical analysis to compare the tumor cells of mice that had very strong responses (responders) to the untreated isotype control mice. A comparison of the cell diameter as measured by Coulter Counter shows minimal differences in the volumes of the tumor cells, with both untreated and responding tumor cells having a diameter of 12-16 µm (Figure 5.17a).

For subsequent biophysical measurements, we used the SMR tool described previously to measure buoyant mass. Additionally, a "node deviation" can be measured by observing the change in resonant frequency in the SMR at the node of vibration versus the background. This deviation from baseline can be used as a proxy for cell stiffness[162]. We found that in the untreated tumors, buoyant mass had two possible peaks in a bimodal distribution, either centered around 25pg or around 50pg. In these mice, the majority of cells existed as lighter cells near 25pg (Figure 5.17b). In terms of stiffness, these cells had very low node deviations, with a majority of cells having less than 4 Hz of node deviation (Figure 5.17c). However, drastically different phenotypes were observed in the tumors of responding mice. For those mice that had little tumor growth upon immunotherapy treatment, the buoyant mass of cells was significantly increased, though with a similar bimodal population as seen in the untreated tumors. Instead of the 25pg peak having the most cells, a vast majority of the cells in the responding tumors were 50-75pg in buoyant mass (Figure 5.17d). A similar observation was seen in the node deviation measurements, with cells from the responding mice having much higher node deviation.

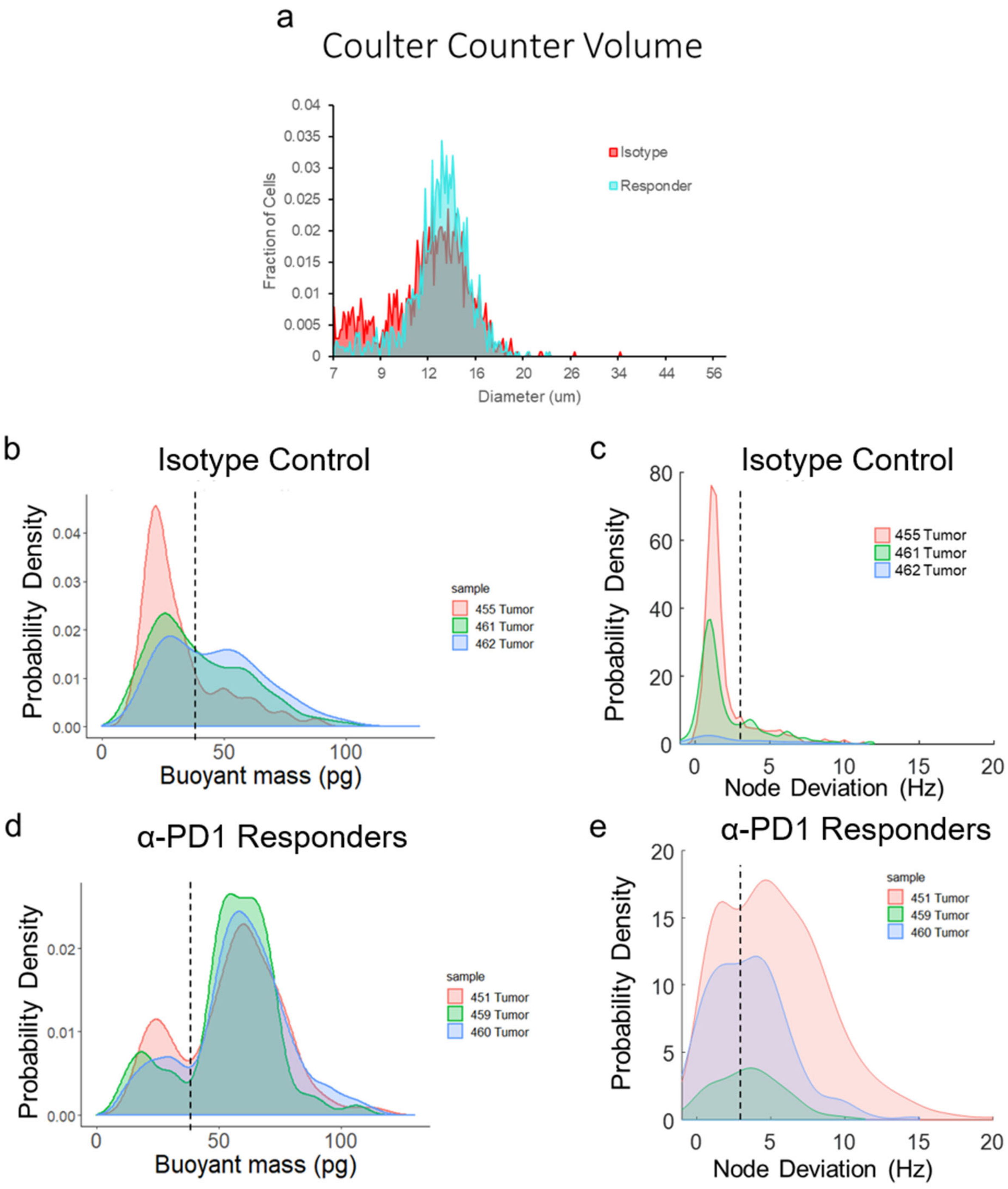

Figure 5.17 Biophysical measurements of E0771 tumor cells in untreated and responding mice. (a) Coulter Counter measurements show no change in volume of between the untreated and responding tumors. (b) Buoyant mass of tumor cells in untreated tumors shows a large fraction of cells with mass below 40 pg. (c) Node deviation, a measure of stiffness, shows relatively low stiffness for the untreated tumors. (d) Buoyant mass of tumor cells in responding tumors show marked increase in mass, with a majority of cells over 50 pg. (e) Node deviation show increased stiffness in tumor cells from tumors that respond strongly to αPD1 treatment.

This dramatic change in biophysical properties could allow for better understanding of whether a tumor is or is not responding well to immunotherapy treatment, or even predict whether a patient will respond to the therapy. Further studies will be required to repeat these results to determine the cohort-to-cohort heterogeneity, as well as understand the differences in physical properties of responding tumors to non-responding (but treated) tumors.

We continued our studies of heterogeneous response to immunotherapy by performing RNA sequencing. Using the Smart Seq 2 protocol, we performed single cell analysis on the transcriptomes of cells from three conditions: non-responders who received treatment but whose tumors continued to grow, responders who received treatment and showed minimal tumor outgrowth, and relapse mice who initially showed response to immunotherapy by later had tumor outgrowth. We used t-distributed Stochastic Neighbor Embedding (tSNE) for dimensionality reduction to observe clustering of cells based on their gene expression (Figure 5.18a). Three main clusters were observed, though no clear correlation was seen between cluster and tumor status (responding, non-responding, or relapse) (Figure 5.18b).

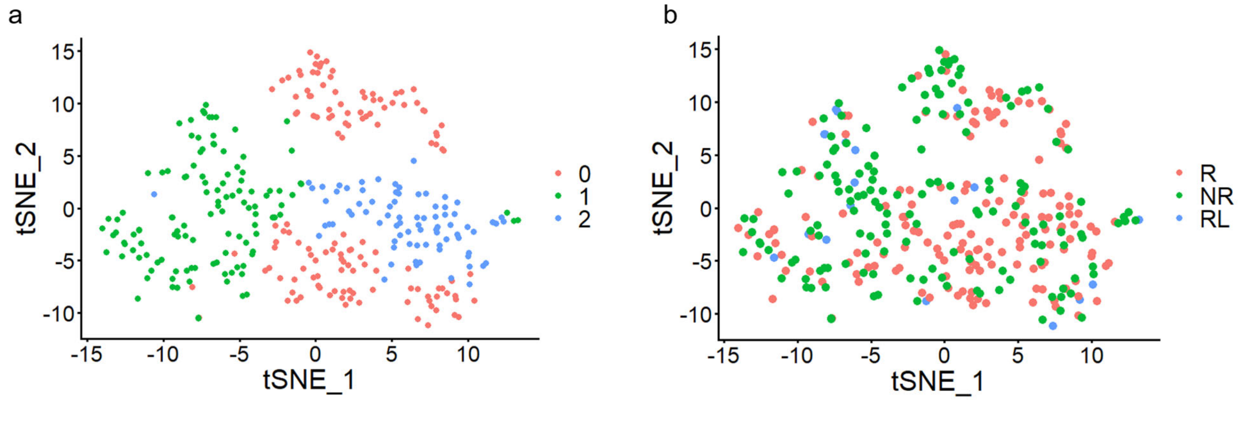

Figure 5.18 Single cell RNA-seq on immunotherapy treated E0771 tumor mice of varied response. (a) t-distributed Stochastic Neighbor Embedding (tSNE) plot showing clustering of transcriptomes of all sequenced cells. Three main clusters were identified. (b) tSNE plot colored by group shows no clear separation between cells from different groups, though non-responders seem to be most present in cluster 0, and responders in clusters 1 and 2. R – responding tumors, NR – nonresponding tumors, RL – relapse tumors.

We finally analyzed the top genes that define each cluster in the tSNE analysis. We found that cluster 0 had a high number of genes associated with metal homeostasis and response to hypoxia, while cluster 1 showed a number of genes associated with response to interferon and cytokines. Cluster 2 showed high levels of cell cycle genes. Further analysis will be needed to understand whether these functional traits influence the response of tumors to immunotherapy, and whether changes in these pathways can encourage more tumors to respond more dramatically to the immunotherapy treatment.

In summary, a key issue with current immunotherapies is the high degree of heterogeneity in response, with some patients experiencing prolonged cures and others having little to no benefit.

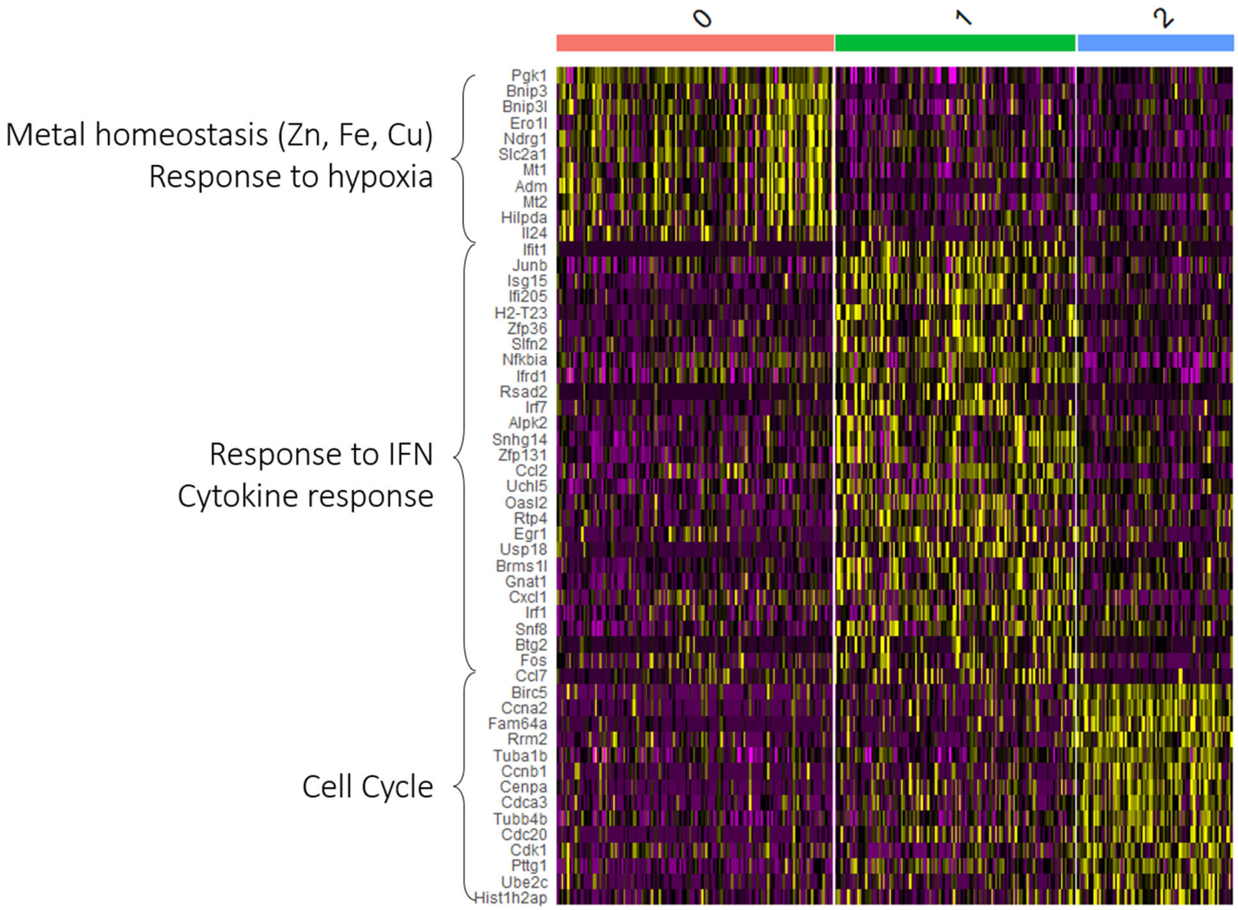

Figure 5.19 Top genes that define the tSNE clusters and functional pathways associated with the upregulated genes.

By studying the physical and transcriptional changes that determine whether a tumor will respond to immunotherapy or not, we hope to develop a signature that could either describe if a tumor is responding to therapy, or better yet, predict whether a patient will respond to a particular therapy.

5.4 Conclusions

Tumor cells and the blood are integrally connected. CTCs traveling in circulation provide the primary avenue for metastasis, the leading cause of death in cancer. And CLCs in leukemia not only provide metastatic potential, but also serve as a major compartment of disease. Studying the factors that define circulatory kinetics of CTCs and CLCs is instrumental in understanding how these cells traffic through the blood, which is crucial to developing new therapies. Our blood exchange technology is uniquely capable of addressing these questions through our ability to decouple circulating and extravascular contributions.

In this project, we began by developing a blood exchange tool to infuse native circulating tumor cells from a donor animal into a recipient. We then applied the technology to solid tumor models of small cell lung cancer, non-small cell lung cancer, and pancreatic cancer and showed the ability to estimate both generation rate and half-life time of the CTCs in circulation. We found that while generation rates in these models varied by several orders of magnitude, the half-life time varied only by approximately 2- to 3-fold. We also showed that the system can be used to generate metastatic models of disease through the infusion of as few as several thousand CTCs. Next, we used two leukemia models: acute lymphocytic leukemia (ALL) and acute myeloid leukemia (AML). With the leukemia models, which had significantly higher cells of CLCs in circulation compared to solid tumor CTCs, we were able to perform studies to assess the influence of non-circulatory and circulatory factors on the clearance rate of CLCs. In the ALL model, we showed that a diseased recipient animal has a drastically reduced fraction of cells cleared, a phenotype which was reversed after chemotherapy treatment. We found that while irradiation or chemotherapy alone were insufficient to significantly reduce the fraction cleared in healthy mice, the inhibition of E-selectin, an endothelial adhesion protein, reduced the fraction of CLCs remaining in circulation of diseased recipients. We suspect that inhibiting E-selectin, which is known to release cells from the bone marrow, allows for cells to more freely mix between the blood and marrow, which subsequently allows for more of the infused cells to exit circulation. Finally, we showed that in the AML model, but not the ALL model, relapse cells clear at a faster rate than untreated. We demonstrated that the relapse AML cells have significantly higher levels of adhesion molecules compared to untreated, and that AML has significantly higher expression of these adhesion molecules compared to the ALL model. Finally, we showed that blocking of the E-selectin binding molecules on the relapsed AML cells decreases the rate at which relapse AML cells escape circulation.

The blood exchange system provides a novel method to measure circulation kinetics of fluorescent cells in the blood. This platform can be used to continue exploring factors that influence the clearance of circulating tumor cells, but could also be used to study the clearance rates of other cells in the blood, such as immune-engineered CAR-T cells. The process of exchanging blood in animals to decouple circulating and non-circulating factors can also be applied even without using the fluorescence detection and circulation kinetics features. We are currently exploring the impact of the gut microbiome on tumor growth using the blood exchange system. By connecting circulation of tumor bearing mice to healthy mice with defined gut microbes, we hope to understand how specific intestinal bacteria can influence tumor outgrowth at distal sites, whether by local activation of immune cells or secretion of small molecules in the blood that impair tumor growth.

The data shown here demonstrates the essential role that adhesion molecules play in regulating clearance rates in leukemia. Several studies have begun to examine how interfering with cellular adhesion can induce drug efficacy, and our results suggest that there is much promise in this area. The development of novel drugs targeting an array of vascular adhesion molecules could improve patient outcomes in leukemia. Future directions for this project could explore the role that adhesion molecules play in circulation kinetics of additional models of leukemia, or of solid tumor CTCs, where interfering with the clearance of CTCs could reduce rates of metastasis.

This research also shows the sustained changes that tumor cells can undergo following treatment. Understanding that relapse and untreated disease have key biological differences requires the adaptation of therapeutics based on treatment status. Future studies will further examine the physical changes that cells undergo in response to chemotherapy and the underlying mechanisms driving those changes. Ultimately, these findings provide further insight into the features that control how tumor cells traffic through the body. By understanding these features, and learning how to influence them, new therapeutics can be developed to increase patient survival.

References

1. Lambert AW, Pattabiraman DR, Weinberg RA. Emerging Biological Principles of Metastasis. *Cell*. 2017;168(4):670-691. doi:10.1016/J.CELL.2016.11.037

2. Leong SP, Naxerova K, Keller L, Pantel K, Witte M. Molecular mechanisms of cancer metastasis via the lymphatic versus the blood vessels. *Clin Exp Metastasis*. 2022;39(1):159-179. doi:10.1007/S10585-021-10120-Z

3. Siegel RL, Miller KD, Wagle NS, Jemal A. Cancer statistics, 2023. *CA Cancer J Clin*. 2023;73(1):17-48. doi:10.3322/CAAC.21763

4. Whiteley AE, Price TT, Cantelli G, Sipkins DA. Leukaemia: a model metastatic disease. *Nat Rev Cancer*. 2021;21(7):461. doi:10.1038/S41568-021-00355-Z

5. Wicha MS, Hayes DF. Circulating tumor cells: Not all detected cells are bad and not all bad cells are detected. *Journal of Clinical Oncology*. 2011;29(12):1508-1511. doi:10.1200/JCO.2010.34.0026

6. Hong B, Zu Y. Detecting circulating tumor cells: Current challenges and new trends. *Theranostics*. 2013;3(6):377-394. doi:10.7150/THNO.5195

7. Kumar V, Abbas AK, Aster JC, Perkins JA. *Robbins Basic Pathology*.

8. Thiery JP, Acloque H, Huang RYJ, Nieto MA. Epithelial-mesenchymal transitions in development and disease. *Cell*. 2009;139(5):871-890. doi:10.1016/j.cell.2009.11.007

9. Yang J, Weinberg RA. Epithelial-mesenchymal transition: at the crossroads of development and tumor metastasis. *Dev Cell*. 2008;14(6):818-829. doi:10.1016/j.devcel.2008.05.009

10. Ting DT, Wittner BS, Maheswaran SM, Correspondence DAH. Single-Cell RNA Sequencing Identifies Extracellular Matrix Gene Expression by Pancreatic Circulating Tumor Cells Accession Numbers GSE51372 GSE60407 GSE51827 Ting et al. *CellReports*. 2014;8:1905-1918. doi:10.1016/j.celrep.2014.08.029

11. Gkountela S, Aceto N. Stem-like features of cancer cells on their way to metastasis. *Biol Direct*. 2016;11:33. doi:10.1186/s13062-016-0135-4

12. Schölch S, García SA, Iwata N, et al. Circulating tumor cells exhibit stem cell characteristics in an orthotopic mouse model of colorectal cancer. *Oncotarget*. 2016;7(19):27232-27242. doi:10.18632/oncotarget.8373

13. Massagué J, Obenauf AC. Metastatic colonization by circulating tumour cells. *Nature*. 2016;529(7586):298-309. doi:10.1038/nature17038

14. Morgan-Parkes JH. Metastases: Mechanisms, Pathways, and Cascades. *Advances in Clinical Medicine*. 1995;164:1075-1082. Accessed March 8, 2019. www.ajronline.org

15. Vanharanta S, Massagué J. Origins of metastatic traits. *Cancer Cell*. 2013;24(4):410-421. doi:10.1016/j.ccr.2013.09.007

16. Xie HY, Shao ZM, Li DQ. Tumor microenvironment: driving forces and potential therapeutic targets for breast cancer metastasis. *Chin J Cancer*. 2017;36(1):36. doi:10.1186/s40880-017-0202-y

17. Scully OJ, Bay BH, Yip G, Yu Y. Breast cancer metastasis. *Cancer Genomics Proteomics*. 2012;9(5):311-320. Accessed March 8, 2019. http://www.ncbi.nlm.nih.gov/pubmed/22990110

18. Coleman RE, Rubens RD. The clinical course of bone metastases from breast cancer. *Br J Cancer*. 1987;55(1):61-66. Accessed March 8, 2019. http://www.ncbi.nlm.nih.gov/pubmed/3814476

19. Arnold RS, Fedewa SA, Goodman M, et al. Bone metastasis in prostate cancer: Recurring mitochondrial DNA mutation reveals selective pressure exerted by the bone microenvironment. *Bone*. 2015;78:81-86. doi:10.1016/j.bone.2015.04.046

20. Mehra R, Kumar-Sinha C, Shankar S, et al. Characterization of bone metastases from rapid autopsies of prostate cancer patients. *Clin Cancer Res*. 2011;17(12):3924-3932. doi:10.1158/1078-0432.CCR-10-3120

21. Kircher DA, Silvis MR, Cho JH, Holmen SL. Melanoma Brain Metastasis: Mechanisms, Models, and Medicine. *Int J Mol Sci*. 2016;17(9). doi:10.3390/ijms17091468

22. Ma MW, Qian M, Lackaye DJ, et al. Challenging the current paradigm of melanoma progression: brain metastasis as isolated first visceral site. *Neuro Oncol*. 2012;14(7):849-858. doi:10.1093/neuonc/nos113

23. Langley RR, Fidler IJ. The seed and soil hypothesis revisited--the role of tumor-stroma interactions in metastasis to different organs. *Int J Cancer*. 2011;128(11):2527-2535. doi:10.1002/ijc.26031

24. de Groot AE, Roy S, Brown JS, Pienta KJ, Amend SR. Revisiting Seed and Soil: Examining the Primary Tumor and Cancer Cell Foraging in Metastasis. *Mol Cancer Res*. 2017;15(4):361-370. doi:10.1158/1541-7786.MCR-16-0436

25. Liu Q, Zhang H, Jiang X, Qian C, Liu Z, Luo D. Factors involved in cancer metastasis: a better understanding to "seed and soil" hypothesis. *Mol Cancer*. 2017;16(1):176. doi:10.1186/s12943-017-0742-4

26. Yue F, Cheng Y, Breschi A, et al. A comparative encyclopedia of DNA elements in the mouse genome. *Nature*. 2014;515(7527):355-364. doi:10.1038/NATURE13992

27. Lin S, Lin Y, Nery JR, et al. Comparison of the transcriptional landscapes between human and mouse tissues. *Proc Natl Acad Sci U S A*. 2014;111(48):17224-17229. doi:10.1073/PNAS.1413624111

28. Dolenšek J, Rupnik MS, Stožer A. Structural similarities and differences between the human and the mouse pancreas. *Islets*. 2015;7(1). doi:10.1080/19382014.2015.1024405

29. Anzai T, Yamagata T, Uosaki H. Comparative Transcriptome Landscape of Mouse and Human Hearts. *Front Cell Dev Biol*. 2020;8. doi:10.3389/FCELL.2020.00268/FULL

30. Cardoso-Moreira M, Halbert J, Valloton D, et al. Gene expression across mammalian organ development. *Nature*. 2019;571(7766):505-509. doi:10.1038/S41586-019-1338-5

31. Song Y, Wang Y, Guan A, et al. Footprints: Stamping hallmarks of lung cancer with patient-derived models, from molecular mechanisms to clinical translation. *Front Bioeng Biotechnol*. 2023;11. doi:10.3389/FBIOE.2023.1132940

32. Murayama T, Gotoh N. Patient-Derived Xenograft Models of Breast Cancer and Their Application. *Cells*. 2019;8(6). doi:10.3390/CELLS8060621

33. Yada E, Wada S, Yoshida S, Sasada T. Use of patient-derived xenograft mouse models in cancer research and treatment. *Future Sci OA*. 2018;4(3):FSO271. doi:10.4155/fsoa-2017-0136

34. Torphy RJ, Tignanelli CJ, Kamande JW, et al. Circulating Tumor Cells as a Biomarker of Response to Treatment in Patient-Derived Xenograft Mouse Models of Pancreatic Adenocarcinoma. Kyprianou N, ed. *PLoS One*. 2014;9(2):e89474. doi:10.1371/journal.pone.0089474

35. Ito R, Takahashi T, Katano I, Ito M. Current advances in humanized mouse models. *Cell Mol Immunol*. 2012;9(3):208. doi:10.1038/CMI.2012.2

36. Jung J, Seol HS, Chang S. The Generation and Application of Patient-Derived Xenograft Model for Cancer Research. *Cancer research and treatment : official journal of Korean Cancer Association*. 2018;50(1):1-10. doi:10.4143/crt.2017.307

37. Kersten K, Visser KE de, Miltenburg MH van, Jonkers J. Genetically engineered mouse models in oncology research and cancer medicine. *EMBO Mol Med*. 2017;9(2):137. doi:10.15252/EMMM.201606857

38. Sauer B, Henderson N. Site-specific DNA recombination in mammalian cells by the Cre recombinase of bacteriophage P1. *Proc Natl Acad Sci U S A*. 1988;85(14):5166-5170. doi:10.1073/PNAS.85.14.5166

39. Jones S, Zhang X, Parsons DW, et al. Core signaling pathways in human pancreatic cancers revealed by global genomic analyses. *Science (1979)*. 2008;321(5897):1801-1806. doi:10.1126/SCIENCE.1164368/SUPPL_FILE/JONES.SOM.REV1.PDF

40. Lee JW, Komar CA, Bengsch F, Graham K, Beatty GL. Genetically engineered mouse models of pancreatic cancer: The KPC model (LSL-KrasG12D/+;LSL-Trp53R172H/+;Pdx-1-Cre), its variants, and their application in immuno-oncology drug discovery. *Curr Protoc Pharmacol*. 2016;2016:14.39.1-14.39.20. doi:10.1002/cpph.2

41. Johnson L, Mercer K, Greenbaum D, et al. Somatic activation of the K-ras oncogene causes early onset lung cancer in mice. *Nature 2001 410:6832*. 2001;410(6832):1111-1116. doi:10.1038/35074129

42. Drosten M, Guerra C, Barbacid M. Genetically Engineered Mouse Models of K-Ras-Driven Lung and Pancreatic Tumors: Validation of Therapeutic Targets. *Cold Spring Harb Perspect Med*. 2018;8(5). doi:10.1101/CSHPERSPECT.A031542

43. Hingorani SR, Wang L, Multani AS, et al. Trp53R172H and KrasG12D cooperate to promote chromosomal instability and widely metastatic pancreatic ductal adenocarcinoma in mice. *Cancer Cell*. 2005;7(5):469-483. doi:10.1016/j.ccr.2005.04.023

44. DuPage M, Dooley AL, Jacks T. Conditional mouse lung cancer models using adenoviral or lentiviral delivery of Cre recombinase. *Nat Protoc*. 2009;4(7):1064-1072. doi:10.1038/nprot.2009.95

45. Chiou SH, Winters IP, Wang J, et al. Pancreatic cancer modeling using retrograde viral vector delivery and in vivo CRISPR/Cas9-mediated somatic genome editing. *Genes Dev*. 2015;29(14):1576-1585. doi:10.1101/GAD.264861.115

46. Heyer J, Kwong LN, Lowe SW, Chin L. Non-germline genetically engineered mouse models for translational cancer research. *Nat Rev Cancer*. 2010;10(7):470-480. doi:10.1038/NRC2877

47. Quinn BA, Xiao F, Bickel L, et al. Development of a syngeneic mouse model of epithelial ovarian cancer. *J Ovarian Res*. 2010;3(1):24. doi:10.1186/1757-2215-3-24

48. Mallya K, Gautam SK, Aithal A, Batra SK, Jain M. Modeling pancreatic cancer in mice for experimental therapeutics. *Biochimica et Biophysica Acta (BBA) - Reviews on Cancer*. 2021;1876(1):188554. doi:10.1016/J.BBCAN.2021.188554

49. Semba T, Sato R, Kasuga A, et al. Lung Adenocarcinoma Mouse Models Based on Orthotopic Transplantation of Syngeneic Tumor-Initiating Cells Expressing EpCAM, SCA-1, and Ly6d. *Cancers 2020, Vol 12, Page 3805*. 2020;12(12):3805. doi:10.3390/CANCERS12123805

50. Freed-Pastor WA, Lambert LJ, Ely ZA, et al. The CD155/TIGIT axis promotes and maintains immune evasion in neoantigen-expressing pancreatic cancer. *Cancer Cell*. 2021;39(10):1342-1360.e14. doi:10.1016/J.CCELL.2021.07.007/ATTACHMENT/966D924A-664F-41A1-8F8F-8BD0FCCC18FC/MMC6.XLSX

51. Céspedes MV, Casanova I, Parreño M, Mangues R. Mouse models in oncogenesis and cancer therapy. *Clinical and Translational Oncology*. 2006;8(5):318-329. doi:10.1007/S12094-006-0177-7

52. McFadden DG, Papagiannakopoulos T, Taylor-Weiner A, et al. Genetic and clonal dissection of murine small cell lung carcinoma progression by genome sequencing. *Cell*. 2014;156(6):1298-1311. doi:10.1016/J.CELL.2014.02.031

53. Platt RJ, Chen S, Zhou Y, et al. CRISPR-Cas9 knockin mice for genome editing and cancer modeling. *Cell*. 2014;159(2):440-455. doi:10.1016/J.CELL.2014.09.014

54. Kirkpatrick JD, Warren AD, Soleimany AP, et al. Urinary detection of lung cancer in mice via noninvasive pulmonary protease profiling. *Sci Transl Med*. 2020;12(537). doi:10.1126/SCITRANSLMED.AAW0262/SUPPL_FILE/AAW0262_SM.PDF

55. Dong Y, Shi O, Zeng Q, et al. Leukemia incidence trends at the global, regional, and national level between 1990 and 2017. *Exp Hematol Oncol*. 2020;9(1):1-11. doi:10.1186/S40164-020-00170-6/FIGURES/5

56. Pluta RM, Lynm C, Golub RM. Lymphocytic Leukemia. *JAMA*. 2011;305(1):112-112. doi:10.1001/JAMA.305.1.112

57. Hossfeld DK. Leukemia. *Manual of Clinical Oncology*. Published online 1994:495-514. doi:10.1007/978-3-642-85159-9_34

58. Mathews E, Laurie T, O'Riordan K, Nabhan C. Liver Involvement with Acute Myeloid Leukemia. *Case Rep Gastroenterol*. 2008;2(1):121. doi:10.1159/000120756

59. Doolittle ND. Brain metastases in hematologic malignancies. *Cancer Treat Res*. 2007;136:169-183. doi:10.1007/978-0-387-69222-7_9/COVER

60. Kumar B, Orellana M, Brooks J, et al. Exosome-driven lipolysis and bone marrow niche remodeling support leukemia expansion. *Haematologica*. 2021;106(5):1484. doi:10.3324/HAEMATOL.2019.246058

61. Chen Y, Hoffmeister LM, Zaun Y, et al. Acute myeloid leukemia-induced remodeling of the human bone marrow niche predicts clinical outcome. *Blood Adv*. 2020;4(20):5257-5268. doi:10.1182/BLOODADVANCES.2020001808

62. Kim JA, Shim JS, Lee GY, et al. Microenvironmental remodeling as a parameter and prognostic factor of heterogeneous leukemogenesis in acute myelogenous leukemia. *Cancer Res*. 2015;75(11):2222-2231. doi:10.1158/0008-5472.CAN-14-3379/651842/AM/MICROENVIRONMENTAL-REMODELING-AS-A-PARAMETER-AND

63. Duarte D, Hawkins ED, Akinduro O, et al. Inhibition of Endosteal Vascular Niche Remodeling Rescues Hematopoietic Stem Cell Loss in AML. *Cell Stem Cell*. 2018;22(1):64-77.e6. doi:10.1016/J.STEM.2017.11.006

64. Passaro D, Tullio A Di, Abarrategi A, et al. Increased Vascular Permeability in the Bone Marrow Microenvironment Contributes to Disease Progression and Drug Response in Acute Myeloid Leukemia. *Cancer Cell*. 2017;32(3):324. doi:10.1016/J.CCELL.2017.08.001

65. Rowe JM. The "7+3" regimen in acute myeloid leukemia. *Haematologica*. 2022;107(1):3. doi:10.3324/HAEMATOL.2021.280161

66. Di Francia R, Crisci S, De Monaco A, et al. Response and Toxicity to Cytarabine Therapy in Leukemia and Lymphoma: From Dose Puzzle to Pharmacogenomic Biomarkers. *Cancers (Basel)*. 2021;13(5):1-39. doi:10.3390/CANCERS13050966

67. Faruqi A, Tadi P. Cytarabine. *xPharm: The Comprehensive Pharmacology Reference*. Published online August 12, 2022:1-5. doi:10.1016/B978-008055232-3.61536-3

68. Samra B, Jabbour E, Ravandi F, Kantarjian H, Short NJ. Evolving therapy of adult acute lymphoblastic leukemia: state-of-the-art treatment and future directions. *J Hematol Oncol*. 2020;13(1). doi:10.1186/S13045-020-00905-2

69. Gbadamosi M, Meshinchi S, Lamba JK. Gemtuzumab ozogamicin for treatment of newly diagnosed CD33-positive acute myeloid leukemia. *Future Oncology*. 2018;14(30):3199. doi:10.2217/FON-2018-0325

70. Garitano-Trojaola A, Sancho A, Götz R, et al. Actin cytoskeleton deregulation confers midostaurin resistance in FLT3-mutant acute myeloid leukemia. *Commun Biol*. 2021;4(1):799. doi:10.1038/S42003-021-02215-W

71. Stone RM, Manley PW, Larson RA, Capdeville R. Midostaurin: its odyssey from discovery to approval for treating acute myeloid leukemia and advanced systemic mastocytosis. *Blood Adv*. 2018;2(4):444. doi:10.1182/BLOODADVANCES.2017011080

72. Naimi A, Mohammed RN, Raji A, et al. Tumor immunotherapies by immune checkpoint inhibitors (ICIs); the pros and cons. *Cell Commun Signal*. 2022;20(1):44. doi:10.1186/S12964-022-00854-Y

73. Zheng Y, Fang YC, Li J. PD-L1 expression levels on tumor cells affect their immunosuppressive activity. *Oncol Lett*. 2019;18(5):5399. doi:10.3892/OL.2019.10903

74. Chen L, Han X. Anti-PD-1/PD-L1 therapy of human cancer: past, present, and future. *J Clin Invest*. 2015;125(9):3384-3391. doi:10.1172/JCI80011

75. Bewersdorf JP, Stahl M, Zeidan AM. Immune checkpoint-based therapy in myeloid malignancies: a promise yet to be fulfilled. *Expert Rev Anticancer Ther*. 2019;19(5):393. doi:10.1080/14737140.2019.1589374

76. Chatterjee M, Turner DC, Felip E, et al. Systematic evaluation of pembrolizumab dosing in patients with advanced non-small-cell lung cancer. *Annals of Oncology*. 2016;27(7):1291. doi:10.1093/ANNONC/MDW174

77. Robert C, Ribas A, Wolchok JD, et al. Anti-programmed-death-receptor-1 treatment with pembrolizumab in ipilimumab-refractory advanced melanoma: a randomised dose-comparison cohort of a phase 1 trial. *Lancet*. 2014;384(9948):1109-1117. doi:10.1016/S0140-6736(14)60958-2

78. Shah BD, Ghobadi A, Oluwole OO, et al. KTE-X19 for relapsed or refractory adult B-cell acute lymphoblastic leukaemia: phase 2 results of the single-arm, open-label, multicentre ZUMA-3 study. *The Lancet*. 2021;398(10299):491-502. doi:10.1016/S0140-6736(21)01222-8

79. Melenhorst JJ, Chen GM, Wang M, et al. Decade-long leukaemia remissions with persistence of CD4+ CAR T cells. *Nature 2022 602:7897*. 2022;602(7897):503-509. doi:10.1038/s41586-021-04390-6

80. Jemal A, Ward EM, Johnson CJ, et al. Annual Report to the Nation on the Status of Cancer, 1975-2014, Featuring Survival. *J Natl Cancer Inst*. 2017;109(9). doi:10.1093/jnci/djx030

81. Hauwel M, Matthes T. Minimal residual disease monitoring: the new standard for treatment evaluation of haematological malignancies? *Swiss Medical Weekly 2014 :3*. 2014;144(3). doi:10.4414/SMW.2014.13907

82. Chiaretti S, Zini G, Bassan R. Diagnosis and Subclassification of Acute Lymphoblastic Leukemia. *Mediterr J Hematol Infect Dis*. 2014;6(1). doi:10.4084/MJHID.2014.073

83. Arber DA, Erba HP. Diagnosis and Treatment of Patients with Acute Myeloid Leukemia with Myelodysplasia-Related Changes (AML-MRC). *Am J Clin Pathol*. 2020;154(6):731-741. doi:10.1093/AJCP/AQAA107

84. Cheson BD, Bennett JM, Kopecky KJ, et al. Revised Recommendations of the International Working Group for diagnosis, standardization of response criteria, treatment outcomes, and reporting standards for therapeutic trials in acute myeloid leukemia. *Journal of Clinical Oncology*. 2003;21(24):4642-4649. doi:10.1200/JCO.2003.04.036

85. Schuurhuis GJ, Heuser M, Freeman S, et al. Minimal/measurable residual disease in AML: a consensus document from the European LeukemiaNet MRD Working Party. *Blood*. 2018;131(12):1275. doi:10.1182/BLOOD-2017-09-801498

86. Weng XQ, Shen Y, Sheng Y, et al. Prognostic significance of monitoring leukemia-associated immunophenotypes by eight-color flow cytometry in adult B-acute lymphoblastic leukemia. *Blood Cancer Journal 2013 3:8*. 2013;3(8):e133-e133. doi:10.1038/bcj.2013.31

87. Short NJ, Zhou S, Fu C, et al. Association of Measurable Residual Disease With Survival Outcomes in Patients With Acute Myeloid Leukemia: A Systematic Review and Meta-analysis. *JAMA Oncol*. 2020;6(12):1890-1899. doi:10.1001/JAMAONCOL.2020.4600

88. Terwijn M, Kelder A, Huijgens PC, et al. High prognostic impact of flow cytometric minimal residual disease detection in acute myeloid leukemia: data from the HOVON/SAKK AML 42A study. *J Clin Oncol*. 2013;31(31):3889-3897. doi:10.1200/JCO.2012.45.9628

89. Luskin MR, Murakami MA, Manalis SR, Weinstock DM. Targeting minimal residual disease: a path to cure? *Nat Rev Cancer*. 2018;18(4):255. doi:10.1038/NRC.2017.125

90. Ngai LL, Kelder A, Janssen JJWM, Ossenkoppele GJ, Cloos J. MRD Tailored Therapy in AML: What We Have Learned So Far. *Front Oncol*. 2021;10:2860. doi:10.3389/FONC.2020.603636/BIBTEX

91. Akinduro O, Weber TS, Ang H, et al. Proliferation dynamics of acute myeloid leukaemia and haematopoietic progenitors competing for bone marrow space. *Nature Communications 2018 9:1*. 2018;9(1):1-12. doi:10.1038/s41467-017-02376-5

92. Duy C, Li M, Teater M, et al. Chemotherapy induces senescence-like resilient cells capable of initiating AML recurrence. *Cancer Discov*. 2021;11(6):1542. doi:10.1158/2159-8290.CD-20-1375

93. Mercier FE, Shi J, Sykes DB, et al. In vivo genome-wide CRISPR screening in murine acute myeloid leukemia uncovers microenvironmental dependencies. *Blood Adv*. 2022;6(17):5072-5084. doi:10.1182/BLOODADVANCES.2022007250

94. Fiedler ERC, Bhutkar A, Lawler E, Besada R, Hemann MT. In vivo RNAi screening identifies Pafah1b3 as a target for combination therapy with TKIs in BCR-ABL1+ BCP-ALL. *Blood Adv*. 2018;2(11):1229-1242. doi:10.1182/BLOODADVANCES.2017015610

95. Almosailleakh M, Schwaller J. Murine Models of Acute Myeloid Leukaemia. *International Journal of Molecular Sciences 2019, Vol 20, Page 453*. 2019;20(2):453. doi:10.3390/IJMS20020453

96. Hassan N, Yang J, Wang JY. An Improved Protocol for Establishment of AML Patient-Derived Xenograft Models. *STAR Protoc*. 2020;1(3). doi:10.1016/J.XPRO.2020.100156

97. Largaespada DA. Genetic heterogeneity in acute myeloid leukemia: maximizing information flow from MuLV mutagenesis studies. *Leukemia*. 2000;14(7):1174-1184. doi:10.1038/SJ.LEU.2401852

98. Jacoby E, Chien CD, Fry TJ. Murine Models of Acute Leukemia: Important Tools in Current Pediatric Leukemia Research. *Front Oncol*. 2014;4. doi:10.3389/FONC.2014.00095

99. Castellanos A, Pintado B, Weruaga E, et al. A BCR-ABLp190 Fusion Gene Made by Homologous Recombination Causes B-Cell Acute Lymphoblastic Leukemias in Chimeric Mice With Independence of the Endogenous bcr Product. *Blood*. 1997;90(6):2168-2174. doi:10.1182/BLOOD.V90.6.2168

100. Barbier V, Erbani J, Fiveash C, et al. Endothelial E-selectin inhibition improves acute myeloid leukaemia therapy by disrupting vascular niche-mediated chemoresistance. *Nature Communications 2020 11:1*. 2020;11(1):1-15. doi:10.1038/s41467-020-15817-5

101. Konopleva M, Konoplev S, Hu W, Zaritskey AY, Afanasiev B V., Andreeff M. Stromal cells prevent apoptosis of AML cells by up-regulation of anti-apoptotic proteins. *Leukemia*. 2002;16(9):1713-1724. doi:10.1038/SJ.LEU.2402608

102. Zeng Z, Samudio IJ, Munsell M, et al. Inhibition of CXCR4 with the novel RCP168 peptide overcomes stroma-mediated chemoresistance in chronic and acute leukemias. *Mol Cancer Ther*. 2006;5(12):3113-3121. doi:10.1158/1535-7163.MCT-06-0228

103. Grenier JMP, Testut C, Fauriat C, Mancini SJC, Aurrand-Lions M. Adhesion Molecules Involved in Stem Cell Niche Retention During Normal Haematopoiesis and in Acute Myeloid Leukaemia. *Front Immunol*. 2021;12:4799. doi:10.3389/FIMMU.2021.756231/BIBTEX

104. DeAngelo DJ, Jonas BA, Liesveld JL, et al. Phase 1/2 study of uproleselan added to chemotherapy in patients with relapsed or refractory acute myeloid leukemia. *Blood*. 2022;139(8):1135-1146. doi:10.1182/BLOOD.2021010721

105. Berrazouane S, Boisvert M, Salti S, et al. Beta1 integrin blockade overcomes doxorubicin resistance in human T-cell acute lymphoblastic leukemia. *Cell Death & Disease 2019 10:5*. 2019;10(5):1-13. doi:10.1038/s41419-019-1593-2

106. Scharff BFSS, Modvig S, Marquart HV, Christensen C. Integrin-Mediated Adhesion and Chemoresistance of Acute Lymphoblastic Leukemia Cells Residing in the Bone Marrow or the Central Nervous System. *Front Oncol*. 2020;10:775. doi:10.3389/FONC.2020.00775

107. Allard WJ, Matera J, Miller MC, et al. Tumor Cells Circulate in the Peripheral Blood of All Major Carcinomas but not in Healthy Subjects or Patients With Nonmalignant Diseases. *Clinical Cancer Research*. 2004;10(20):6897-6904. doi:10.1158/1078-0432.CCR-04-0378

108. Cabel L, Proudhon C, Gortais H, et al. Circulating tumor cells: clinical validity and utility. *Int J Clin Oncol*. 2017;22(3):421-430. doi:10.1007/s10147-017-1105-2

109. Lara O, Tong X, Zborowski M, Chalmers JJ. Enrichment of rare cancer cells through depletion of normal cells using density and flow-through, immunomagnetic cell separation. *Exp Hematol*. 2004;32(10):891-904. doi:10.1016/j.exphem.2004.07.007

110. Che J, Yu V, Garon EB, Goldman JW, Di Carlo D. Biophysical isolation and identification of circulating tumor cells. *Lab Chip*. 2017;17(8):1452. doi:10.1039/C7LC00038C

111. Fan X, Jia C, Yang J, et al. A microfluidic chip integrated with a high-density PDMS-based microfiltration membrane for rapid isolation and detection of circulating tumor cells. *Biosens Bioelectron*. 2015;71:380-386. doi:10.1016/J.BIOS.2015.04.080

112. Martel JM, Toner M. Inertial Focusing in Microfluidics. *https://doi.org/101146/annurev-bioeng-121813-120704*. 2014;16:371-396. doi:10.1146/ANNUREV-BIOENG-121813-120704

113. Raimondi C, Nicolazzo C, Gradilone A, et al. Circulating tumor cells: exploring intratumor heterogeneity of colorectal cancer. *Cancer Biol Ther*. 2014;15(5):496-503. doi:10.4161/cbt.28020

114. Kirby BJ, Jodari M, Loftus MS, et al. Functional characterization of circulating tumor cells with a prostate-cancer-specific microfluidic device. *PLoS One*. 2012;7(4):e35976. doi:10.1371/journal.pone.0035976

115. Andreopoulou E, Yang LY, Rangel KM, et al. Comparison of assay methods for detection of circulating tumor cells in metastatic breast cancer: AdnaGen AdnaTest BreastCancer Select/Detect^{TM} versus Veridex CellSearch^{TM} system. *Int J Cancer*. 2012;130(7):1590-1597. doi:10.1002/ijc.26111

116. Nagrath S, Sequist L V, Maheswaran S, et al. Isolation of rare circulating tumour cells in cancer patients by microchip technology. *Nature*. 2007;450(7173):1235-1239. doi:10.1038/nature06385

117. Stott SL, Hsu CH, Tsukrov DI, et al. Isolation of circulating tumor cells using a microvortex-generating herringbone-chip. *Proc Natl Acad Sci U S A*. 2010;107(43):18392-18397. doi:10.1073/pnas.1012539107

118. Pei H, Li L, Wang Y, et al. Single-Cell Phenotypic Profiling of CTCs in Whole Blood Using an Integrated Microfluidic Device. *Anal Chem*. 2019;91(17):11078-11084. doi:10.1021/ACS.ANALCHEM.9B01647/SUPPL_FILE/AC9B01647_SI_006.MP4

119. Wang Z, Sun N, Liu H, et al. High-Efficiency Isolation and Rapid Identification of Heterogeneous Circulating Tumor Cells (CTCs) Using Dual-Antibody-Modified Fluorescent-Magnetic Nanoparticles. *ACS Appl Mater Interfaces*. 2019;11(43):39586-39593. doi:10.1021/ACSAMI.9B14051/SUPPL_FILE/AM9B14051_SI_001.PDF

120. Fidler IJ. Metastasis: Quantitative Analysis of Distribution and Fate of Tumor Emboli Labeled With 125I-5-Iodo-2′ -deoxyuridine. *JNCI: Journal of the National Cancer Institute*. 1970;45(4):773-782. doi:10.1093/JNCI/45.4.773

121. Juratli MA, Siegel ER, Nedosekin DA, et al. In vivo long-term monitoring of circulating tumor cells fluctuation during medical interventions. *PLoS One*. 2015;10(9). doi:10.1371/journal.pone.0137613

122. Williams A, Fitzgerald J, Niedre M. Short-term circulating tumor cell dynamics in mouse xenograft models and implications for liquid biopsy. *bioRxiv*. Published online October 22, 2019:814368. doi:10.1101/814368

123. Steenbergen W, Zharov VP. Towards Reaching the Total Blood Volume by in vivo Flow Cytometry and Theranostics. *Cytometry Part A*. 2019;95(12):1223-1225. doi:10.1002/CYTO.A.23916

124. Madden RE, Malmgren RA. Quantitative Studies on Circulating Cancer Cells in the Mouse | Cancer Research | American Association for Cancer Research. Cancer research. Published 1962. Accessed May 1, 2022. https://aacrjournals.org/cancerres/article/22/1_Part_1/62/474851/Quantitative-Studies-on-Circulating-Cancer-Cells

125. Aceto N, Toner M, Maheswaran S, Haber DA. En Route to Metastasis: Circulating Tumor Cell Clusters and Epithelial-to-Mesenchymal Transition. *Trends Cancer*. 2015;1(1):44-52. doi:10.1016/j.trecan.2015.07.006

126. Meng S, Tripathy D, Frenkel EP, et al. Circulating tumor cells in patients with breast cancer dormancy. *Clin Cancer Res*. 2004;10(24):8152-8162. doi:10.1158/1078-0432.CCR-04-1110

127. GALBRAITH PR, VALBERG LS, BROWN M. Patterns of Granulocyte Kinetics in Health, Infection and in Carcinoma. *Blood*. 1965;25(5):683-692. doi:10.1182/BLOOD.V25.5.683.683

128. CARTWRIGHT GE, ATHENS JW, WINTROBE MM. Analytical Review: The Kinetics of Granulopoiesis in Normal Man. *Blood*. 1964;24(6):780-803. doi:10.1182/BLOOD.V24.6.780.780

129. Spivak JL, Brubaker LH, Perry S. Intravascular Granulocyte Kinetics in Acute Leukemia. *Blood*. 1969;34(5):582-590. doi:10.1182/BLOOD.V34.5.582.582

130. Hamza B, Ng SR, Prakadan SM, et al. Optofluidic real-time cell sorter for longitudinal CTC studies in mouse models of cancer. *Proc Natl Acad Sci U S A*. 2019;116(6):2232-2236. doi:10.1073/pnas.1814102116

131. Hum NR, Sebastian A, Gilmore SF, et al. Comparative Molecular Analysis of Cancer Behavior Cultured In Vitro, In Vivo, and Ex Vivo. *Cancers (Basel)*. 2020;12(3). doi:10.3390/CANCERS12030690

132. Pampaloni F, Reynaud EG, Stelzer EHK. The third dimension bridges the gap between cell culture and live tissue. *Nat Rev Mol Cell Biol*. 2007;8(10):839-845. doi:10.1038/NRM2236

133. Butler TP, Gullino PM. Quantitation of Cell Shedding into Efferent Blood of Mammary Adenocarcinoma1 | Cancer Research | American Association for Cancer Research. *Cancer Res*. 1975;35(3):512-516. Accessed March 15, 2023.

https://aacrjournals.org/cancerres/article/35/3/512/480587/Quantitation-of-Cell-Shedding-into-Efferent-Blood

134. Mehdipour M, Amiri P, Liu C, et al. Small-animal blood exchange is an emerging approach for systemic aging research. doi:10.1038/s41596-022-00731-5

135. Conboy MJ, Conboy IM, Rando TA. Heterochronic parabiosis: historical perspective and methodological considerations for studies of aging and longevity. *Aging Cell*. 2013;12(3):525. doi:10.1111/ACEL.12065

136. Hamza B, Miller AB, Meier L, et al. Measuring kinetics and metastatic propensity of CTCs by blood exchange between mice. *Nature Communications 2021 12:1*. 2021;12(1):1-11. doi:10.1038/s41467-021-25917-5

137. Bossuyt X, Marti GE, Fleisher TA. Comparative analysis of whole blood lysis methods for flow cytometry. *Communications in Clinical Cytometry*. 1997;30(3). doi:10.1002/(SICI)1097-0320(19970615)30:3<124::AID-CYTO3>3.0.CO;2-L

138. Vašíček J, Baláži A, Bauer M, et al. Enrichment of rabbit primitive hematopoietic cells via macs depletion of CD45+ bone marrow cells. *Magnetochemistry*. 2021;7(1):1-15. doi:10.3390/MAGNETOCHEMISTRY7010011

139. Krebs MG, Hou JM, Ward TH, Blackhall FH, Dive C. Circulating tumour cells: their utility in cancer management and predicting outcomes. *Ther Adv Med Oncol*. 2010;2(6):351. doi:10.1177/1758834010378414

140. Del Monte U. Does the cell number 109 still really fit one gram of tumor tissue? *https://doi.org/104161/cc837608*. 2009;8(3):505-506. doi:10.4161/CC.8.3.7608

141. Zou D, Cui D. Advances in isolation and detection of circulating tumor cells based on microfluidics. *Cancer Biol Med*. 2018;15(4):335-353. doi:10.20892/j.issn.2095-3941.2018.0256

142. Burg TP, Godin M, Knudsen SM, et al. Weighing of biomolecules, single cells and single nanoparticles in fluid. *Nature 2007 446:7139*. 2007;446(7139):1066-1069. doi:10.1038/nature05741

143. Stevens MM, Maire CL, Chou N, et al. Drug sensitivity of single cancer cells is predicted by changes in mass accumulation rate. *Nature Biotechnology 2016 34:11*. 2016;34(11):1161-1167. doi:10.1038/nbt.3697

144. Olcum S, Cermak N, Wasserman SC, Manalis SR. High-speed multiple-mode mass-sensing resolves dynamic nanoscale mass distributions. *Nature Communications 2015 6:1*. 2015;6(1):1-8. doi:10.1038/ncomms8070

145. Bagnall JS, Byun S, Begum S, et al. Deformability of Tumor Cells versus Blood Cells. *Scientific Reports 2015 5:1*. 2015;5(1):1-11. doi:10.1038/srep18542

146. Sudhesh Dev S, Zainal Abidin SA, Farghadani R, Othman I, Naidu R. Receptor Tyrosine Kinases and Their Signaling Pathways as Therapeutic Targets of Curcumin in Cancer. *Front Pharmacol*. 2021;12:3266. doi:10.3389/FPHAR.2021.772510/BIBTEX

147. Fleischmann KK, Pagel P, Von Frowein J, Magg T, Roscher AA, Schmid I. The leukemogenic fusion gene MLL-AF9 alters microRNA expression pattern and inhibits monoblastic differentiation via MIR-511 repression. *Journal of Experimental and Clinical Cancer Research*. 2016;35(1):1-15. doi:10.1186/S13046-016-0283-5/FIGURES/7

148. Meyer C, Hofmann J, Burmeister T, et al. The MLL recombinome of acute leukemias in 2013. *Leukemia*. 2013;27(11). doi:10.1038/leu.2013.135

149. Shalapour S, Hof J, Kirschner-Schwabe R, et al. High VLA-4 expression is associated with adverse outcome and distinct gene expression changes in childhood B-cell precursor acute lymphoblastic leukemia at first relapse. *Haematologica*. 2011;96(11):1627-1635. doi:10.3324/HAEMATOL.2011.047993

150. Fay ME, Myers DR, Kumar A, et al. Cellular softening mediates leukocyte demargination and trafficking, thereby increasing clinical blood counts. *Proceedings of the National Academy of Sciences*. 2016;113(8):1987-1992. doi:10.1073/PNAS.1508920113

151. Pezeshkian B, Donnelly C, Tamburo K, Geddes T, Madlambayan GJ. Leukemia Mediated Endothelial Cell Activation Modulates Leukemia Cell Susceptibility to Chemotherapy through a Positive Feedback Loop Mechanism. *PLoS One*. 2013;8(4):e60823. doi:10.1371/JOURNAL.PONE.0060823

152. Stucki A, Rivier AS, Gikic M, Monai N, Schapira M, Spertini O. Endothelial cell activation by myeloblasts: molecular mechanisms of leukostasis and leukemic cell dissemination. *Blood*. 2001;97(7):2121-2129. doi:10.1182/BLOOD.V97.7.2121

153. Tuzuner N, Cox C, Rowe JM, Bennett JM. Bone marrow cellularity in myeloid stem cell disorders: impact of age correction. *Leuk Res*. 1994;18(8):559-564. doi:10.1016/0145-2126(94)90036-1

154. Zhang B, Nguyen LXT, Zhao D, et al. Treatment-induced arteriolar revascularization and miR-126 enhancement in bone marrow niche protect leukemic stem cells in AML. *J Hematol Oncol*. 2021;14(1). doi:10.1186/S13045-021-01133-Y

155. Mezu-Ndubuisi OJ, Maheshwari A. The role of integrins in inflammation and angiogenesis. *Pediatric Research 2020 89:7*. 2020;89(7):1619-1626. doi:10.1038/s41390-020-01177-9

156. Gkountela S, Castro-Giner F, Szczerba BM, et al. Circulating Tumor Cell Clustering Shapes DNA Methylation to Enable Metastasis Seeding. *Cell*. 2019;176(1-2):98-112.e14. doi:10.1016/j.cell.2018.11.046

157. Fabisiewicz A, Grzybowska E. CTC clusters in cancer progression and metastasis. *Medical Oncology*. 2017;34(1):12. doi:10.1007/s12032-016-0875-0

158. Aceto N, Bardia A, Miyamoto DT, et al. Circulating tumor cell clusters are oligoclonal precursors of breast cancer metastasis. *Cell*. 2014;158(5):1110-1122. doi:10.1016/j.cell.2014.07.013

159. Pliss A, Zhao L, Ohulchanskyy TY, Qu J, Prasad PN. Fluorescence lifetime of fluorescent proteins as an intracellular environment probe sensing the cell cycle progression. *ACS Chem Biol*. 2012;7(8):1385-1392. doi:10.1021/CB300065W/SUPPL_FILE/CB300065W_SI_001.PDF

160. Zhou J, Papautsky I. Viscoelastic microfluidics: progress and challenges. *Microsyst Nanoeng*. 2020;6(1). doi:10.1038/S41378-020-00218-X

161. Le Naour A, Rossary A, Vasson MP. EO771, is it a well-characterized cell line for mouse mammary cancer model? Limit and uncertainty. *Cancer Med*. 2020;9(21):8074-8085. doi:10.1002/CAM4.3295

162. Kang JH, Miettinen TP, Chen L, et al. Non-invasive monitoring of single-cell mechanics by acoustic scattering. *Nat Methods*. 2019;16(3):263. doi:10.1038/S41592-019-0326-X